Master's thesis

Siren Ånestad

The Magnetic Petrological Expression of Slipsteinsberget, a Zoned Serpentinized Ultramafic Body in Trøndelag

Master's thesis in Geology
Supervisor: Christine Fichler & Mai Britt E. Mørk
May 2020

NTNU
Norwegian University of
Science and Technology

Siren Ånestad

The Magnetic Petrological Expression of Slipsteinsberget, a Zoned Serpentinized Ultramafic Body in Trøndelag

Master's thesis in Geology
Supervisor: Christine Fichler & Mai Britt E. Mørk
May 2020

Norwegian University of Science and Technology
Faculty of Engineering
Department of Geoscience and Petroleum

NTNU
Norwegian University of
Science and Technology

Abstract

Slipsteinsberget is a zoned serpentinized ultramafic body located near Sparbu, Trøndelag county, Norway. Slipsteinsberget is situated within the Neoproterozoic to Late Cambrian Skjøtningen Nappe. It has a long archeological history dating back to the early 11th century, where soapstone vessels were produced on a large scale. In more recent time, Slipsteinsberget has been exploited for serpentinite "dimension stones", and the resulting quarry has created excellent outcrops to investigate the ultramafic rocks.

As isolated ultramafic metamorphosed bodies of minor size are still a matter of research regarding genesis, composition, and geometry, a wide variety of methods have been used in this thesis to investigate Slipsteinsberget. The fieldwork included geological mapping, sampling of oriented blocks, and magnetic susceptibility measurements. The field samples were cut into thin sections and cylinders for optical microscopy, scanning electron microscopy, and geophysical testing. A comprehensive magnetic petrological investigation was conducted to identify and quantify the magnetic minerals as wells as to understand how they formed and how they affected the bulk magnetism of Slipsteinsberget. Also, a ground magnetic survey over the area was conducted with the aim to model the subsurface by 3D magnetic modeling. The ground magnetic survey revealed a magnetic core in the center of the quarry consisting of serpentinites with total magnetic intensities (TMI) between 55,900 and 54,700nT.

The serpentinites have been divided into three distinct subgroups based on their mineralogy and magnetic expression. In a decreasing order of magnetization, these are: (1) A dark green serpentinite containing olivine, micromagnetite, and zoned Cr-spinels, (2) a brecciated serpentinite containing micromagnetites and zoned Cr-spinels, and (3) a green serpentinite dominated by antigorite without any observed magnetic minerals. The serpentinites of Slipsteinsberget are zoned with the dark green serpentinite confined to the core, surrounded by the brecciated serpentinite, which is again enclosed by the green serpentinite. 3D magnetic modeling of the serpentinites revealed an elliptical-shaped zoned body which is estimated to have a maximum thickness of 40m on the western side of Slipsteinsberget and a total volume of ~300 000m^3. The model follows the general foliation of the surrounding garnet mica-schist with a dip direction towards the southwest.

The investigation of Slipsteinsberget made it possible to correlate its magnetic anomaly to other less studied ultramafic rocks at Sparbu by comparing the upward continued ground magnetic survey of Slipstinsberget to aeromagnetic data over Sparbu, provided by NGU. The results from this thesis indicate that the ultramafic bodies at Sparbu may be larger than published on geological maps (NGU) and that other subsurface bodies might exist in this area. On a larger scale, comparing Slipsteinsberget to other well studied ultramafic rocks along the Trøndelag-Jämtland border, there might be a connection to an extending belt of ultramafic bodies from Røros to Snåsa.

Combining observations from this thesis with former work, it is reasonable to argue that the serpentinites of Slipsteinsberget may have formed during the opening of the Iapetus Ocean in an oceanic to continent transitional setting. Prior to and during the creation of the Scandian Orogeny, the serpentinized ultramafic rocks were thrusted onto the Baltican plate and may later have protruded along steep faults due to density contrast to the enclosing rocks. The metamorphic grade likely reached greenschist facies. Finally, the addition of CO_2-rich hydrothermal fluids may have metasomatized the serpentinites into the observed zoned ultramafic body today.

Sammendrag

Slipsteinsberget er et brudd i en sonert serpentinisert ultramafisk kropp nær Sparbu, Trøndelag, Norge. Bruddet befinner seg i det neoproterosoiske til kambriske Skjøtningsdekket. Arkeologisk sett har området en lang historie som kan følges helt tilbake til tidlig 1000 tallet, da ble klebersteinsgryter produsert i stor skala. I nyere tid har Slipsteinsberget blitt brukt til produksjon av naturstein, og det tilhørende bruddet har dermed gode blotninger for å utforske den ultramafiske kroppen.

Det forskes stadig på metamorfe ultramafiske bergarter med tanke på dems opprinnelse og geologiske utvikling. Det har derfor blitt brukt et bredt spekter av metoder i denne oppgaven for å utforske Slipsteinsberget. Feltarbeidet inkluderer geologisk kartlegging, prøvetaking av orienterte blokker, og magnetiske susceptibilitetmålinger. Prøvene fra felt ble videre bearbeidet til tynnslip og sylindere for optisk mikroskopering, elektronmikroskop og geofysisk testing. En omfattende magnetisk petrologisk undersøkelse ble igangsatt for å identifisere og kvantifisere de magnetiske mineralene i bergartene, samt for å forstå hvordan de ble dannet og hvordan de påvirker magnetismen til Slipsteinsberget. En magnetisk bakkeundersøkelse ble også gjennomført over området for å kunne modellere undergrunnen ved en 3D-magnetisk modellering. Under undersøkelsen ble det funnet en magnetisk kjerne i sentrum av bruddet bestående av serpentinitt med en total magnetisk intensitet (TMI) mellom 55 900 og 54 000nT.

Serpentinittene har blitt delt inn i tre distinkte grupper basert på deres mineralinnhold og magnetiske utrykk. I minkende grad av magnetisering er disse: (1) en mørkegrønn serpentinitt med innhold av olivin, mikromagnetitt og sonerte Cr-spineller, (2) en breksjert serpentinitt med mikromagnetitt og sonerte Cr-spineller og (3) en grønn serpentinitt dominert av antigoritt uten magnetiske mineral. Den mørkegrønne serpentinitten befinner seg i kjernen, omsluttet av den breksjerte serpentinitten som igjen er omsluttet av den grønne serpentinitten. 3D-magnetisk modellering av serpentinittene viste en elliptisk sonert kropp med en estimert maksimal tykkelse på 40m på den vestlige siden av Slipsteinsberget og et volum på ~300 000m³. Modellen følger den generelle foliasjonen til den omkringliggende granatglimmerskiferen med en fallretning mot sørvest.

Undersøkelsen av Slipsteinsberget gjorde det mulig å korrelere dens magnetiske anomali til andre, mindre studerte, ultramafiske bergarter på Sparbu. Dette ble gjort ved å sammenligne den ekstrapolerte magnetiske bakkeundersøkelsen av Slipsteinsberget til aeromagnetisk data over Sparbu, gitt av NGU. Resultatene fra denne oppgaven indikerer at de ultramafiske bergartene på Sparbu muligens er større enn antatt på bergrunnskart (NGU) og at det kan finnes flere kropper skjult i grunnen. Visse likheter mellom Slipsteinsberget og andre studerte ultramafiske bergarter langs Trøndelag-Jämtland grensen er observert og beskrevet. Det kan tyde på en sammenheng mellom Slipsteinsberget og serpentinittbeltet mellom Røros og Snåsa.

Ved å kombinere observasjoner fra denne oppgaven med publiserte artikler er det mulig å argumentere for en serpentinittdannelse ved åpningen av Iapetushavet i en overgangssone mellom hav og kontinent. Før og under den Kaledonske fjellkjededannelsen, ble de serpentiniserte ultramafiske kroppene skjøvet over den Baltiske kontinentplaten og senere protrudert langs bratte forkastninger grunnet tetthetsforskjeller til de omkringliggende bergartene. De metamorfe forholdene nådde trolig grønnskifer-facies. Senere har CO_2 rike hydrotermale væsker metasomatisert serpentinittene til den sonerte ultramafiske kroppen på Slipsteinsberget i dag.

Acknowledgments

Siren Ånestad

x

Table of Contents

XII

List of Figures

XIV

List of Tables

List of Abbreviations

AMS	Anisotropy of Magnetic Susceptibility
BSE	Backscatter Images
EDS	Electron Dispersive X-ray Spectrometer
GMS	Ground Magnetic Survey
IGRF	International Geomagnetic Reference Field
MD	Multidomain
MTFC	Møre- Trøndelag Fault Complex
NGU	Norwegian Geological Survey
NRM	Natural Remanent Magnetization
OCC	Oceanic Core Complex
OCT	Ocean to Continent Transition
PPL	Plane Polarized Light
PSD	Pseudosingle Domain
PT	Pressure and Temperature
SD	Single Domain
SEM	Scanning Electron Microscope
SI	System of Units
SNC	Seve Nappe Complex
TMI	Total Magnetic Field Intensity
WGR	Western Gneiss Region
XRD	X-Ray Diffraction
XRF	X-ray Fluorescence
XPL	Cross Polarized Light

Table 1: Abbreviations in alphabetical order

1 Introduction

1.1 Sparbu Serpentinite Quarry

Slipsteinsberget is a serpentinite quarry located approximately 17km south of the town of Steinkjær, close to the village of Sparbu, Trøndelag county, Norway. The quarry is situated on a small hill that rises 20-30m above the surrounding garnet mica-schist and covers an area of nearly 20 000km^2, as seen in Fig 1-1. Slipsteinsberget is mainly composed of serpentinite with talc and soapstone in the outermost edges. The history of the quarry dates back to the early 11th century, where soapstone vessels were produced on a large scale (Østerås, 2017), and is today one of the largest soapstone quarries in Norway (Storemyr, 2015). The production lasted throughout the Viking Age and the Middle Ages, and it has been estimated that between 9,000 – 18,000 pots were produced during this time (Mortenson, 1973; Storemyr & Heldal, 2002). Traces of medieval activity can still be seen in some parts of the area. Several centuries later, the quarry was also used by the Germans during their Second World War occupation, for strategic powder production (Østerås, 2017).

In more recent years, the quarry was owned by A/S Lilleberg Verk, where they exploited the serpentinite for "dimension stones", a prized building material that is capable of taking on an attractive polish. The serpentinite resembles the exclusive brecciated Italian "Verde Antico" serpentinite (Mortenson, 1973) and can be observed at numerous buildings in Norway, such as the University of Oslo, Trondheim Congress Centre and the main post office in Bergen. Today, the quarry is owned by Solberg Steinindustri. Unfortunately, production stopped in 2006 due to low international market prices, however the quarry still holds many resources, and the factory is nevertheless intact.
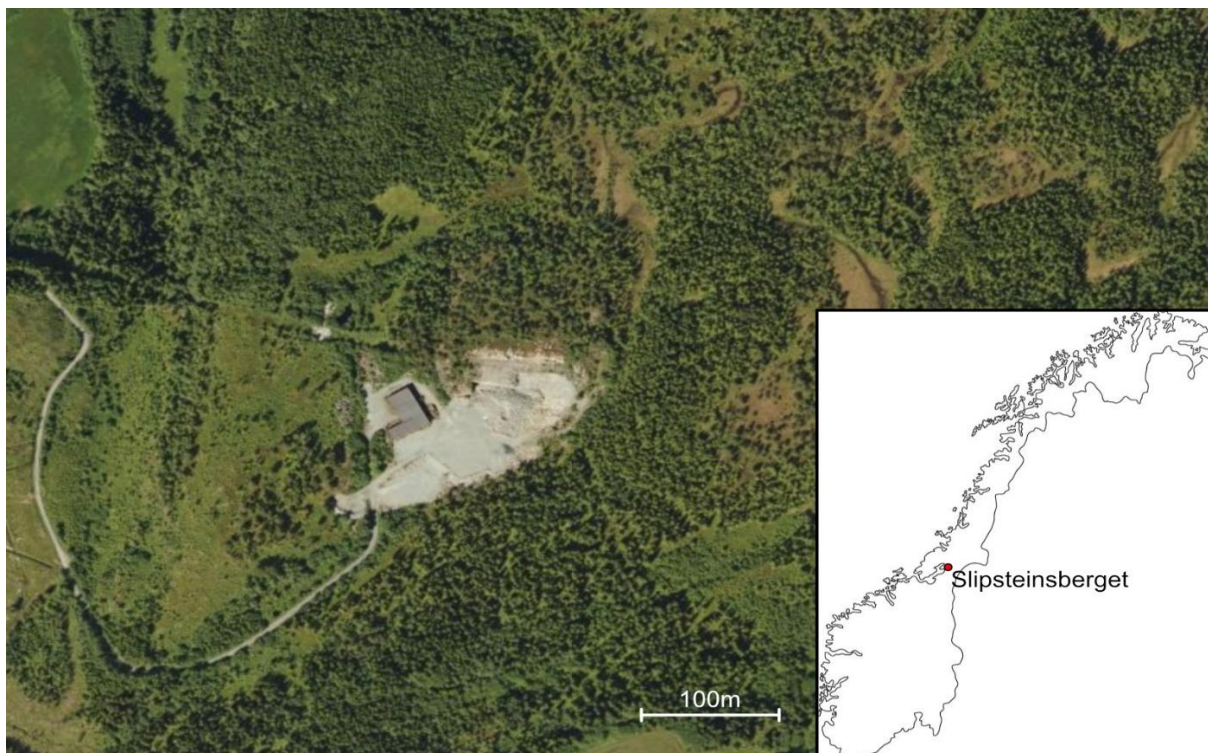
Figure 1-1: Orthophoto of the quarry taken from norgeibilder.no. Slipsteinsberget location is marked in red on the inserted map of Norway.

1.2 Previous Work

Extensive archaeological work has been carried out at Slipsteinsberget as it is an important historical site in Norway. This work has resulted in numerous articles documenting the history of the quarry and how soapstone has been used throughout time (Storemyr, 2015; Storemyr & Heldal, 2002; Østerås, 2017). However, these articles lack a comprehensive geological assessment of the quarry, and they tend to overgeneralize its lithologies.

The previous owner Lilleberg Verk A/S, with the help of Hultin (1964) and NGU, produced a report with a generalized map and drill logs taken from Slipsteinsberget. The drill cores were aimed at testing the quality of the talc and did not focus on serpentinite.

A few years later, Mortenson (1973) did a much more detailed geological investigation of the quarry, which is considered to be the main published report up until today. Mortenson (1973) mapped both Slipsteinsberget and two other ultramafic bodies, Smulstuen and Bakaunberget, as serpentinite bodies within the Sparbu municipality. He also compared the ultramafic bodies in Sparbu to other serpentinite bodies in north Østerdalen and Gudbrandsdalen. However, his main focus was on Slipsteinsberget. Mortenson (1973) separated Slipsteinsberget into three lithologies; serpentinite in the middle, talc in the edges, and mica-schist around the quarry, as shown in Fig 1-2. Furthermore, he also made three interpreted profiles across the quarry. As this report was written in the 70's, modern-day outcrop evaluation technologies were not yet developed, and a depth estimate for the serpentinite was not made. He also chose to map Slipsteinsberget as one big homogeneous body despite detecting an internal zonation.

Slipsteinsberget is also included in the Norwegian Geological Survey's (NGU) "Stiklestad bedrock map" (Roberts, 2010) along with three other ultramafic rock outcrops within Sparbu municipality. The mapping of Slipsteinsberget is very generalized and the legend is broad, however, but it does give a good tectonostratigraphic overview of the area.
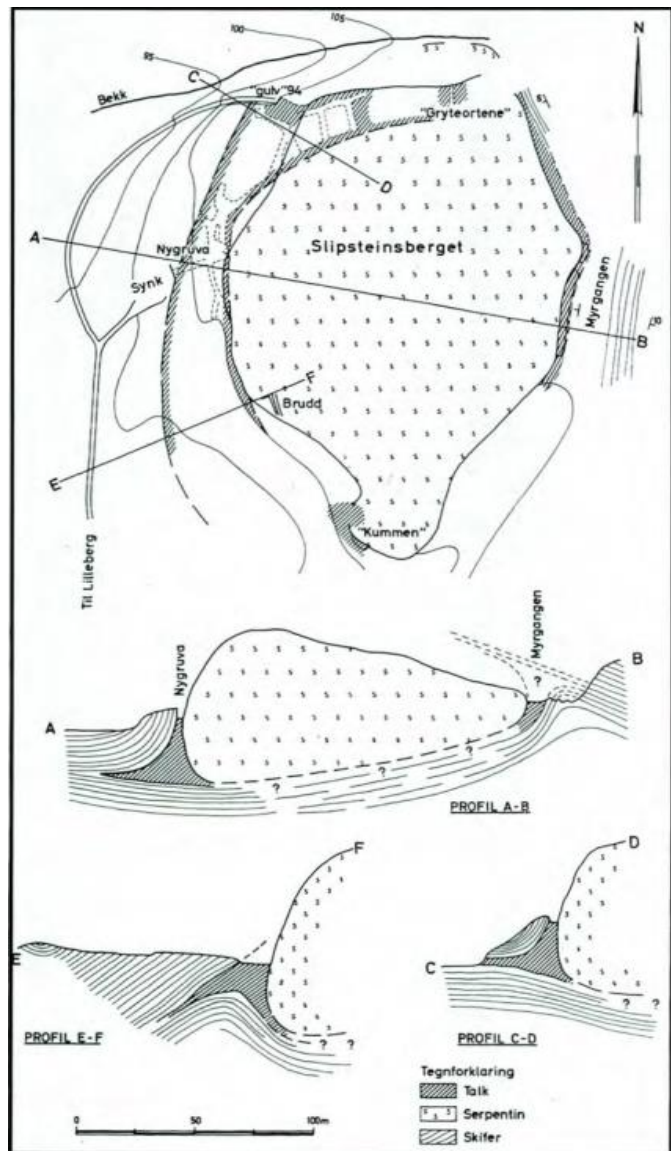
Figure 1-2: Geological map and cross-section along the quarry. Figure from Mortenson (1973).

1.3 Aim of Study

Isolated ultramafic metamorphosed bodies of minor size are still a matter of research regarding genesis, composition, and geometry. They are located in several places in mid-Norway but are especially abundant in zones extending between Bergen, Røros, and Snåsa. Ultramafic bodies are also located in the area around Sparbu, northern Trøndelag, with a prominent example being Slipsteinsberget, the study of this master thesis. As the rocks of Slipsteinsberget are well exposed, it gives an excellent opportunity to investigate rocks that usually occurs at much greater depths. The obtained petrological and mineralogical information is used to understand as much as possible of Slipsteinsberget's metamorphic history and possible correlations to other ultramafic rocks in Norway.

The second aspect of this master thesis is directly linked to the production of dimension stones. Apart from the previous generalized mapping of Slipsteinsberget (Mortenson, 1973), there is no present-day map or model that demonstrates the distribution of the different rock types within Slipsteinsberget, nor their subsurface 3D geometry. If Slipsteinsberget is again to open for production of dimension stones, the distribution of the different minerals and rock types, and hence the appearance, is essential.

This study aims to improve the model presented by Mortenson (1973) and, in general, the understanding of isolated metamorphosed ultramafic bodies in several aspects, including:

1) Examine and describe the internal "facies" associations and geometries within Slipsteinsberget's ultramafic body, using and integrating available methods:
   a. Field mapping
   b. Sample investigations in the lab (density, susceptibility, natural remanent magnetization, and X-ray diffraction)
   c. Microscopy (optical microscopy and scanning electron microscopy)
2) Investigate how magnetic methods might help quantify and model the serpentinites in the subsurface of Slipsteinsberget, including identification and characterization of magnetic minerals.
3) Create an updated geological map, geometric subsurface model, and volume estimate of the serpentinites.
4) Create a detailed magnetic characterization of Slipsteinsberget's ultramafic body that can be used as an analog, helping to understand other, less-studied ultramafic bodies elsewhere.
5) Attempt to reconstruct the formation and metamorphic history of Slipsteinsberget.

2 Geological Setting

Ever since the onset of plate tectonic in the early history of the Earth, its crustal plates have drifted, and new oceans, continents, and mountain ranges have been created and evolved through time. The oldest rock recorded in Norway is from the Archean Eon, a 2900Ma old gneiss from Sør-Varanger (Nordgulen & Andresen, 2013). In comparison, the rocks found close to Slipsteinsberget are much younger with age from Neoproterozoic to Late Cambrian (Mortenson, 1973; Roberts, 2010). Since the formation of the oldest rocks in Norway, the Fennoscandian shield has expanded and experienced both rifting, magmatic activity, and the creation of mountain ranges (e.g., the Svecofennian-, the Gothian, the Sveconorwegian-orogeny, and the Caledonian orogeny) (Nordgulen & Andresen, 2013). The Fennoscandian shield amalgamated with other shields during the Sveconorwegian orogeny, resulting in the formation of the supercontinent Rodinia in Late Mesoproterozoic (Bogdanova et al., 2008; Slagstad et al., 2017). This supercontinent lasted approximately 150 million years after its complete assembly (Li et al., 2008). According to Li et al. (2008), mantle avalanches and thermal insulation led to the formation of a mantel superswell beneath Rodinia. This resulted in continental rifting, and episodic plume events between 825Ma to 740Ma, whereupon the supercontinent was broken up, and Norway was left as a part of the Baltica paleocontinent (Nordgulen & Andresen, 2013). Parts of Vestlandet, Rondane, Drovre, and Trøndelag still hold bedrocks from this time and reflect the break-up of Rodinia (Nystuen, 2013).

In the Precambrian, the Baltic continent once again started to fracture (Nystuen, 2013). A fissure formed in the crust in the middle of the "belt of sea" and started to separate Laurentia from Baltica (Nystuen, 2013). Basaltic lava from the mantle surged upwards through this fissure and resulted in crustal stretching and thinning, and later on faulting (Roberts, 1997). Thick sand deposits were deposited at this time, and the landscape was dominated by rivers (Roberts, 1997). An increasing degree of stretching and faulting in ~650Ma to ~580M allowed basaltic magma to intrude into the overlying thick sand deposits, resulting in dolerite dikes (Roberts, 1997). Further to the present-day geographical west, the upper crust experienced even more extensive stretching and thinning that led to a significant abundance of basaltic intrusions (Roberts, 1997). The rivers gradually evolved into a new ocean through seafloor spreading, the Iapetus Ocean (Nystuen, 2013; Roberts, 1997). The opening of the Iapetus Ocean was initiated at a junction between a rift (Laurentia-Gondwana), a right-lateral fault (Laurentia-Baltica), and a trench (inverted Baltica-Gondwana) (Hartz & Torsvik, 2002). The Baltica continent was then flooded as the spreading ridge rose and displaced the seawater over the worn-down Baltica (Nystuen, 2013).

In the Cambrian (500Ma), Baltica and Laurentia started to move towards each other, and island arcs formed in the Iapetus Ocean due to the early subduction of the Baltic plate (Fossen et al., 2013; Rey et al., 1997). The island arc collided with Baltica in ~500Ma to ~490Ma and resulted in the first Caledonian deformation- and metamorphic event, the "Finnmarkian" phase (Roberts, 1997). The island arc, and some of the seafloor, was thrusted onto Baltica in an eastward direction along with other newly formed nappes, such as the Skjøtningen- and Leksdal Nappe that originated from the transition zone between the continent and the Iapetus Ocean (Roberts, 1997). Later, sedimentary facies from shallow-water carbonates to deep-marine terrigenous turbidite were deposited in an Ordovician-Silurian sequence (Roberts & Wolff, 1981). The convergence continued throughout Ordovician and Early Silurian time and resulted in a continent-continent collision at 430Ma (Corfu et al., 2014). This collision lasted for approximately 30 Ma into the

Early Devonian (Corfu et al., 2014) and led to a new deformation- and metamorphic event (Roberts, 1997). Baltica subducted beneath Laurentia where the high- and ultrahigh-pressure rocks of the Western Gneiss Region (WGR) reached Baltica's maximum burial depth at 410Ma to 400Ma (Andersen et al., 2012; Butler et al., 2015; Corfu et al., 2014; Rey et al., 1997). The collision between the continents resulted in the Scandian Orogeny and an accretionary wedge consisting of major thrust-units (with a general south-east imbrication), and form most of Norway's landscapes today (Corfu et al., 2014; Rey et al., 1997). The conventional way of describing the Scandinavian Caledonides is to use the nomenclature "allochthons". Traditionally, the Scandian Caledonides are divided into a Lower-, Middle-, Upper, and Uppermost-allochthon, with their respective derivation from and between Laurentia and Baltica (Gee & Sturt, 1985).

Since the comprehensive study of the Caledonian orogeny by Gee and Sturt (1985), modern-day technologies have unraveled new facets of the geology of the orogeny. Corfu et al. (2014) and Jakob et al. (2017) explain how Baltica could have been amalgamated with the Avalonian plate in the time of the collision with Laurentia, and that the Caledonian margin of Baltica might have been facing different seaways and terrains during its course northwards. Furthermore, Andersen et al. (2012) and Jakob et al. (2017) suggest that the pre-Caledonian margin of Baltica might have been stretched into a hyperextended crust that is represented by a mélange zone of mantle peridotites in southern Norway today. Furthermore, the nature of the Finnmarkian event is also debated. There are some agreements about the involvement of arc/continent collision (Torsvik & Cocks, 2005), but its age and a single formation event are argued (Corfu et al., 2014). However, the Finnmarkian event is used in this thesis to explain the basics of an earlier obuction event before the main Caledonian event.

These new findings challenge the traditional way of describing the Scandian Caledonides, and a reinterpretation of the allochthons and the Caledonian Orogeny is warranted (Andersen et al., 2012). Corfu et al. (2014) also discuss how the use of allochthons can lead to misconceptions. However, seen on a bigger scale, the main features of the allochthons can still be applied. Concerning this master thesis, which is focused on a small area, the terms (and concept of) segments, groups, and nappes, as seen in Fig 2-1, are used.
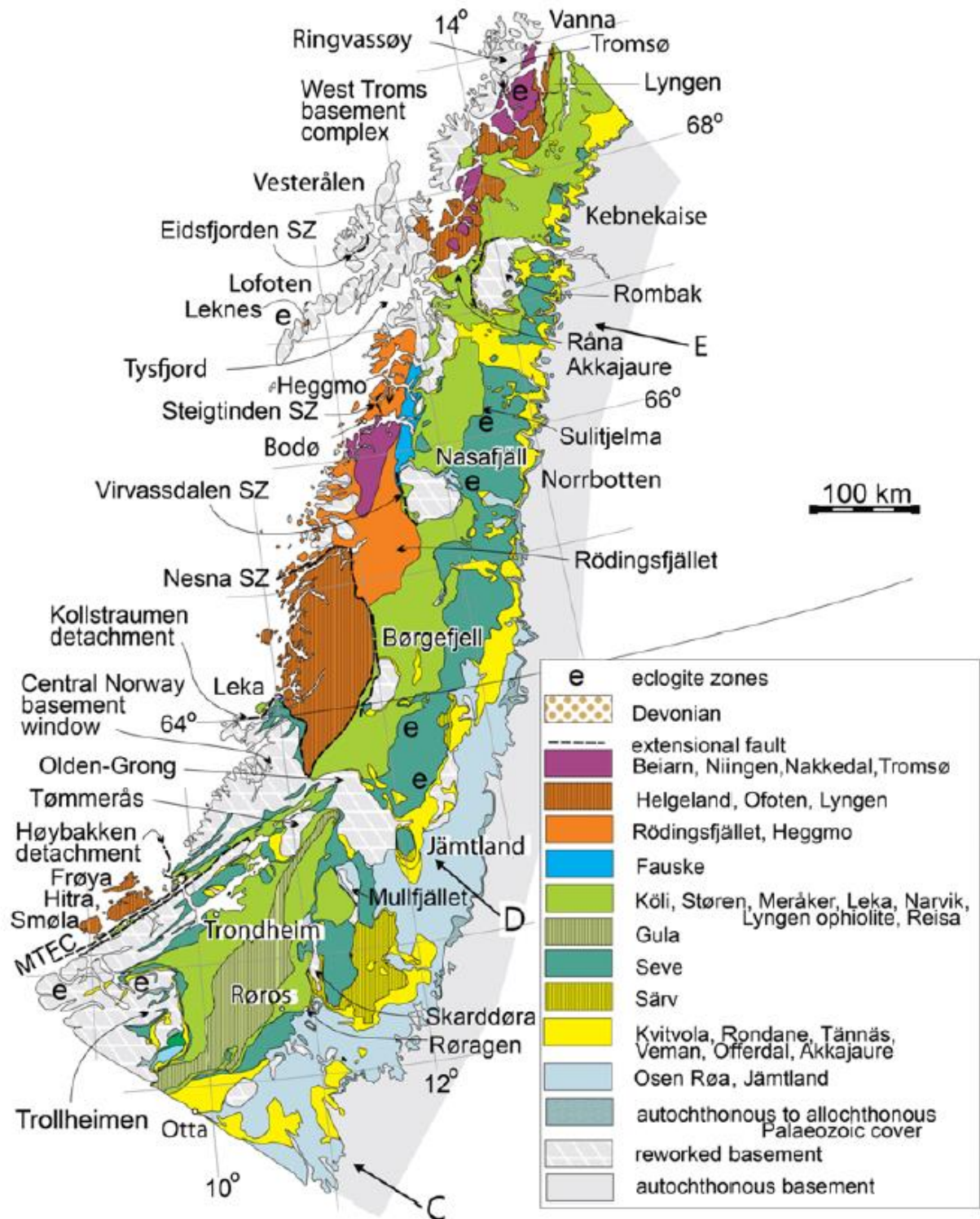
Figure 2-1: Tectonic map of central Norway. MTFC: Møre- Trøndealg fault complex; SZ: shear zone. Figure from Corfu et al. (2014).

In the Early Devonian (ca. 405Ma), the convergence came to an abrupt end, switched to an east-west extensional regime, and the subducted slab started to exhume (Fossen, 2000; Rey et al., 1997). The newly formed extensional regime reactivated former thrust zones that now acted as extensional décollement faults on the western margin of Baltica (Rey et al., 1997). Several papers (Bjørlykke & Olesen, 2018; Nasuti et al., 2012; Osmundsen et al., 2006; Seranne, 1992) have located multiple Late-Caledonian detachment zones in mid-Norway. One of the most prominent ones is the Møre-Trøndelag Fault Complex (MTFC). The MTFC is an Early to Middle Devonian east-northeast oriented fault zone that still has parts that are seismically active today (Gabrielsen et al., 1999). In the Devonian, it had a deep sinistral strike-slip movement that exerted an important geometrical control in the Trondheim region (Corfu et al., 2014; Gabrielsen et al., 1999; Nasuti et al., 2012). The MTFC has experienced multiple reactivations from the Devonian to the present (Seranne, 1992) and can, to some extent, be followed offshore utilizing geophysical data (Nasuti et al., 2012). The fault complex, along with other faults, can be detected through airborne magnetic and gravimetric maps, as shown in Fig 2-2. In addition to this, the post-Caledonian faults can be identified from lineaments in the present-day topography.
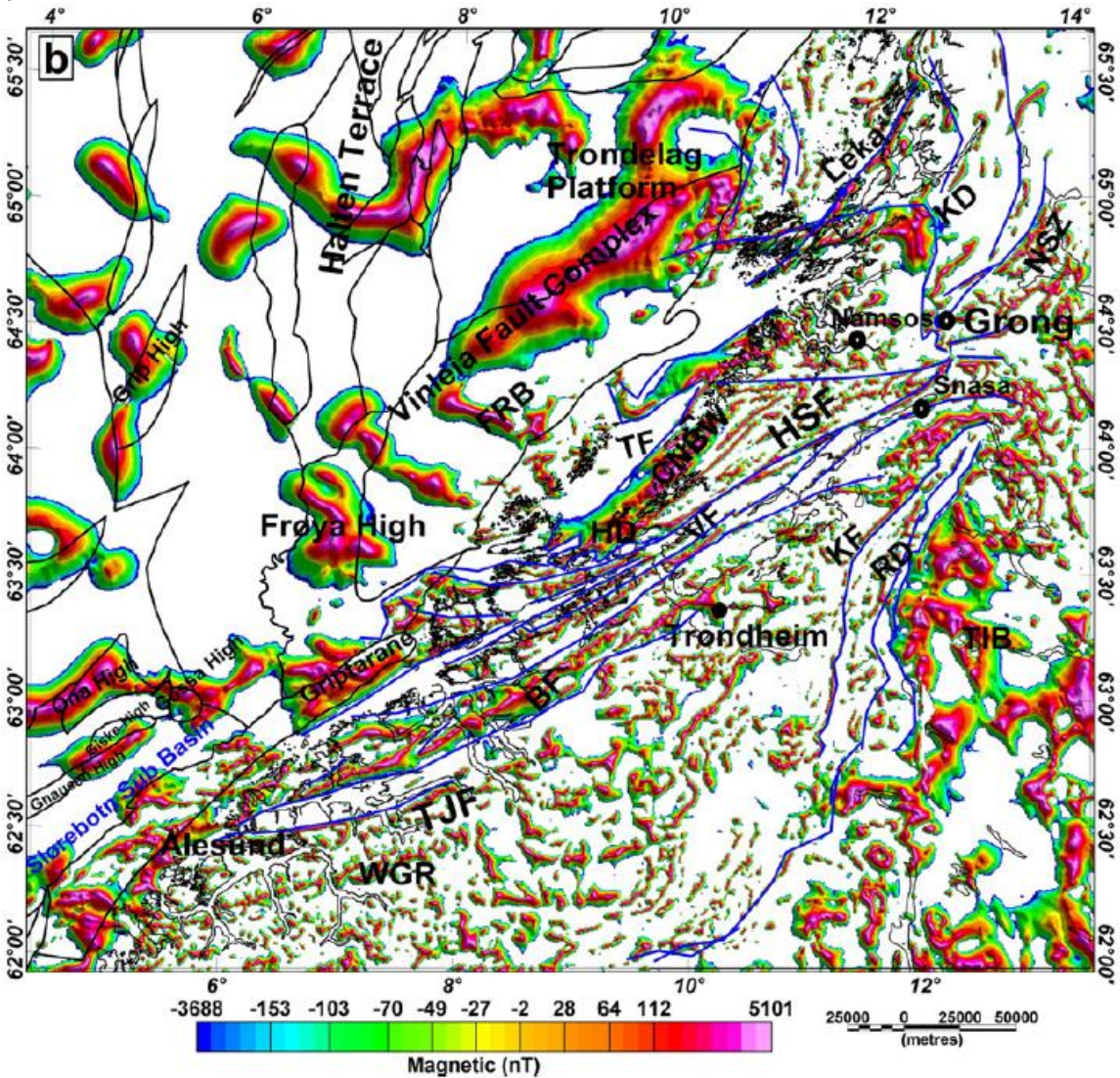
Figure 2-2: Tilt derivative of magnetic anomalies. Only the positive values of the til derivative are shown. CNBW= Central Norwegian basement window, HSF= Hitra-Snåsa Fault, KD= Kollstraumen Detachment, RD= Røragen Detachment, TF= Tarva Fault. TJF= Tjellefonna Fault, VF= Verran Fault, WGR= Western Gneiss Region. Figure from (Nasuti et al., 2012).

7

Slipsteinsberget is located in Trøndelag and is a part of the Seve Nappe complex (SNC), which geographically is known as the Skjøtingen Nappe (Nilsson et al., 2014; Roberts, 2010). Tectonically, it rests on the Leksdal Nappe and is overlaid by the Støren Nappe (Bjørlykke & Olesen, 2018; Corfu et al., 2014; Mortenson, 1973; Nilsson & Roberts, 2014; Roberts & Wolff, 1981). This area is affected by the MTFC in the west as well as other Late-Caledonian detachment zones (Bjørlykke & Olesen, 2018; Seranne, 1992). Fig 2-3 shows a simplified geological map of the area.
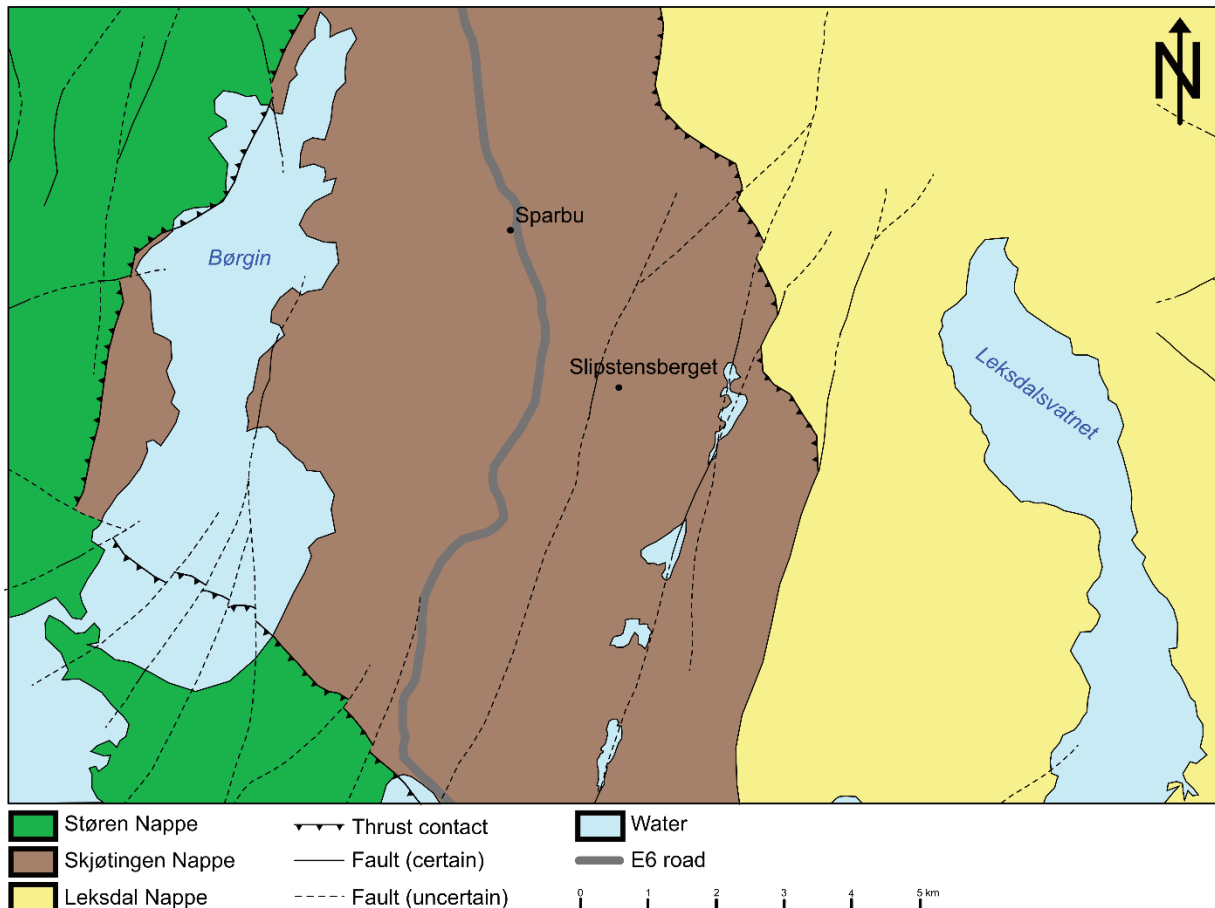
Figure 2-3: Simplified tectonostratigraphic map of the Sparbu area showing the location of Slipsteins-berget. Modified after Roberts (2010).

The Leksdal Nappe mainly consists of Neoproterozoic meta-arkoses and meta-sandstones with minor augen gneisses and mylonites (Roberts & Wolff, 1981). The metasediments are interpreted to derive from a continental margin during the pre- to syn-rifting of the Iapetus Ocean (Jakob et al., 2019). The break-up of Iapetus resulted in abundant metadolerite dikes (ages of 650Ma – 580Ma (Roberts, 1997)) within the Leksdal Nappe and the overlying Skjøtningen (Seve) Nappe (Jakob et al., 2019; Ladenberger et al., 2014; Nilsson et al., 2005; Tegner et al., 2019). Later, during the Finnmarkian event in Ordovician, the nappe was thrusted onto Baltica (Roberts, 1997) and now rests on the Precambrian basement rocks (Wolff, 1976). Furthermore, the Leksdal Nappe is likely correlative of the Särv Nappe on the Sweden side of the border (Roberts & Wolff, 1981; Wolff, 1976).

The Skjøtingen (Seve) Nappe is of Neoproterozoic to Late Cambrian age (Mortenson, 1973; Roberts, 2010) and is generally of a higher metamorphic grade than the over- and under-lying nappes (Corfu et al., 2014) as it is assumed to have undergone two phases of metamorphism. (Roberts, 1997). The Skjøtingen Nappe is dominated by amphibolite-facies schists and gneisses (Nilsson et al., 2005), but also minor amphibolites, marbles, and

8

serpentinized peridotites (Corfu et al., 2014; Roberts & Wolff, 1981). The located perido-tites are associated with metasedimentary schist and felsic gneisses and occur as lenses (Corfu et al., 2014). The Nappe also holds dolerite dikes and gabbros that intruded the nappe in 605 Ma – 610Ma (Corfu et al., 2014; Tegner et al., 2019) during the opening of the Iapetus Ocean (Jakob et al., 2019). Regionally, the SNC experienced diachronous am-phibolite to eclogite metamorphism in the Early to Late Ordovician (Jakob et al., 2019) and was thrusted upon Baltica during the Finnmarkien event (Roberts, 1997). Furthermore, Wolff (1976) suggests that the amphibolites are metamorphic products of the tectonos-tratigraphically overlying Støren Nappe basalt-lavas. Later, in Silurian, the Skjøtingen Nappe experienced a lower-grade metamorphic event during the Caledonian orogeny (Roberts, 1997).

The overlying Støren Nappe consists of lower-grade metamorphosed sedimentary and vol-canic rocks (mostly (pillow) basaltic greenstone (Roberts, 1997; Roberts & Wolff, 1981)) of assumed Cambrian and Ordovician age with some minor plutonic rocks, conglomerates, and peridotites (Roberts, 1997, 2010; Wolff, 1976). The Støren Nappe is a part of the Trondheim's Nappe complex (Roberts, 1997; Wolff, 1976) and is often correlated to the Meråker and Køli Nappe (NGU). According to Roberts (1997), the Støren Nappe has an oceanic affinity corresponding to the Iapetus Ocean's seafloor and island arcs resulting from a converging setting. Corfu et al. (2014) further assign the Støren Nappe to the Laurentian side of the Iapetus Ocean. Remains of the oceanic history are today observed as ophiolites within the Støren Nappe (Grenne, 1988).

3 Methods

To understand both the variation in geology within the quarry and the relationship to the surrounding rocks, a wide variety of methods were used in this master project. As some research has been conducted in the area beforehand ((Hultin, 1964; Mortenson, 1973; Roberts, 2010; Storemyr & Heldal, 2002), the methods were chosen in such a way that they built on the previous work and produced new raw data, analysis, and interpretation.

3.1 Fieldwork

Slipsteinsberget is located approximately 100km northeast of Trondheim, as seen in Fig 1-1. It was, therefore, most efficient to take several day trips to the field area instead of renting a place at Sparbu. This decision made it possible to look at the weather- and geo-magnetic- forecasts in advance and to choose the optimal days for fieldwork. Outcrop samples and measurements were taken during each trip and were furthered processed at the lab immediately after return. This instantly increased the understanding of the field area and contributed to more efficient fieldwork on successive trips to the field.

3.1.1 Geological Mapping

All mapping was carried out digitally using the software FieldMove (Petroleum Experts) on an iPad with GPS. FieldMove allows the user to import georeferenced background maps such as orthophoto, geological-, LiDAR- and magnetic- maps over the field area. This has numerous advantages when it comes to geological mapping. Different rocks have different properties that can be represented by different colors displaying, e.g., topography, vege-tation, or magnetic susceptibility. The use of corresponding background maps can, therefore, improve geological mapping quite significantly. Another advantage of digital mapping is the possibility to draw outcrops and add structures directly on the map. This gives an excellent "real-time" overview of the field area, and the relationships between outcrops and, for example, lithologies can be observed. Besides this, FieldMove directly plots all the measurements into stereonets, which makes it possible to detect trends al-ready in the field. Although the iPad has a GPS with an accuracy of 5m, a handheld Garmin GPSMAP 62stc was always carried alongside as a backup. A Brunton compass was used to measure all the structures in the field area, which were then plotted manually into Field-Move. Dip and dip direction were used for planar measurements, while trend and plunge were used for linear measurements. Occasionally, when the compass was very close to a highly magnetic rock, the compass needle could experience a 5-15 degree shift. Therefore, the reliability of the measurements taken in the highly magnetic core needs to be consid-ered before further processing.

3.1.2 Susceptibility Measurements

A handheld KM-7 Kappa magnetic susceptibility meter was provided by the Department of Geoscience and Petroleum at NTNU. This instrument can detect readings of $\pm999\text{x}10^{-3}$ SI units with a sensitivity of $1\text{x}10^{-6}$ SI units (StatisGeo, n.d.). This made it possible to measure the outcrops on location to get a rough estimate of the rock's magnetic properties imme-diately. Because the susceptibility can vary within the same rock, multiple measurements were taken for each (small) area. For the later analysis, a mean value was used when the measured values were close, and a range of values was used when the measured values varied a lot. Two susceptibility-profiles within the quarry were acquired, as well as individ-ual locations in order to map the surrounding areas. Location coordinates were recorded for all measurements.

10

3.1.3 Oriented Samples

Outcrop samples were selected with two aims: to be representative of each different lithology, and to capture the range and variability of magnetic susceptibilities independent of lithology. A good overview of the expected susceptibility values was needed before selecting which rocks to sample. The orientation of the samples was measured in-situ, photographed, and marked by a waterproof marker before they were taken out by hand with a hammer and chisel (and occasionally a sledgehammer). All samples were oriented, except for three samples that were only needed for X-ray diffraction (XRD). The sample size varied depending on their homogeneity. Large samples were taken in the case of heterogeneous rocks in order to obtain a representative result.

3.1.4 Ground Magnetic Survey

The ground magnetic survey was done during one of the last days of fieldwork when the solar activity was low. An understanding of the geometry and properties of the quarry was needed in order to decide which survey lines to walk. The survey lines within the quarry were intended to be as straight as possible and intersect at multiple places, by walking in roughly north-south and east-west directions. Care was taken not to walk too close to the steep walls to prevent the additional effects of edges and topography. Due to the dense vegetation and steep topography outside the quarry, however, the path choices were quite limited and therefore resulted in a more random pattern, as shown in Fig 3-1a. A Geometrics G-859AP Mining Magnetometer was provided by the Department of Geoscience and Petroleum at NTNU. The magnetometer has a cesium sensor with a sampling rate of up to 5 readings per second, with an accuracy of 0.008 nT. In addition to this, it has an integrated NovAtel Smart VI GPS, with an accuracy of 3m, which saves the mapping positions automatically to the readings (Geometrics, 2011). The mounted cesium sensor was oriented in a 45-degree tilted position to obtain the strongest magnetic signal. See Fig 3-1b for fieldwork setup. The magnetometer measures the total magnetic field intensity (TMI). Consequently, human-made magnetic objects not belonging in nature, i.e., cultural noise, was also included in the readings and had to be excluded later in the data handling. Fortunately, the field area is located in a remote place, and the effect of cultural noise was therefore limited. The field area includes an old factory, a dead power line, two longstanding mining entrances, and an old drill rig.

The XYZ-file obtained from the ground magnetic survey was loaded into Geosofts modeling software Oasis montaj for further processing. Drop-
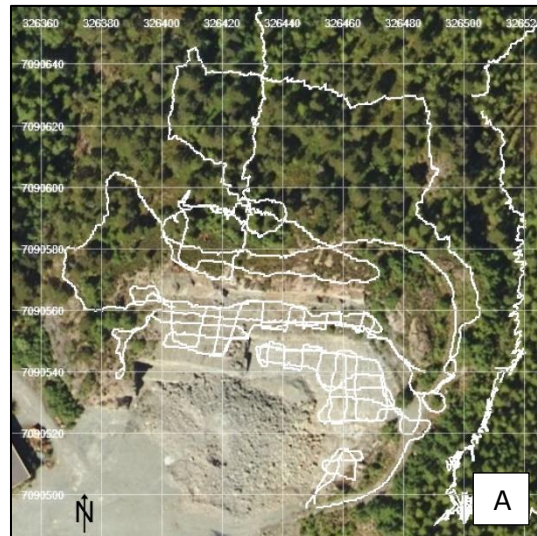
Figure 3-1: **A**: *Ground magnetic survey lines over Slipsteinsberget superimposed on an ortophoto image from norgeibilder.no* **B**: *Setup of instrument on-site. Photo: Zeudia Pastore*

outs, or so-called zero-readings, were excluded from the results and spikes, or abrupt impulses were manually removed. The edited XYZ-file was then gridded using minimum curvature (Dentith & Mudge, 2014) with a cell size of 1m to detect small spatial magnetic variations. The locations assumed to generate cultural noise were compared with the gridded magnetic data. Only the drilling rig made a detectable signal which was removed from the data. However, concerning the long history of the quarry, its underground tunnels, and archeological findings on-site, there is a chance that the data still contains undetected objects that can cause a superficial anomaly.

3.2 Sample preparation

3.2.1 Drilling Cores and Cylinders

To further process the oriented outcrop samples at the NTNU lab, they first had to be drilled into small cores and cut into cylinders with a specific volume. It was important that the samples had the proper geometry to fit into instruments, and that they had the same volume so they could be compared easily. In total, 57 cylinders were created from 9 samples. The number of cylinders created from the same sample varied depending on the homogeneity of the rock. Samples with a high degree of lithological variation were cut into several cylinders, while homogeneous samples were not. However, a minimum of 3 cylinders were produced from each sample. They were created by first drawing additional lines on them, parallel to the already existing markings, to maintain their orientation through drilling. The samples were then placed in a drill press with the marked oriented surface facing upwards. A bubble leveler was used to make sure the surface was oriented as horizontal as possible. Because the samples were collected by hand on-site, it was rare to have an entirely flat surface. Therefore, the prioritized horizontal surface was the same part of the surface that was measured in the field. A diamond drill bit with an inner diameter of 1 inch was then used for drilling the cores. See Fig 3-2 for setup. The cores were again marked right after drilling to keep control of the orientations. The cores from sample 12 were fragile and contained many cracks. They were glued and placed in a vacuum container for drying to obtain a stronger core for further processing. After that, each core was cut into cylinders with a length of 19-21mm on a diamond

Figure 3-2: Drilling cylinders on the marked surface.
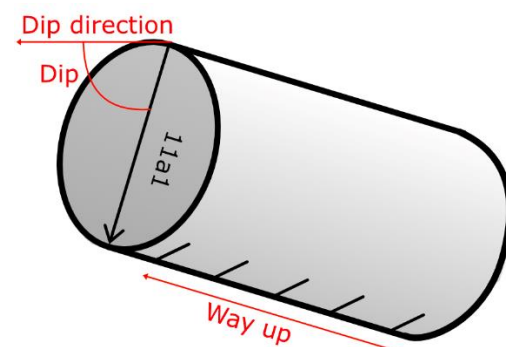
Figure 3-3: Illustration of cylinders with orientations.

blade saw. Finally, the cylinders were named and marked as indicated in Fig 3-3 The first number shows which sample it comes from, the second letter (A, B, C, or D) identifies which core and the last number shows its position (1=top, 2=middle, or 3= bottom).

3.2.2 Production of Thin Sections

All samples were cut into small rectangular squares before they were given to the professionals working at the Thin section Laboratory at the Department of Geoscience and Petroleum at NTNU for finishing. Due to the high demand at the institute, only 12 thin sections could be requested each time. Oriented thin sections were cut parallel to the dip direction to allow the detection of kinematic indicators. Furthermore, all the samples were ethanol-treated to avoid possible swelling. The thin sections, with a size of 28x48 mm and a thickness of 30µm, were polished and later on carbon-coated for SEM.

3.2.3 X-Ray Diffraction (XRD)

Some minerals were quite challenging to distinguish in the field, and some samples appeared to have the same lithology but had different magnetic properties. To get a better understanding of the rocks and their mineralogy, X-ray diffraction (XRD) was carried out quite early in the project. The samples were first manually crushed down into grain sizes of < 5 mm in a Fly Press Rock Crusher. Fifty grams of the samples were then selected with the help of a randomized sorting tool, a splitter. Next, they were placed in a grinding set of tungsten carbide and positioned in a vibratory disc mill for further crushing. When the desired grain size was obtained (< 40 µm), they were crushed one final time in a micronizing mill, in a tube of agate pebbles and ethanol. Fig 3-4 shows some of the crushing steps. The sample crushing tends to flatten the grains. For this reason, the crushed samples were poured into petri dishes, ethanol was added, and they were in a 100°C heated cabinet for an hour. This was done to reconstruct the initial shape of the minerals. After all the ethanol was evaporated away, the samples were cooled and stirred in the petri dish. Finally, they were placed on a disc holder and were ready for analysis.
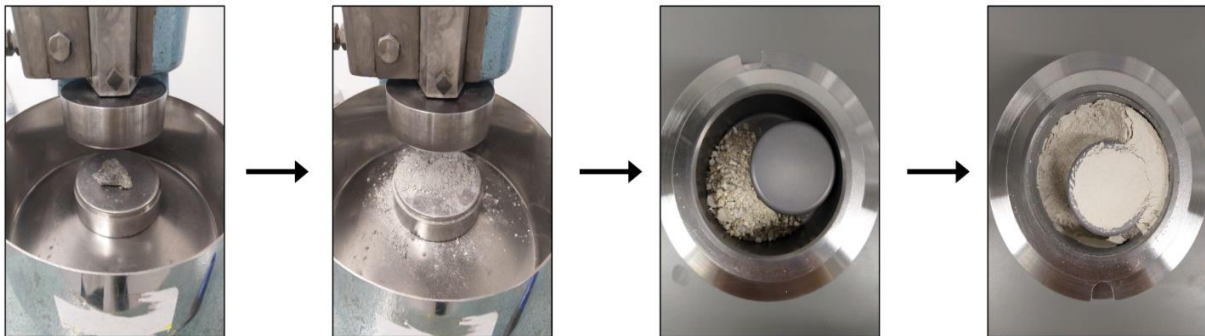
Figure 3-4: Visual illustration of the grain size during crushing and milling.

3.3 Laboratory Work

All the laboratory work was conducted in the labs of the Department of Geoscience and Petroleum at NTNU.

3.3.1 Density

Density is a measurement that compares the mass of an object to its volume. Rock density depends on mineralogy, pore fill, and fracture content (Dentith & Mudge, 2014). As most rock types have known, standard density ranges, it is possible to compare these to measured values to get an indication of the geological processes that may have led to any deviation from the standard values. The density of all the 57 cylinders was calculated based on Archimedes' Principle:

$$Measured\ immersed\ weight = Weight_{in\ air} - Weight_{of\ displaced\ fluid} \qquad (1)$$

Weight can be rewritten:

$$Weight = \rho * V * g \qquad (2)$$

Where ρ =density [g/cm^3], V=volume [cm^3] and g =gravity [m/s^2]. The density of distilled water is assumed to be ~1 g/cm^3, and the density of air is effectively 0 g/cm^3. When a sample is fully submerged, the volume of the object will be the same as the volume of the displaced fluid. Because gravity is a constant, equation 1 can be reformulated:

$$\rho_{cylinder} = \frac{Weight_{in\ air}}{Weight_{of\ displaced\ fluid}} \qquad (3)$$

The cylinders were weighed on a Mettler Toledo ML104 scale with an accuracy of four decimals. Each cylinder was measured both in air and submerged in water, as seen in Fig 3-5. The analytical balance was tared between each measurement to decrease errors. Weight $_{in\ air}$ was first measured for all the samples. Then, the samples were soaked in water for 24 hours. It was assumed that the possible gasses (e.g., O_2, CO_2), leading to an upward buoyancy force, would have been replaced by water after 24 hours. Finally, the weight $_{of\ displaced\ fluid}$ was measured.

3.3.2 Magnetic Susceptibility

A MFK1-A susceptibility bridge was used to measure the magnetization in the cylinders when an external magnetic field was applied to them. The relationship between the cylinders and the external magnetic field can be explained by equation 4:

$$M_{ind} = \kappa * H \qquad (4)$$

Where M_{ind} = induced magnetization in the cylinders, κ = magnetic susceptibility, and H = applied magnetic field. Before the measurements started, the susceptibility bridge was calibrated with a manufactured nonmagnetic cylinder of 8 cm^3 to obtain precise results. After 10 minutes, the susceptibility bridge was heated and ready to run. The cylinders were measured in three different directions to detect any signs of anisotropy of magnetic susceptibility (AMS). Fig 3-5 shows the instrument setup. The software, Safyr6, saved all the measurements into a big file and calculated the properties based on a sample volume of 1cm^3. The measured values were volume-corrected in the end, according to equation 5:

$$Volume\ corrected\ measurement\ [*] = \frac{Instrument\ reading\ [*] \times Assumed\ volume\ [cm^3]}{Real\ volume\ [cm^3]} \qquad (5)$$

*[SI] for susceptibility, [A/m] for natural remanent magnetization.

Clark (1997) conducted multiple tests on magnetite and monoclinic pyrrhotite, which resulted in an estimate for magnetite content:

$$\textbf{Volume \% magnetite} = \frac{\textbf{Susceptibility [SI]}}{\textbf{0,0347}}$$

(6)

3.3.3 Natural Remanent Magnetization (NRM)

An AGICO JR–6A spinner magnetometer was used to measure the NRM of the samples. The instrument was first calibrated with a manufactured standard cylinder of 8cm^3 to obtain precise and accurate results. Fig 3-5 shows the setup during a measurement. The grey lid acted as a shield that removed the present-day field and allowed the instrument only to measure the magnetization generated from the sample itself. As in the susceptibility bridge, anisotropy was taken into account and measured. An oscillating shaft made it possible to run the measurement in one go without having to turn the sample manually from each direction. The software Rema6W saved both the NRM values, its directions, and the % error into a single file. Care was taken not to let the error exceed 3%. If a sample had an error in excess of this, it was measured again at a lower speed to decrease the % error. Since the instrument used an assumed volume of 10 g/cm^3, the readings had to be corrected to the precise volume obtained in the density measurements by equation 5.
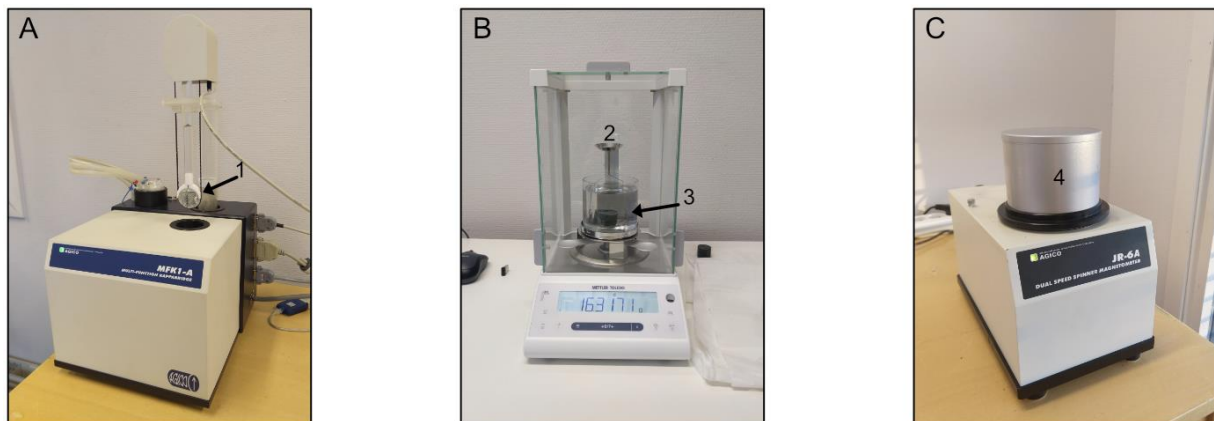
Figure 3-5: Instrument setups. **A:** *Susceptibility bridge.* **B:** *Analytical balance.* **C:** *Spinner magnetometer.* **1:** *Rotating sample holder.* **2:** *Weight in air.* **3:** *Weight in water.* **4:** *Field remover.*

3.3.4 X-Ray Diffraction (XRD)

The already prepared disc samples were inserted into a D8 Advanced. The two X-ray guns fired a beam with identical wavelength and phase at the disc samples and moved continuously in a vertical direction allowing a thorough scan at different angels. According to Bragg's Law, the diffraction angle is affected by the lattice spacing in the sample, *d*, which allows mineral identification.

A software (Diffrac.Topaz) transferred the readings into digital graphs with specific peaks at distinct angles that represented the different minerals. The software contains a database with over 40 000 minerals and helped to identify minerals to the corresponding peaks. When the mineral assemblages were found, the software Diffrac.Eva was used for quantifying them. Even though the software often came up with multiple mineral suggestions, it was essential to remember that all of these were not necessarily correct, and that they had to be further verified through, e.g., microscopy.

3.4 Microscopy

3.4.1 Optical Microscopy
All of the thin sections were investigated in a Leica polarizing microscope with both transmitted and reflected light. The transmitted light was used for mineral identification and observations of microstructures, while the reflected light was used for the identification of opaque minerals. There was a particular focus on identifying magnetic minerals and mineral assemblages to understand the magnetic expression of the rocks of the quarry as well as its zonation. As a guide, both Deer et al. (2013), Nesse (2012), and Passchier and Trouw (2005) were used.

3.4.2 Scanning Electron Microscope (SEM)
The minerals that could not be identified in optical microscopy were furthered investigated in the Department of Geoscience and Petroleum's SEM at NTNU. The carbon-coated thin sections were placed on a stage with standard height. The thin sections were inserted into a low vacuum chamber and placed under an electron gun with 15kV, an extraction voltage of 5,0-2,20kV, and a medium probe current of 15nA. The working distance was set to 15mm. When started, the SEM fired focused accelerated electrons towards the sample through an electromagnetic lens (Collett, 2007). When the beam of electrons hit the sample, it emitted back different signals that could be collected by various detectors either to form images or to perform spectroscopic analysis (Luo, 2018). The signal used in this master thesis is backscattered electrons (BSE) and X-rays.

The BSE signals were used for imaging the atomic number contrast. Higher atomic numbers have a stronger electron interaction and absorb electrons faster than lower atomic numbers (Inkson, 2016). Therefore, heavier elements will exhibit a light contrast while the lighter elements exhibit a darker contrast. SEM images in BSE mode is a convenient tool to characterize the distribution of, e.g., oxides.

An energy dispersive X-ray spectrometer was mounted on the SEM, which detects the different emitted X-rays from the sample. Each atom has a unique X-ray signature and is represented by an energy dispersive spectrum (Inkson, 2016). This resulted in a semi-quantitative chemical analysis that revealed the elements within a single point or over a small area. The data was represented by a specter of elements normalized to atom% or in a colored map of distributed elements over a given area. In combination with optical microscopy and XRD, the mineral phases could be identified using mineralogical tables.

It was essential to investigate thins section taken from the same locality as the cylinders to obtain a precise correlation between mineralogy and magnetic properties. This was achievable for samples 3 and 8. Unfortunately, it was not possible to accomplish this for sample 9 as this sample does not have any corresponding thin section. The closest sample, sample 2, was used instead, which is represented by the same rock type.

3.5 Core Logging
NGU's National Drill Core and Sample Center at Løkken stores seven drill cores from Slipsteinsberget. These were studied to get a better understanding of the lithological and magnetic property variations with depths in the subsurface. A portable Niton XL3 X-ray fluorescence (XRF) with a 3mm small spot-size and a mining Cu/Zn-sample type identified the elements of interest. Furthermore, a handheld magnetic susceptibility meter made a possible correlation between the XRF analysis and the core's magnetic properties. Both instruments belong to the Department of Geoscience and Petroleum at NTNU. In total, 117m of cores were located and logged.

4 Theory

4.1 Geomagnetic Theory

The Chinese are thought to be the first to use lodestone as a primitive direction-finding tool in the second century BC. It was not until the 12th century that the Europeans started to use a magnetic compass for navigation. Furthermore, it was not until 1600 that the first work on the Earth's magnetic field, conducted by William Gilbert, was published. Since then, the geomagnetic methods have been used in a wide variety of aspects, and they are a powerful tool when it comes to geological mapping (Reynolds, 2011).

A bar magnet will create a magnetic field, H, with magnetic flux lines converging towards the end of it (Reynolds, 2011). A dipole will always have a positive- and a negative end with flux lines generated between the poles (Reynolds, 2011), as illustrated in Fig 4-1. The Earth's magnetic field can be compared to a big bar magnet situated in the center of the Earth but inclined at 11,5° to the Earth's rotational axis (Reynolds, 2011). The Earth's magnetic field is stronger at the poles (~60 µT) and decreases towards the geomagnetic equator (~30 µT) (McEnroe et al., 2009). Merrill et al. (1996) state that the Earth has experienced numerous polar reversals during its history with irregular intervals. In addition to the Earth's magnetic pole, the Earth also has a geographical pole. The geographic pole is fixed while the geomagnetic pole moves (Reynolds, 2011). The geomagnetic south pole is today close to the geographical north pole (McEnroe et al., 2009), as is the case in Fig 4-1. In 2010 the geomagnetic south pole was located on the eastern side of Ellesmere Island in the Canadian Arctic Archipelago (Reynolds, 2011).
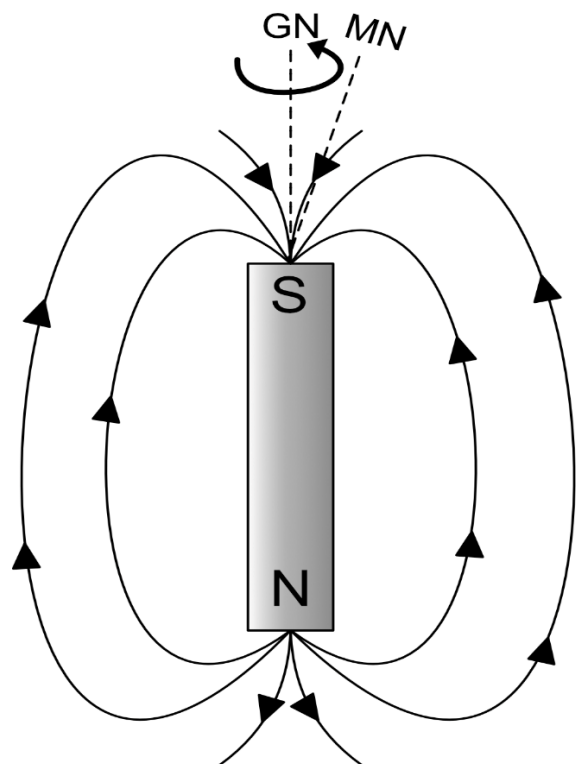
Figure 4-1: Bar magnet with flux lines. GN= Geographical north, MN= Magnetic north. Modified after Reynolds (2011)

In modern times, the intensity of the Earth's main magnetic field has been decreasing by approximately 5% each century (Reynolds, 2011). Fortunately, this slow, relatively gradual change in intensity does not affect data acquisition. However, other secular variations need to be taken into consideration when acquiring data. Jerks are abrupt changes in the trend of temporal variations over short periods (Reynolds, 2011). Researchers are not entirely sure of their physical origin, but they are believed to be due to change in the fluid flow at the surface of the Earth's liquid outer core (Bloxham et al., 2002). Daily changes (diurnal variations) are caused by currents in the ionosphere and can increase the field by 50nT (Reynolds, 2011). They are at a minimum at night when the hemisphere is shaded from the sun, and vary with latitude (Dentith & Mudge, 2014). Base stations record the magnetic field, and their measurements can be used to correct for diurnal effects. On the other hand, rapid and short changes in the magnetic field, such as those due to solar storms, cannot

use the help of base stations as the intensity changes within small distances. In these situations, all magnetic surveying has to stop. Magnetic storms may last for several hours or days and are caused by sunspot and solar activity resulting in solar-charged particles entering the ionosphere (Reynolds, 2011).

As a compass will align and point towards the north, rocks can also align with an applied magnetic field. If they do, the rocks are magnetized. How susceptible material is to being magnetized is called its susceptibility, K, and is dimensionless (Reynolds, 2011). There are two types of magnetization: induced magnetization, J_i, and natural Remanent magnetization (NRM), J_r (Butler, 1992). Induced magnetization occurs when a material is magnetized by an external magnetic field, *H*, and the magnetization is proportional to K (Dunlop & Özdemir, 1997). Natural Remanent magnetization does not require an external magnetic field as it is sustained by an internal field strength due to permanently magnetic minerals (Reynolds, 2011). A rock can carry both types of magnetizations. The induced- and remanent magnetization can have different intensities and be pointing in different directions. The resultant, J, is, therefore, a vector sum of both J_i and J_r (Reynolds, 2011):

$$J = J_i + J_r \qquad (7)$$

Fig 4-2 illustrates how the resultant magnetization's direction and intensity are dependent on the magnetization properties of both the induced and remanent magnetization. They can also cancel each other out if pointing in opposing directions.
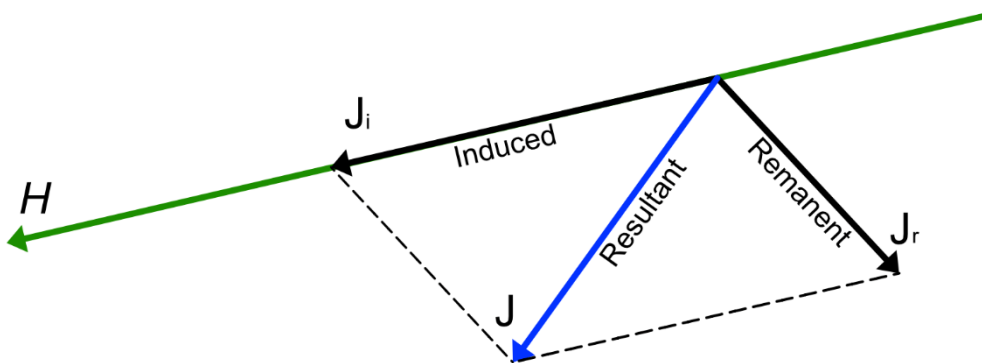
Figure 4-2: Vector summation of induced and remanent magnetization with different magnetized directions and intensities. Modified after (Reynolds, 2011).

Minerals can lose their natural remanent magnetization above certain temperatures, called its Curie temperature (Harrison & Feinberg, 2009). For magnetite, this is a temperature of 580°C (McEnroe et al., 2009). However, during cooling below its Curie temperature, the minerals can once again attain their NRM, which will be aligned to the new present field (Harrison & Feinberg, 2009).
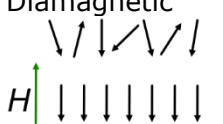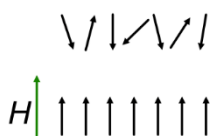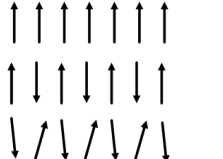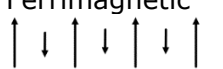
The Königsberger ratio, Q, is the ration between induced and Remanent magnetization (Clark, 1997).

$$Q = \frac{J_r}{J_i} \qquad (8)$$

A Q-value bigger than 1 indicates that the remanence dominates the induced magnetization, whereas a Q-value lower than 1 implies an induced dominated rock (Clark, 1997). It is essential to know the direction of the NRM in rocks that are considered to have a high Q-value (from ~2 and upwards) as this has a substantial effect on the measured resultant values in the field (McEnroe et al., 2009). It is particularly basalts, ores, and skarns that tend to have high Q-values while sediments are predominantly less than 1 (Clark, 1997).

The reason for rocks being magnetic is related to their structure, the atoms (Clark, 1997; Harrison & Feinberg, 2009; Reynolds, 2011). All atoms have a magnetic moment as the quantum effect generates electron spins (Harrison & Feinberg, 2009). Furthermore, the orbital motion of the electrons around the nucleus can give an additional contribution to the magnetic moment (Harrison & Feinberg, 2009). Depending on how the electrons are distributed and how they react to an external field, they can be divided into four groups, as seen in Table 2.

Table 2: Different magnetism in rocks. Based on Clark (1997), Dekkers (1988), Dunlop and Özdemir (1997), Harrison and Feinberg (2009), McEnroe et al. (2009), Potter et al. (2011) and Reynolds (2011).

Type of magnetism	Atom configuration	Magnetic properties	Examples for rocks and minerals
Diamagnetic \\/|/\\/| H |||||||	Complete electron shells. The orbital motions adjust to oppose the applied field.	No net magnetic moment. Weak negative susceptibility	All materials. Calcite, quartz, halite, feldspar, magnesite
Paramagnetic \\/|/\\/| H ↑↑↑↑↑↑↑	Incomplete electrons shells with unpaired electrons that produce unbalanced spins, which are weakly correlated. The magnetic moments align themselves with an applied external field.	No net magnetic moment. Weak positive susceptibility	Olivine (fayalite), pyroxene, garnets, serpentine, ilmenite (above 57 Kelvin),
Ferromagnetic & (Canted) antiferromagnetic ↑↑↑↑↑↑↑ ↑↓↑↓↑↓↑ ↓/↓/↓/↓\\	Unpaired electrons. *Ferro*: The spins are aligned parallel to each other. *Antiferro*: Opposite magnetic sublattices *Canted*: Opposite magnetic sublattices with an angle	*Ferro*: Big net magnetic moment. High susceptibility. *Antiferro:* No net magnetic moment. Weak positive susceptibility *Canted:* Weak net magnetic moment. Weak positive susceptibility.	*Ferro*: Cobalt, nickel, iron *Antiferro*: Goethite, pyrrhotite (hexagonal), *Canted*: Hematite
Ferrimagnetic ↑↓↑↓↑↓↑	One of the two anti-parallel magnetic moments is stronger than the other.	Net magnetic moment. High susceptibility	Magnetite, trevorite, pyrrhotite (monoclinic)

The magnetic moments within a grain will try to obtain the lowest level of energy (Harrison & Feinberg, 2009). When there is no external field applied, the magnetic moments will align themselves to the specific crystallographically defined "easy axis," which is constrained by higher energy demanding "hard axis". The easy axis is energetically favorable, and a magnetized grain will remain fixed along the easy axis as long as the energy barriers (hard axis) are higher than the available thermal energy. This state is called "blocked", and the grain will obtain the same Remanent magnetization until the grain is "unblocked". According to Harrison and Feinberg (2009), this magnetocrystalline anisotropy is one of the most critical concepts in magnetism. In addition to this, both shape and grain size are essential contributors when it comes to magnetism (Clark, 1997; Harrison & Feinberg, 2009).

It is easier to magnetize an elongated body along its length rather than perpendicular to it (Harrison & Feinberg, 2009). This is because the magnetization parallel to the grain creates two poles that are separated by a greater distance compared to a perpendicular magnetization. As a result, it will lower the required opposite demagnetizing field, H_D, and the grain will keep its lowest level of energy (Harrison & Feinberg, 2009). Elongated bodies are, therefore, more accessible to magnetize than spheres. Size is also an important parameter. If the grain is sufficiently big enough, its demagnetization energy level can be lowered or eliminated by subdividing the grain into domains. Each domain is separated by a domain wall that allows the domains to have a uniformly magnetized domain parallel to the surface at all points (Dunlop & Özdemir, 1997). This type of grain is called a multidomain grain (MD), whereas a grain that is too small to accommodate a domain wall (~65 nm) is called a single domain (SD) grain (Harrison & Feinberg, 2009). MD grains are easier to magnetize and have a higher susceptibility than SD grains (Reynolds, 2011). Furthermore, MD grains have a zero or near-zero overall net magnetization in the absence of an external field (Dunlop & Özdemir, 1997), while SD grains can hold highly stable Remanent magnetizations (Harrison & Feinberg, 2009). In addition to SD and MD grains, grains that are smaller than ~20 µm can enter an intermediate domain, which is called the pseudosingle domain (PSD). Small PSD grains are powerful remanence carriers as they have a strong hard axis (Clark, 1997).

All the abovementioned geophysical properties affect the magnetism of minerals. The most important terrestrial magnetic minerals are oxides of iron and titanium. A ternary diagram, consisting of Ti^{4+}, $Fe^{2+,}$ and Fe^{3+}, contains some of the most common magnetic minerals such as, e.g., magnetite, hematite, ilmenite, maghemite and their respective solid solutions as seen in Fig 4-3. According to Dentith and Mudge (2014), increasing titanium content will lower the susceptibility and NRM values of the mineral. The titanomagnetite solid solution, also known as the spinel group, contains many minerals that can be magnetic, such as iron- and chromium-spinel. Pyrrhotite and siderite are other important magnetic rocks, and they are essential in sediments (Dunlop & Özdemir, 1997).
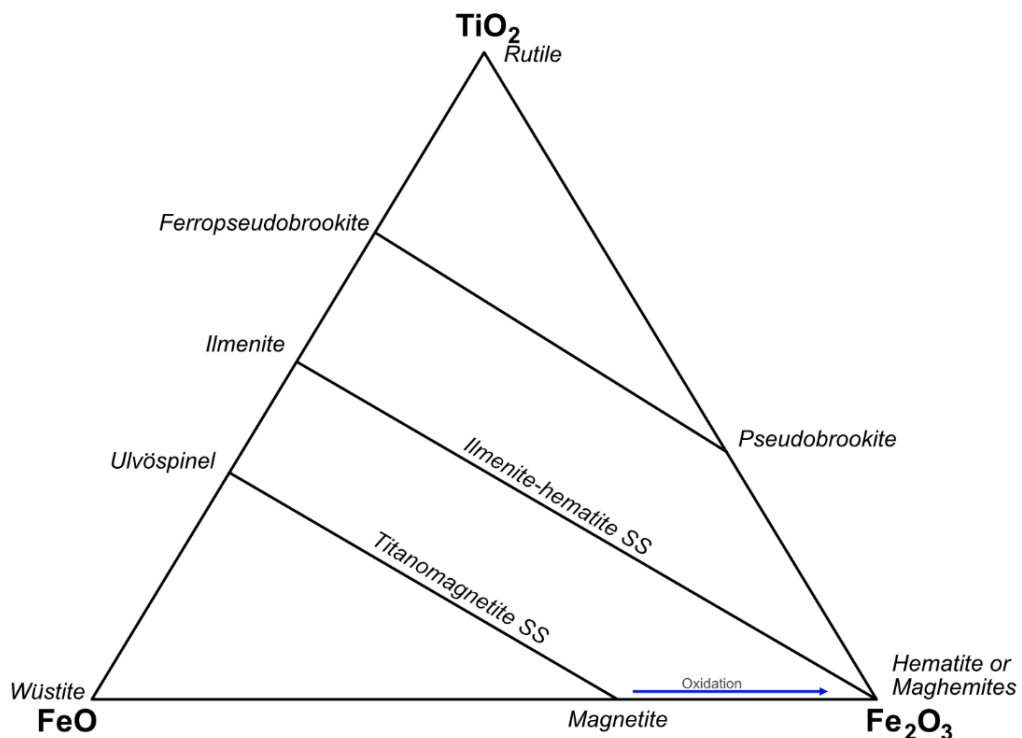
Figure 4-3: The TiO_2-FeO-Fe_2O_3 ternary diagram. SS: Solid solution. Based on Clark (1997), Dunlop and Özdemir (1997), McEnroe et al. (2002), and McEnroe et al. (2009).

20

4.2 Formation of Serpentinite, Mineralogy and Geophysical Expression

Serpentinites are rocks that mostly consist of serpentine group minerals: lizardite, chrysotile, and antigorite (Evans et al., 2013). They are green to black in color, rich in water, and are formed by hydration of olivine-rich ultramafic rocks (Guillot & Hattori, 2013). Furthermore, they play an essential role in numerous geological settings and have been used by many cultures as carving and building stones (Guillot & Hattori, 2013).

The mantle is the ultimate source for magma and is mostly composed of Fe- and Mg-rich silicate minerals such as olivine, pyroxene, and amphibole (Winter, 2014). Rocks consisting of predominantly olivine, orthopyroxene, and clinopyroxene are called ultramafic rocks. They are divided into peridotites and pyroxenites depending on the olivine content (Streckeisen, 1967), as illustrated in Fig 4-4. Serpentinite form by hydration of MgFe-rich peridotites (olivine or pyroxene) by the general equation:

$$\text{MgFe olivine} + H_2O \rightarrow \text{MgFe serpentine} + \text{magnetite} + \text{MgFe brucite} + H_2 \qquad (9)$$
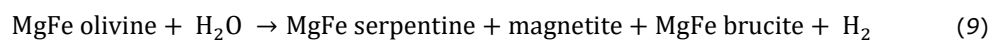
(Evans et al., 2013). Newly formed serpentine cannot always accommodate all the available iron, and the excess is therefore incorporated into magnetite (Winter, 2014). This reaction leads to a volume increase with a potential expansion as significant as 40% (Evans et al., 2013). The serpentine group minerals favor specific pressure and temperature conditions. According to Deer et al. (1992), a typical sequence with an increasing degree of metamorphism is lizardite → lizardite + chrysotile → chrysotile + antigorite → antigorite. When the temperatures exceed 400-450°C, the serpentinites can no longer hold their water, and they get dehydrated (Hirth & Guillot, 2013; Winter, 2014).

Winter (2014) describes how serpentine and its associated minerals react with an increasing degree of metamorphism. A typically low-grade greenschist facies peridotite will contain serpentine, brucite, diopside, and magnetite. With increasing temperature, the metamorphic reactions are as follows:

Lizardite and chrysotile occur in low-grade serpentinites and gradually transform into antigorite with increasing temperatures. At ~400°C, brucite is consumed by a reaction with antigorite, and secondary olivine is formed. In addition to this, water is also formed as the serpentinites no longer can hold their water:

$$20\,\text{Brucite} + \text{Antigorite} \rightarrow 34\,\text{Forsterite} + 51\,H_2O \qquad (10)$$
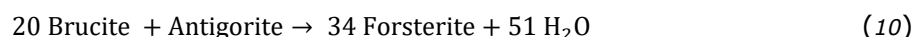
The secondary olivine tends to be more Mg-rich than the original peridotic olivine as most of the iron is consumed by the magnetite earlier in the process. The remaining minerals are now antigorite, diopside, and forsterite. Further, antigorite reacts with diopside and forms tremolite at ~530°.

$$8\,\text{Diopside} + \text{Antigorite} \rightarrow 18\,\text{Forsterite} + 4\,\text{Tremolite} + 27\,H_2O \qquad (11)$$
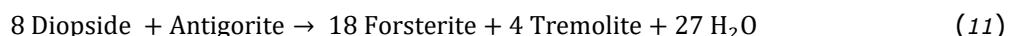
Finally, the stability limit of antigorite is reached at ~570°C, and as a result, talc forms:

$$\text{Antigorite} \rightarrow 18\,\text{Forsterite} + 4\,\text{Talc} + 27\,H_2O \qquad (12)$$
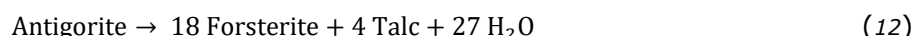
With increasing temperatures, other minerals continue to form. Chlorite is also a common mineral in metamorphosed ultramafic rocks, and it can be stable up to 700-750°C. The whole process is shown in Fig 4-5.
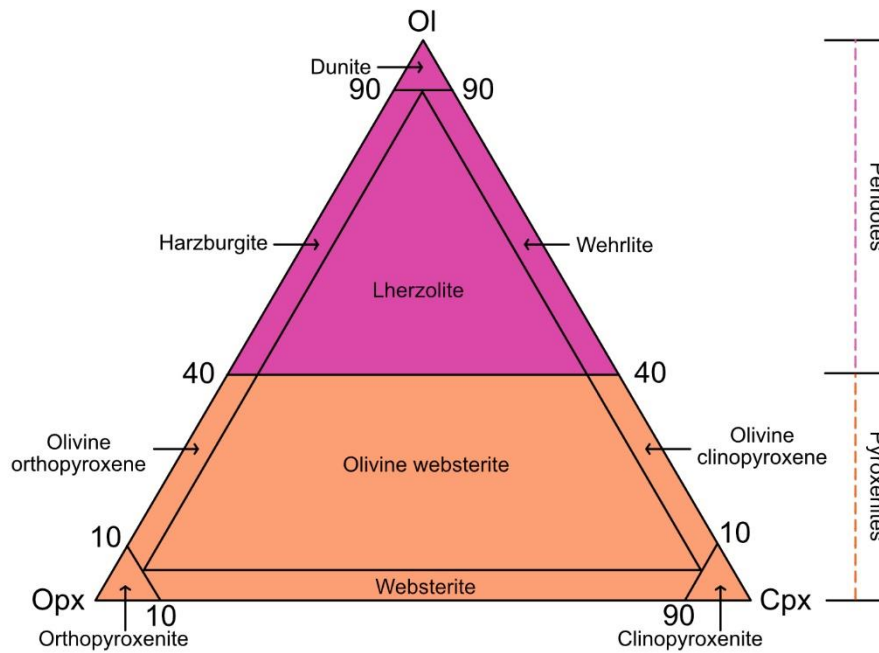
Figure 4-4: Classification diagram of ultramafic rocks. Modified after (Streckeisen, 1967).
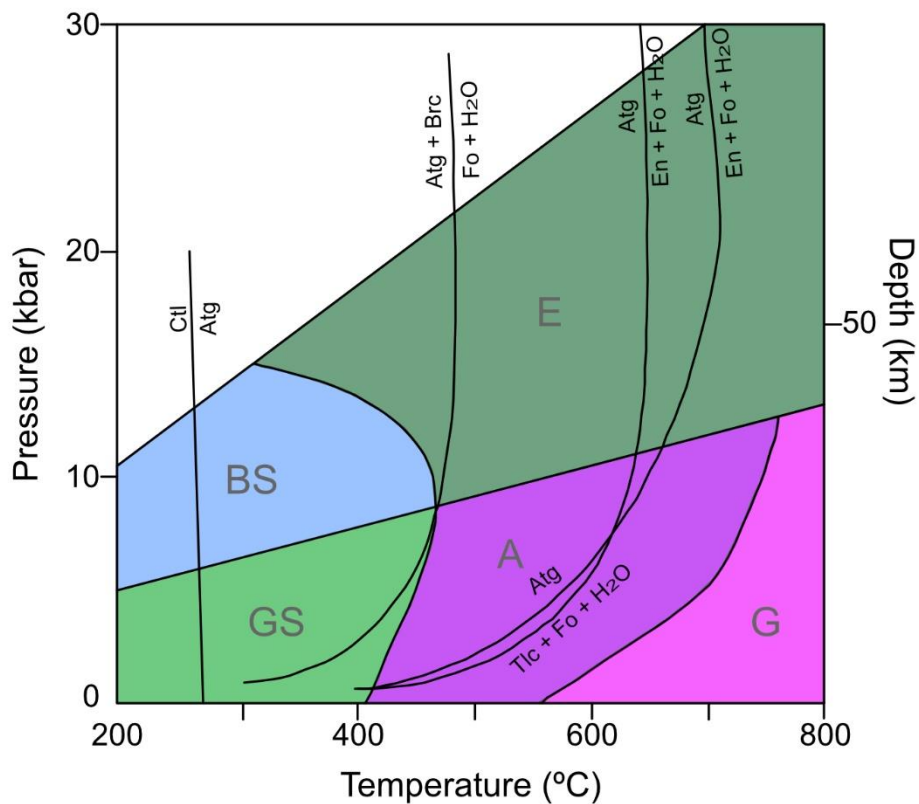
Figure 4-5: Possible phase diagram for serpentinite minerals on top of a corresponding metamorphic facies diagram. Ctl = Chrysotile, Atg = Antigorite, Brc = Brucite, Fo = Forsterite, En = Enstatite, Tlc = Talc, H_2O = Water, BS = Blueschist, GS = Greenschist, A = Amphibole, G = Granulite, E = Eclogite. Modified after Auzende et al. (2006).

According to Winter (2014), adding CO_2 to the system will decrease the stability of hydrous minerals such as serpentine and brucite. A small amount of CO_2 will lower the stability field of antigorite and produce talc and magnesite at the expense of it. The presence of carbonate veins in a serpentinite body suggests that the whole rock is not in equilibrium or that the rock is internally buffered. Furthermore, metasomatism is common at the margins of bodies where fluids may percolate easily along fractures or faults.

Multiple tectonic settings allow serpentinite minerals to form. Some of the most common tectonic settings are subduction zones, spreading ridges, oceanic core complexes (OCC), hyperextended margins, and faults. They are briefly described here.

The oceanic crust is rich in water; the crust contains structurally bound water, and the overlying sediments hold water in their pore space (Winter, 2014). In a subduction zone, the subducting slab will get dehydrated with increasing depths as the pressure and temperature increase. For a metabasalt, dehydration starts at around 40 to 50km, and then transforms into eclogite (Blakely et al., 2005). The released water will migrate upwards and hydrate the overlying mantle wedge, which then gets serpentinized (Guillot et al., 2015). The addition of volatiles into the hot overlying mantle lowers the melting point and causes partial melting, which creates volcanic arcs (Guillot et al., 2015). Fig 4-6 illustrates serpentinization in a subduction zone.
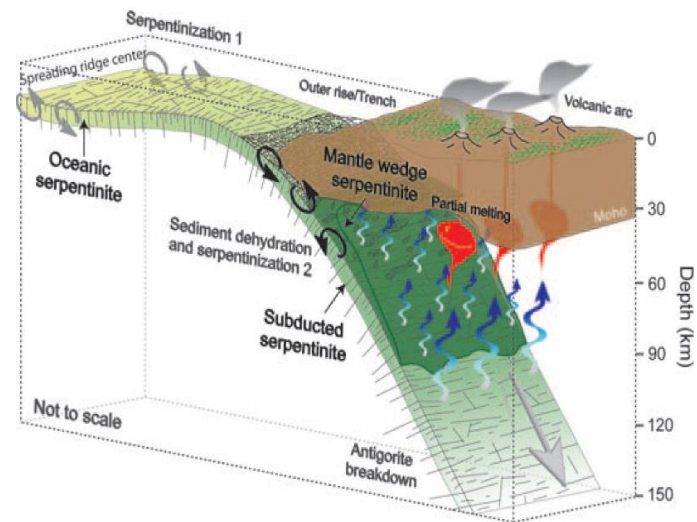
Figure 4-6: Serpentnization in a subduction zone. Figure from Guillot & Hattori (2013).

Slow- to ultraslow-spreading ridges (<40mm/year) (Guillot et al., 2015), such as the Mid-Atlantic Ridge (Evans et al., 2013), also produce serpentinites. Due to isostatic equilibrium, the mantle peridotites rise towards the surface as the crust is being pulled apart (Allen & Allen, 2005). The exposed mantle peridotites become pene-

Figure 4-7: A 3D illustration of an ocean core complex (OCC). Serp: serpentinization. Figure from (Guillot et al., 2015)

trated by seawater, and serpentinites may form down to a depth of ~7km (Evans et al., 2013). The volcanic activity is discontinuous in space and intermittent through time (Guillot et al., 2015). Furthermore, spreading ridges are more broken up, and water can penetrate through multiple faults (Winter, 2014). Ocean core complex (OCC), a $10x20km^2$ (Guillot et al., 2015) dome-like structure, may form close to the ridge axis (Hirth & Guillot, 2013) as a result of unroofing along low-angle kilometer-scale detachment faults (Guillot et al., 2015). These can rise to 500m above the seafloor and show corrugated surfaces due to detachment faults (Hirth & Guillot, 2013), as seen in Fig 4-7. Guillot and Hattori (2013) suggest that up to 25% of the top part of the oceanic lithosphere may consist of serpentinites.

Serpentinites may also form in an oceanic to continent transition (OCT). The OCT is a ~200km wide transition zone that contains a hyperextended (≤10km) continental crust with an exhumed mantle situated in a normal thick (~30km) continental crust, as illustrated in Fig 4-8. As in spreading ridges, water penetrates the exhumed mantle and serpentinizes them down to a depth of ~6km. The upper serpentinized mantle show characteristics between an oceanic and a continental mantle with less than 10% partial melting (Guillot et al., 2015), and lack the typical ophiolitic sequence with sheeted-dike complexes (Andersen et al., 2012).
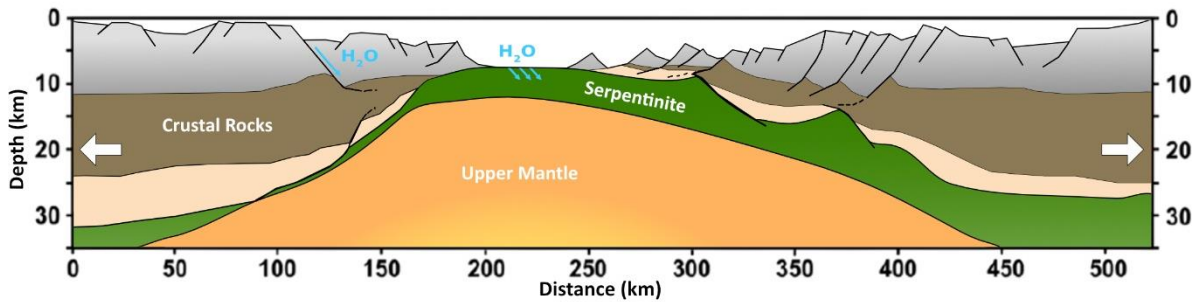
Figure 4-8: Oceanic to continent transition (OCT). Modified after Guillot et al. (2015).

Large-scale deep-seated strike-slip faults also accommodate serpentinites (Guillot et al., 2015). The San Andreas Fault is a large-scale strike-slip fault with numerous serpentinite bodies (Hirth & Guillot, 2013). There are multiple theories of how they formed. Coleman (1971) interpreted them to be ophiolites along old suture zones, which got reactivated and parallelized along the fault zone while Guillot et al. (2015) sees them as deeply connected diapirs exhumed along the fault zone. Further-

Figure 4-9: A 3D illustration showing the distribution of serpentinite outcrops along the San Andreas Fault. Figure from Guillot et al. (2015).

more, Saumur et al. (2010) proposed that these serpentinites were protruded from a mantle wedge to the surface along the fault zone, as seen in Fig 4-9. Nevertheless, they all have in common that the serpentinites travel through the fault zone rather than forming in the fault zone.
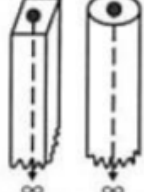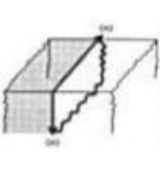
As serpentinization of an ultramafic rock leads to a volume increase and the formation of magnetite as seen in equation 9, serpentinized rocks have a characteristic geophysical signal. Serpentinites are associated with decreasing density and increasing susceptibility and NRM (Dentith & Mudge, 2014). The density is inversely proportional to the degree of serpentinization, while the susceptibility has a nearly exponential correlation (Fichler et al., 2011). When acquiring aeromagnetic data over an area, serpentinites often occur as a positive anomaly compared to the surrounding low magnetic rocks. The size of the magnetic anomaly is dependent on both the depth and shape of the serpentinite according to equation 13:

$$\text{The decay of magnetic anomaly size} = \frac{1}{\text{depth}^N} \qquad (13)$$

where N = structural index, as seen in Table 3. Deeper spherical bodies will have lower amplitudes with longer wavelengths compared to shallower elongated bodies. When combined with gravimetric measurement, serpentinites can be distinguished from their surrounding rocks by having a positive magnetic anomaly without a corresponding positive gravity anomaly.

Table 3: Structural index for different models for equation 13. Modified after Hinze et al. (2013).

EULER Structural index N for simple sources						
Magnetic model	Sphere	Vertical cylinder	Horizontal cylinder	Vertical sheet	Horizontal sheet	Contact
Magnetic field	3	2	2	1	1	0

To enhance the targeted rocks in the subsurface, gradient- or derivative filters may be applied to the measured TMI. A high-pass filter enhances short wavelengths, while a low-pass filter enhances long wavelengths (Dentith & Mudge, 2014). Vertical- and horizontal gradients are very sensitive to the edges of bodies and are good filters for finding the extent of the body (Dentith & Mudge, 2014). The total horizontal gradient, a combination of the horizontal gradients, is an excellent filter for detecting the boundary of a body:

$$\text{Total horizontal gradient} = \sqrt{\left(\frac{\partial M}{\partial x}\right)^2 + \left(\frac{\partial M}{\partial y}\right)^2} \qquad (14)$$

where M is the magnetic field, and x and y are the horizontal directions (Dentith & Mudge, 2014). A tilt derivative is a useful filter for detecting vertical magnetic features such as, e.g., faults:

$$\text{Tilt derivative} = \tan^{-1}\left[\frac{\partial M}{\partial z} \Big/ \sqrt{\left(\frac{\partial M}{\partial x}\right)^2 + \left(\frac{\partial M}{\partial y}\right)^2}\right] \qquad (15)$$

where z is the vertical direction. The tilt derivative will have a positive anomaly over the magnetic source and a negative anomaly outside it (Dentith & Mudge, 2014).

5 Results

Slipsteinsberget serpentinite quarry is located in the southern part of Slipsteinsberget hill and is approximately 110m wide in an east-west direction. The quarry consists of 4 east-west striking benches with different lengths and heights, as illustrated in Fig 5-1. Traces of underground mining are observed in several places around the hill, but it is no longer possible to enter the mines as they are filled with water.

Due to the well-exposed rocks within the quarry, most of the comprehensive field mapping was conducted on the quarry benches. The rest of Slipsteinsberget and its immediate enclosing rocks are mostly covered by vegetation with limited outcrops. As a result, the mapping outside the quarry was very much dependent on the ground magnetic survey and correlations with the well-exposed rocks within the quarry. However, the confining steep terrain at the outermost edges of Slipsteinsberget showed some excellent outcrops which helped in the determination of contacts. The following sections will present the results from the field observations, field measurements, and laboratory analyses.

Figure 5-1: LiDAR data of Slipsteinsberget taken from høydedata. Point 1 and 2 show locations of old mine entrances. The schematic illustration to the right identifies the different benches (not to scale)
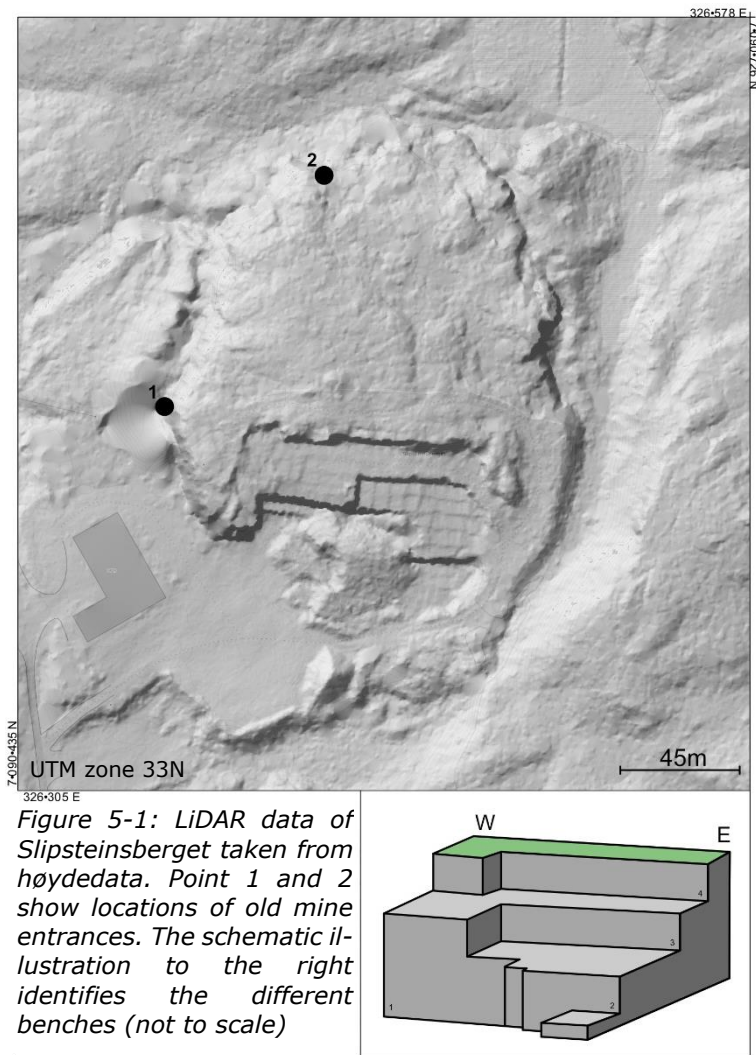
5.1 Geological Map

The geometry of Slipsteinsberget is challenging to visualize structurally due to the lack of tectonic indicators such as foliation planes, folds, and other structures. However, the surrounding garnet mica-schist is consistently foliated with a general dip/dip-direction of 33/236. Also, Slipsteinsberget contains east-west-striking sub-vertical fractures, and conjugate fracture sets striking north-south. Some of the exposed fracture planes show mineral lineations (slickenlines), although the displacement direction could not be determined.

The primary rock within the quarry is serpentinite. The serpentinite shows some internal variations and gradually grades to soapstone in Slipsteinsberget's outermost edges.

Slipsteinsberget has an overall elliptical shape, and a positive topographic relief that comprises "out-of-place" lithologies compared to the general trend of garnet mica-schist in the area. From the center, the lithologies show an almost elliptical zonation. Based on field mapping, as well as petrographical descriptions (see section 5.2), an interpreted geological map and a profile are presented in Fig 5-2.
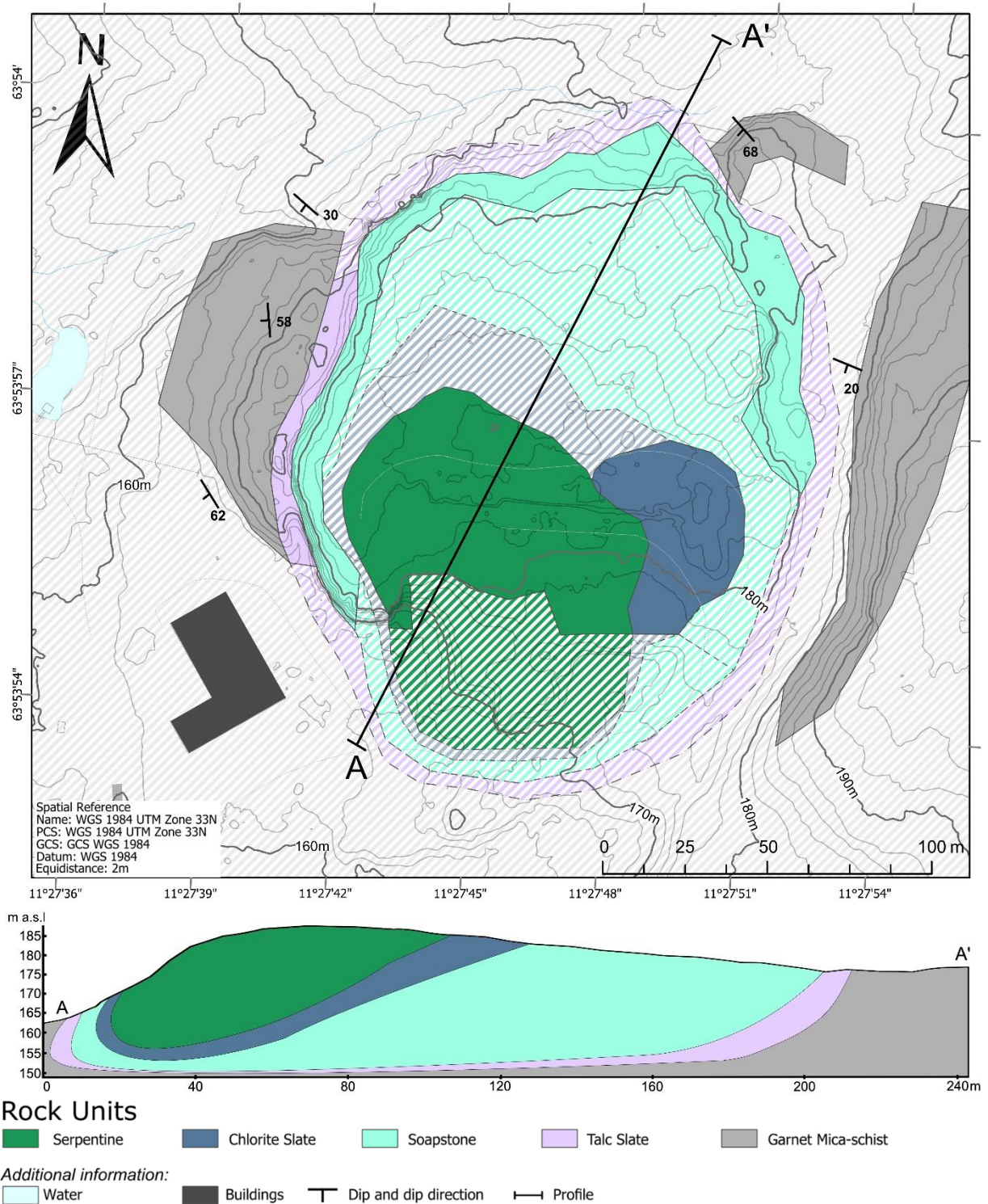
Figure 5-2: Geological map and profile of Slipsteinsberget based on field mapping. The dashed lines in the map represent uncertain interpretation due to the lack of outcrops.

5.2 Petrographical Descriptions and Field Measurements

The rocks within the field area show a clear division in rock type depending on their location. The rocks within Slipsteinsberget are metamorphic ultramafic rocks, while the country rock is metasedimentary. The metamorphic ultramafic rocks show a distinct zonation that can be divided into four zones based on their appearance in the field, their magnetic properties and mineralogical assemblages obtained from both drill cores, optical microscopy, SEM, and XRD (see Appendix for more details). Mineral identification was achieved by a combination of chemical analysis (point analysis) obtained by SEM (and correlated to the literature for typical mineral chemistry and occurrences), and microscopy. The contact between the metamorphic ultramafic rocks and the surrounding metasedimentary rock was not easy to observe as much of it is highly weathered. No signs of contact metamorphism were observed.

This chapter will describe the major rock units and their measured susceptibility in the field. A summary of the mineral distribution and their magnetic response is illustrated in Fig 5-13. This is a panorama profile taken from bench four, which is the most extensive bench. This bench exposes almost all of the different mineralogical zones.

5.2.1 Serpentinite

Serpentinite is the primary lithology of the quarry. It is massive, green to black, and contains white-brown magnesite veins that chaotically crosscut the entire quarry. The serpentinite dominates in the core of Slipsteinsberget and shows a lithological variation that can be subdivided into three groups, as seen in Fig 5-14, and is further described below

5.2.1.1 Green Serpentinite

The green serpentinite is the most prevalent of thee three serpentinite subgroups, and consists of predominantly antigorite and magnesite. It is aphanitic and appears massive in the field, although a weak foliation is observed under the microscope. It varies in color from light- to dark-green and often contains cm-scale black areas. The intensity of the black regions depends on the texture of the serpentinite. A blade-like texture results in a lighter serpentinite, while a needle-like texture results in a darker one, as seen in Fig 5-3. The green serpentinite is crosscut by leucocratic magnesite veins mostly parallel to its weak foliation.

The green serpentinite had a consistent low-magnetic response in the field with susceptibility values below 0,001 SI.

Figure 5-3: Photomicrograph of sample 4 - Thin section of antigorite and magnesite in cross-polarized light (xpl). Lower left corner shows bladed antigorite, while the middle and upper left show needle-like antigorite. Atg: Antigorite. Mgs: Magnesite.

5.2.1.2 Brecciated Serpentinite

The brecciated serpentinite occurs in the center of bench four and comprises approximately 30m of the wall. This subgroup consists of a massive groundmass with bigger clasts (up to 1,5m), mostly made up of serpentinite,

magnesite, and magnetite. The groundmass consists of aphanitic antigorite and two groups of magnetite with distinct grain sizes: microcrystals up to 20 µm and grains ~2mm. The phaneritic magnetite grains are zoned and are characteristic of the rock unit. This is further discussed in section 5.4. The big clasts have a melanocratic rim and a leucocratic core. The core has a mesh texture made up of magnesite, as seen in Fig 5-14. The clasts are inequigranular, show no shape preferred orientation, and are randomly distributed throughout the whole zone. The crosscutting magnesite veins penetrate the groundmass but do not penetrate the clasts. This zone also

Figure 5-4: Photomicrograph of sample 3 - Zoned magnetite grain is seen in reflected light. See section 5.4 for further information on the zonation.

contains a discontinuous magnetite vein (up to 2cm wide). The eastern edge of the zones is hidden behind a ~1cm thick magnesite layer covering the whole bench face. It was not possible to observe the serpentinite behind it on a large scale. However, a sample revealed the same mineralogy as the rest of the zone with zoned magnetite grains up to 2mm, as seen in Fig 5-4.

Susceptibility measurements conducted on-site revealed two distinct groupings within the brecciated serpentinite. They both carried values higher than the green serpentinite, which resulted in a positive anomaly. The clasts differentiated from the groundmass by having a higher susceptibility with values ranging from approximately 0,06-0,10 SI. The groundmass and the hidden zone to the east had values between 0,01-0,05 SI. In addition to this, the magnetite vein had an SI-value of 0,7. Thus, the brecciated serpentinite showed a good susceptibility correlation with lithology.

5.2.1.3 Dark Green Serpentinite

The dark green serpentinite is located on the western side of bench three. It is melanocratic, aphanitic, and appears homogenous in hand specimens, as Fig 5-14 illustrates. However, this serpentinite differentiates from the other two serpentinites by containing olivine. The olivine makes up approximately 35% of the rock, with individual crystals reaching sizes up to 1mm, and is rich in magnesium. As Fig 5-5 shows, the forsterite grains accumulate together in big groups surrounded by antigorite. Furthermore, the dark green serpentinite holds magnetite grains. The magnetite grains appear as bigger clasts (up to 1,55mm), but also in small microcrystals (up to 20 µm), as seen in Fig 5-6. The microcrystals accumulate both between the grains and within the connection to fracture zones. Moreover, the magnetite grains do not show a significant zonation pattern as in the brecciated serpentinite (but it does occur) and do not contain as many big grains.

Susceptibility measurements conducted on the dark green serpentinite in the field showed a clear division in SI values. They clustered in 2 groups of approximately 0,04 and 0,09 SI. Due to the homogeneity of the rock, there were no signs of any lithological relationship.
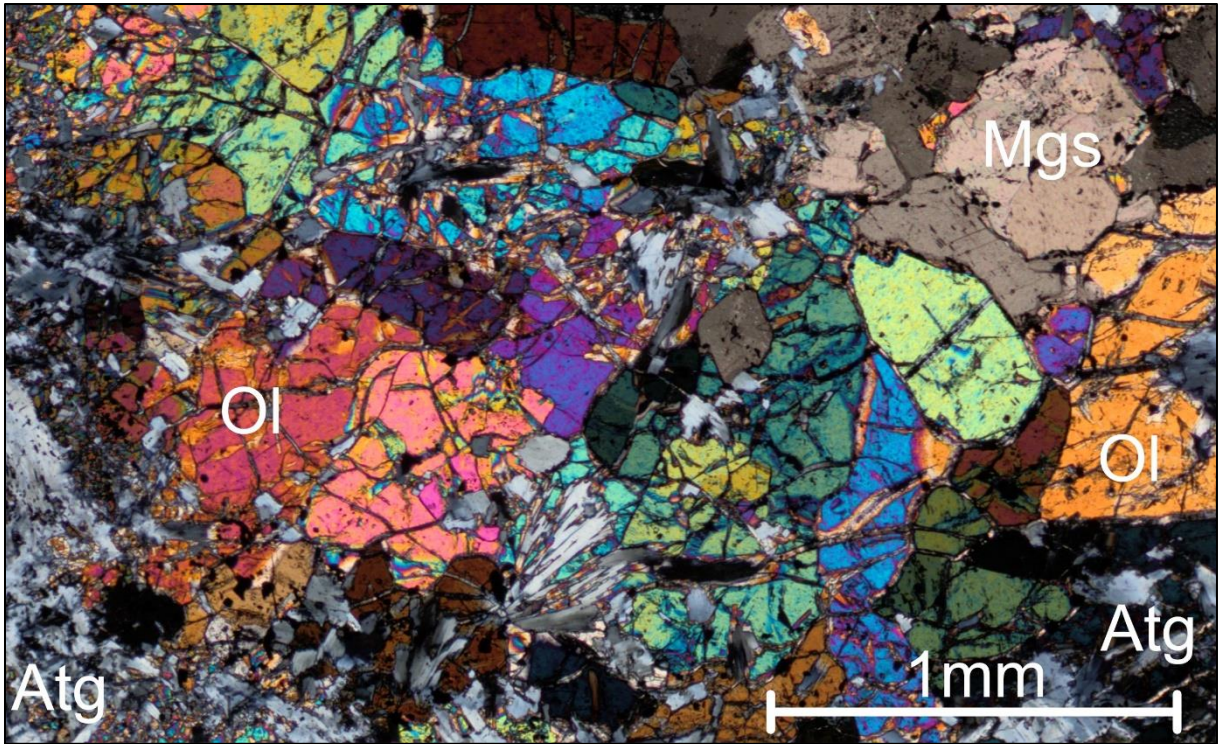
Figure 5-5: Photomicrograph of sample 8 - Xpl of dark green serpentinite with olivine grains accumulated in groups with antigorite around it. The olivines have undulose extinction and subgrain boundaries, with interlobate boundaries. Ol= Olivine, Atg= Antigorite, Mgs= Magnesite.
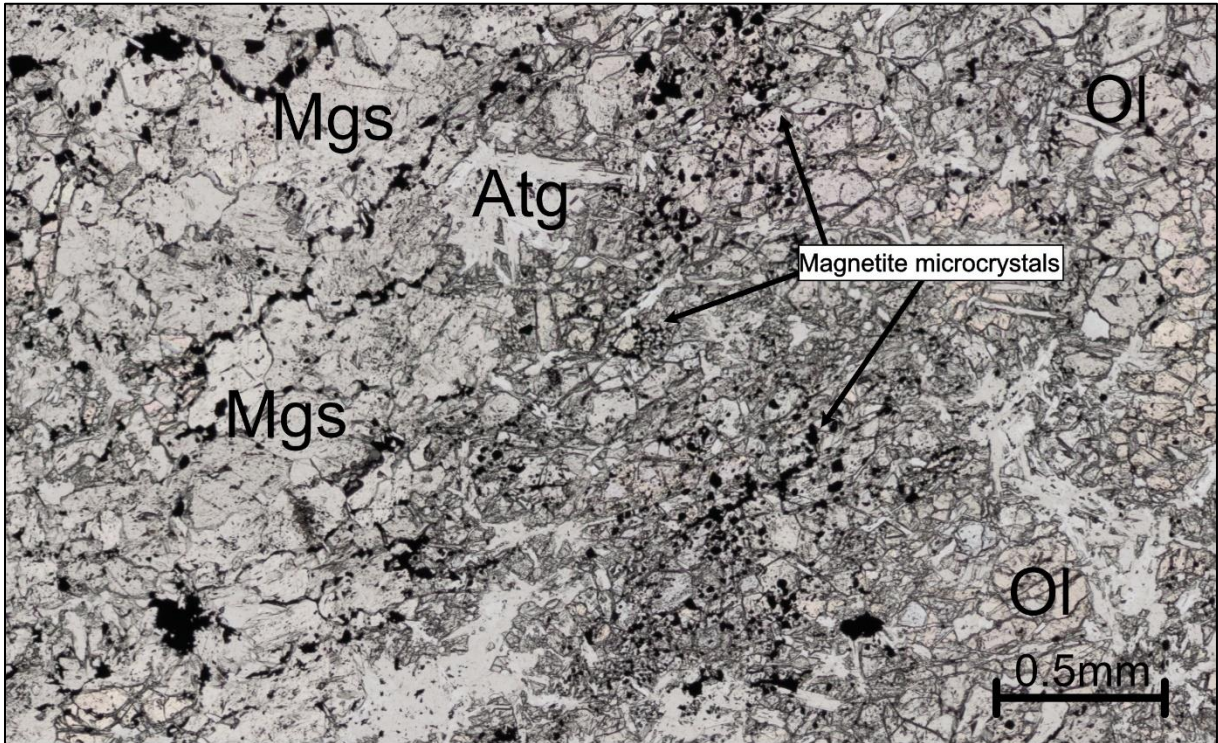
Figure 5-6: Photomicrograph of sample 8 – Dark green serpentinite with magnetite microcrystals in plane-polarized light (Ppl). They occur both within and between grains. Ol = Olivine, Atg= Antigorite, Mgs=Magnesite.

5.2.2 Chlorite Slate

The chlorite slate is located on the eastern side of the quarry. It is melanocratic, aphanitic, schistose, and mainly consists of chlorite. Moreover, it shows a wide variety of minor phases. Rhombohedron crystals of magnesite up to 1cm in size are easily detected. Most of these crystals weathered on the surface of the chlorite slate, leaving rhombohedron holes in the slate. The magnesite is still intact on fresh surfaces. Close to the contact between the serpentinite and the chlorite slate, white, radial, Ca-rich (possibly tremolite) amphibole coexist with the slate. As seen in Fig 5-7, they are acicular and reach sizes up to 4 cm. The area with amphiboles lacks the presence of magnesite. Furthermore, the chlorite slate contains numerous monazite and ilmenite grains (~50 μm – 200μm in size). Bigger grains of hydroxylapatite (see XRD results in Appendix E and Mortenson (1973)) and ilmenite (up to 3mm in size) are situated in veins through the chlorite slate together with pyroxene.

Figure 5-7: Chlorite slate with a zone of white, radial, acicular amphibole. Compass for scale.

Susceptibility measurements conducted on-site indicated a low to nonmagnetic rock with SI values of ~0,002. The variation of minor phases did not affect the readings.

5.2.3 Soapstone

The soapstone is abundant in the outermost edges of Slipsteinsberget and can be traced all around it. Because a lot of the sites with exposed soapstone showed evidence of pre-historic times, the soapstone has been very much left untouched for this thesis. The surface of the soapstone is heavily weathered and appeared as a massive unit. However, one sample taken outside the restricted area allowed further investigation on a fresh surface. It is a leucocratic, equigranular, fine-grained rock mostly consisting of magnesite and talc. A weak foliation exists, and the talc minerals have developed perfect cleavage. In addition, the soapstone contains some minor dark minerals that make up less than 1% of the rock. Fig 5-8 shows how these minerals appear in SEM. They are profoundly altered and consist of pyrrhotite, trevorite, and mackinawite (see SEM Appendix D for details).
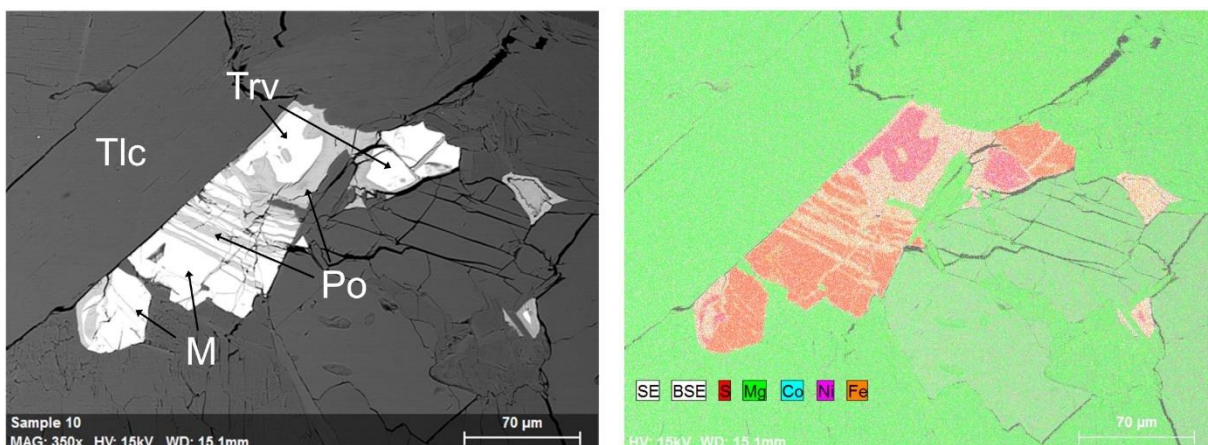
Figure 5-8: Sem image of sample 10 – mapping-image of altered grain consisting of talc (Tlc), pyrrhotite (Po), trevorite (Trv), and mackinawite (M).

Susceptibility measurements conducted on-site indicated a low to nonmagnetic rock with an SI value of 0,001.

31

5.2.4 Talc Slate

The talc-rich zone is exposed on the western side of Slipsteinsberget. It situates in an elongated depression between soapstone and garnet mica-schist with steep walls enclosing it on both sides, as seen in Fig 5-9. It is heavily weathered and was hard to distinguish from regular soil. Due to its heavily weathered condition, it was not possible to obtain any useable samples from this location. However, drill cores stored at Løkken exposed fresh talc surfaces, which made a closer investigation possible. The talc is leucocratic, aphanitic, and has a flakey texture. It also contains small (up to 1mm) dark minerals. These were too small for the portable XRF to measure and remain unidentified. The talc also includes some small zones (3 cm) of epidote.

Susceptibility measurements revealed a low to nonmagnetic rock with SI values of 0,001-0,002.

Figure 5-9: Depression with talc between soapstone to the left and garnet mica-schist to the right. Person for scale.

5.2.5 Garnet Mica-schist

The garnet mica-schist is the country-rock, which crops out in numerous places outside Slipsteinsberget. It is a leucocratic foliated rock with a porfyroblastic texture consisting of quartz, mica, and garnets. The quartz and mica occur mostly separately in bands stacked on top of each other. However, some small mica grains occur within the quartz-rich zones with a lepidoblastic texture. The garnets are porphyroblasts in the quartz-rich zones. They are red, easily spotted, and vary in size from 1mm up to almost 1cm. They are rich in iron and aluminum and classify as almandine garnets. The mica-garnet schist has a general foliation with a dip and dip-direction of 33/236, as seen in Fig 5-11

Figure 5-10: Photomicrograph of sample 11 – Garnet porphyroblast with poikilitic texture and pressure shadows in ppl. Red stippled lines: pressure shadows. Chl = chlorite, Qtz = quartz, Ms = muscovite, Grt = garnet.

Furthermore, the garnets show poikilitic texture and pressure shadows on a microscale and are surrounded by muscovite and chlorite, as seen in Fig 5-10. Folds were observed in microscopy, but no large-scale faulting was observed in the field. However, C'-type shear bands were detected on a macroscale (cm), indicating dextral shear sense towards the southeast, as seen in Fig 5-12.

The measurements conducted on-site showed low, consistent SI values of ~0,002. However, the garnet mica-schist in the drill cores revealed some high values over smaller intervals (up to 30cm) with SI values of ~0,005.

Figure 5-11: Stereonet with plotted foliation of garnet mica-schist in brown lines. Black line indicates average dip and dip direction of 33/236

NW   SE
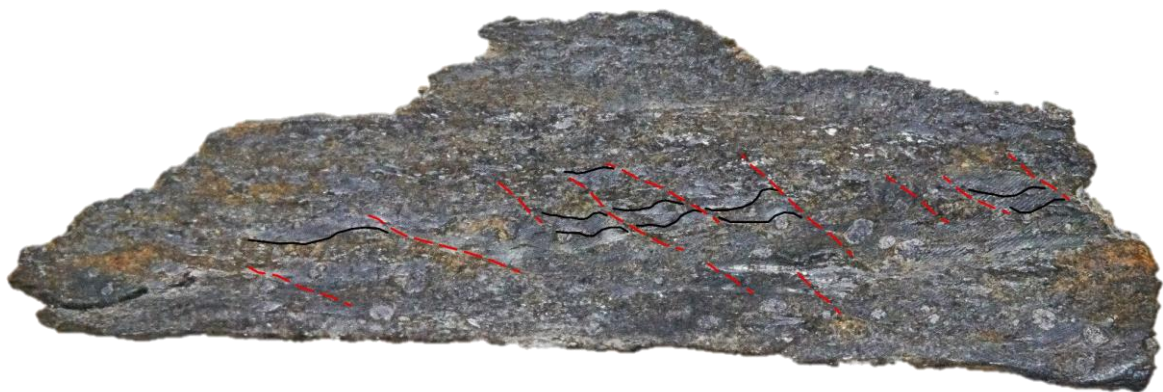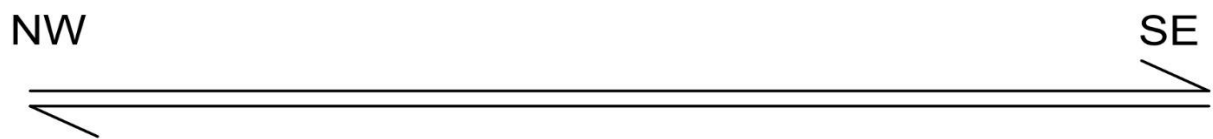
Figure 5-12: Garnet mica-schist C'-type shear bands. Red stippled line: shear band, dark solid line: foliation. Shear bands indicate top to the southeast. The sample is approximately 11cm wide.
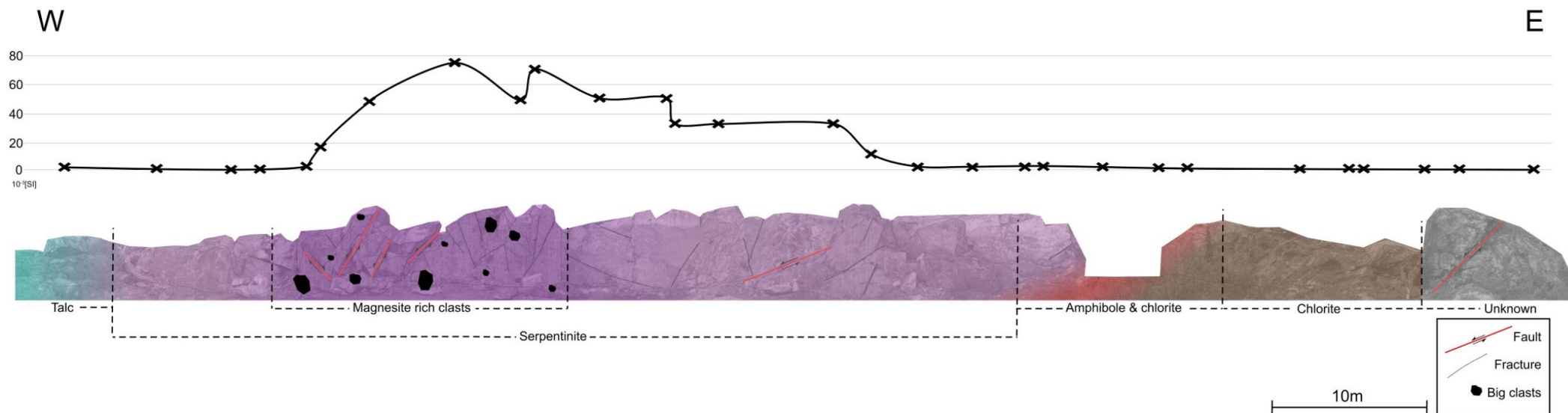
Figure 5-13: Profile of bench wall 4 showing the susceptibility values and a photograph with mineral zonation as an overlaid color pattern.
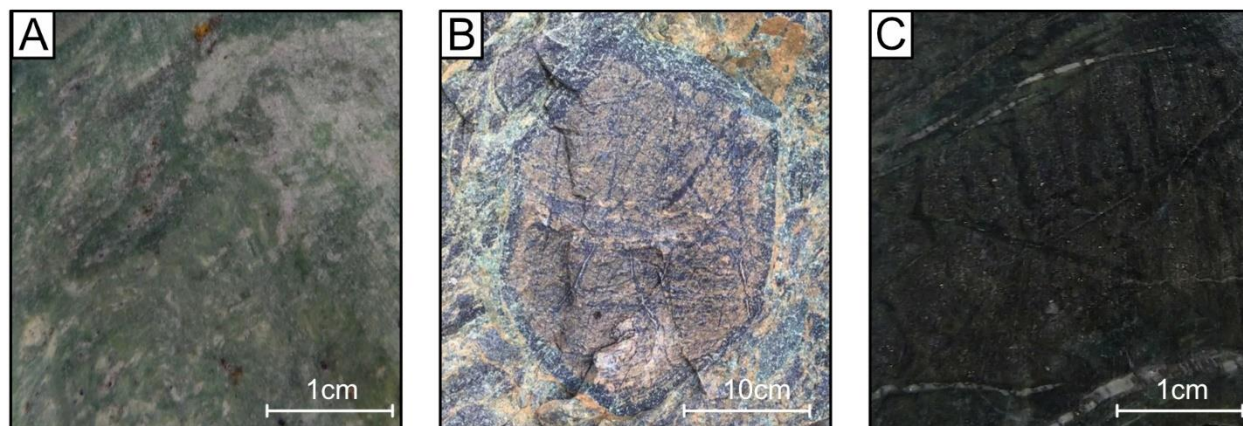
*Figure 5-14: Hand specimens of the three different groups of serpentinites in the quarry. **A**: Cut surface of green serpentinite. **B**: Wall with brecciated serpentinite **C**: The cut surface of dark green serpentinite.*

5.3 Geophysical Analysis

Oriented cylinders taken from the field were tested in the laboratory at NTNU to investigate their geophysical properties. It was not possible to obtain oriented cylinders from all the sample locations for various reasons. However, every lithology is represented by at least one sample giving a minimum of three cylinders. The areas of archaeological importance were restricted and excluded for sampling and hammering. Fig 5-15 shows the field area with sample locations and restricted areas, while Table 4 shows the samples' lithology. The magnetic properties and densities of Slipsteinsberget show significant variations between lithologies and within lithologies. This section aims to present the most relevant results. A detailed spreadsheet with all the results is added to the Appendix at the end.

Table 4: Sample numbers with assigned lithology

Sample number	Lithology
1	Talc slate
2, 9, 3	Brecciated serpentinite
4, 13	Green serpentinite
5, 7, 6, 12	Chlorite slate
8	Dark green serpentinite
10	Soapstone
11	Garnet mica-schist
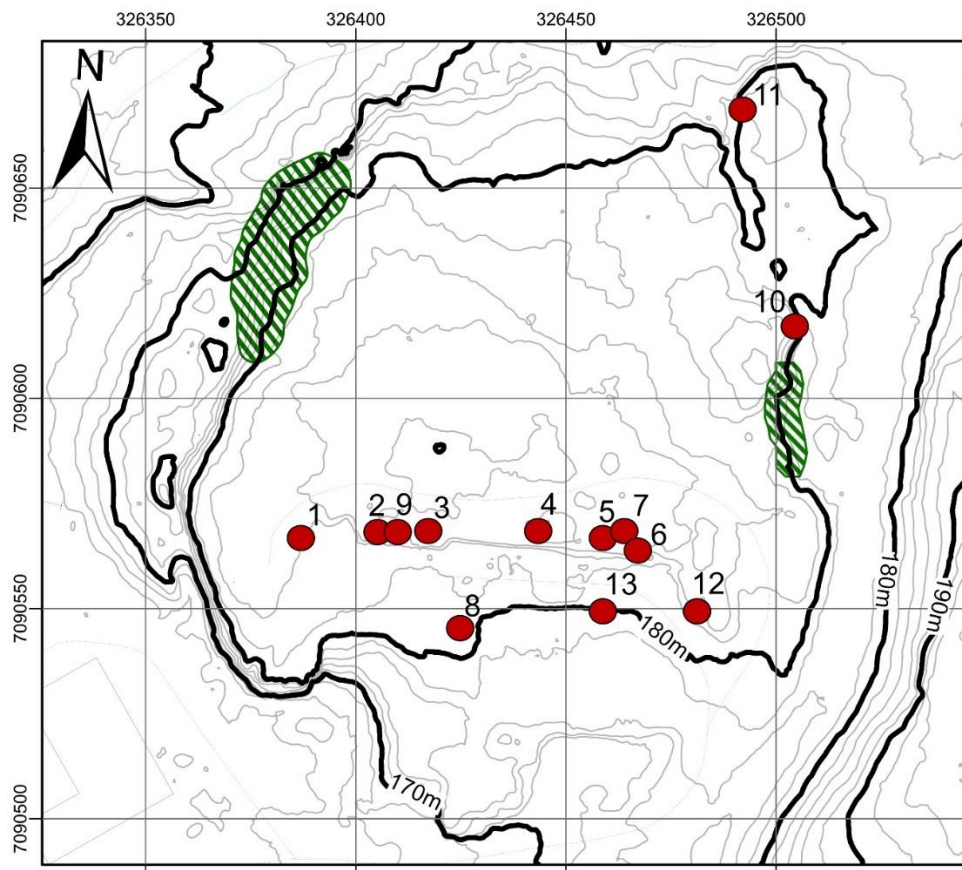
Figure 5-15: Field area with sample localities in red and restricted historical areas in patterned green. Coordinate system: UTM33N/WGS1984. Equidistance = 2m.

5.3.1 Density and Susceptibility

The density of the cylinders was obtained based on equation 3. When plotted against the measured susceptibility from the lab, as in Fig 5-16, the cylinders reveal some interesting observations. The samples have density values ranging from approximately 2,55-2,95 g/cm^3. The chlorite slate, soapstone, talc, and garnet mica-schist have more restricted density ranges, whereas the serpentinite has a more significant variation. When seen together with the susceptibility values, the serpentinites divides into two groups; one group with a lower susceptibility (SI values of ~0,001 – 0,002) and density (2,6-2,7 g/cm^3), and one group with a higher susceptibility (SI values of ~0,04 – 0,3) and a wider density range (2,6- 2,9 g/cm^3). The other lithologies have a more consistent susceptibility and mostly plot within one confined group. Furthermore, the most magnetic serpentinites showed a higher susceptibility in the lab compared to the values obtained in the field. Samples 3, 8, and 9 plot in the higher susceptibility group and show a positive trend with an increasing density (the uppermost trendline in Fig 5-16). There is also a positive trend for the other low susceptibility samples (the lowermost trendline in Fig 5-16). In general, the serpentinites have a higher susceptibility than the other lithologies.
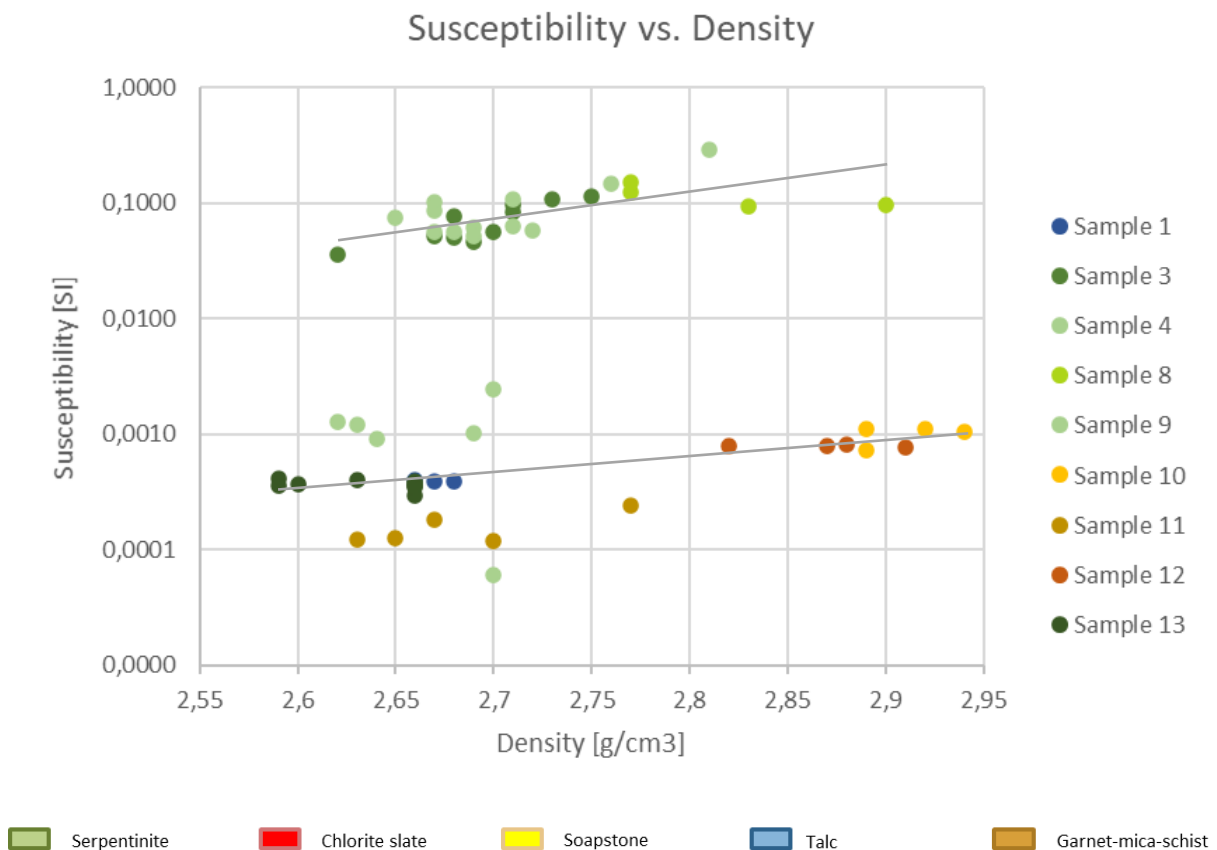
Figure 5-16: Susceptibility versus density plot obtained from cylinders. The grey linear lines are trendlines for the two groupings. The susceptibility axis has a logarithmic scale. Sample localities are found in Fig 5-15.

Some of the cylinders indicated a preferred magnetic orientation, as seen in Fig 5-17. The samples with the highest susceptibilities are also the samples with the highest anisotropy of magnetic susceptibility (AMS). Sample 9 has the highest AMS values, and also the biggest range in AMS, with the highest value close to 2,0. Samples 3 and 8 also holds elevated AMS values up to 1,55 and 1,35, respectively.
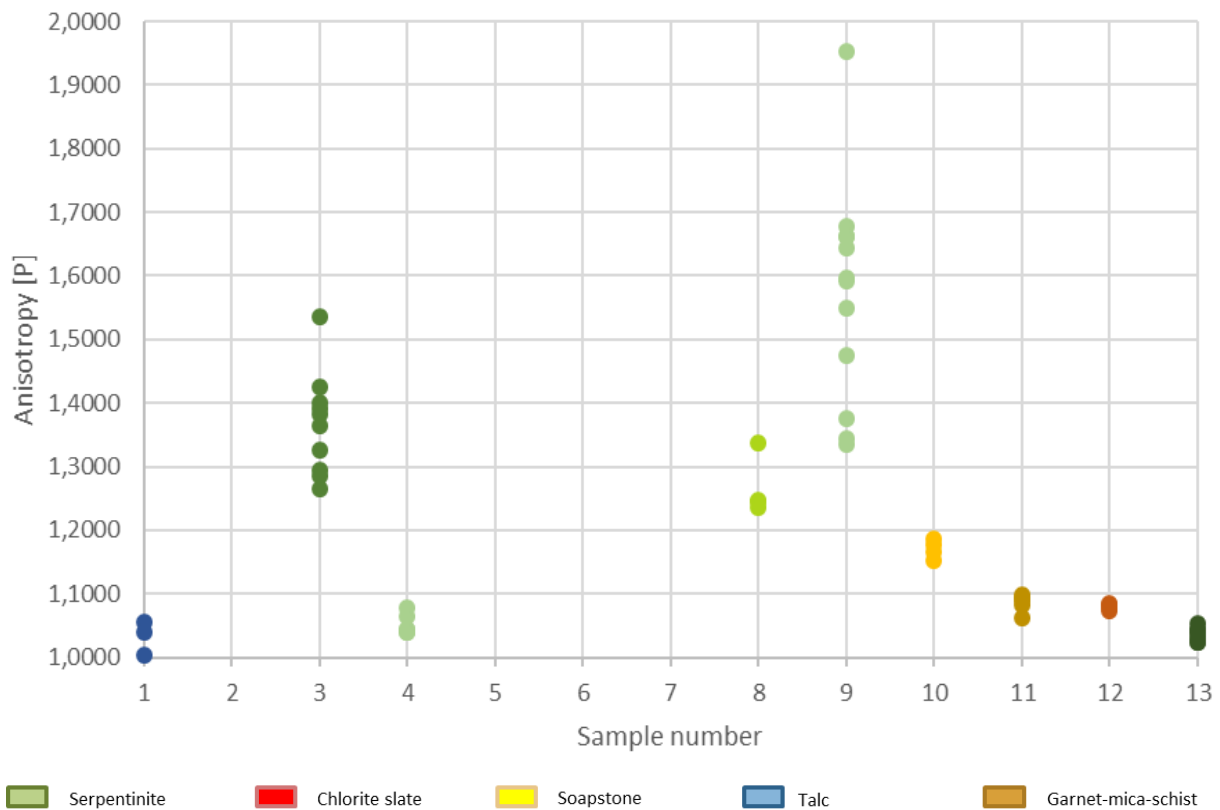
Figure 5-17: AMS from the oriented samples from the field. Each dot represents one cylinder. Some sample numbers are left empty, as there were no obtained oriented samples.

5.3.2 Density and NRM

The Density vs. NRM plot, shown in Fig 5-18, is obtained from the same cylinders as in Fig 5-16 and Fig 5-17. The plot shows a significant separation between the serpentinites and the other remaining lithologies. All the serpentinites have a higher NRM value compared to the different lithologies of approximately the same density. Furthermore, increasing density shows a good correlation with an increase in NRM for all lithologies. However, an increase in density for the serpentinites results in an increased NRM value compared to the other lithologies, as indicated with grey lines in the figure. Samples 3, 8, and 9 still plot in the upper range of NRM as they did in the density vs. susceptibility plot. Samples 3 and 9 plot quite similarly, while sample 8 has an even higher NRM- and density-value. Sample 10, the soapstone, plots with increased NRM values compared to the other low magnetic samples.

Fig 5-19 illustrates the geographical NRM directions obtained from the cylinders. Almost all of them have an upward inclination as the present-day field, except for the talc-cylinders and one serpentinite cylinder. The NRM directions have a wide distribution altogether, but plot closer within the same lithology. When considering only the serpentinites, their Fisher mean vector plots close to the present-day field.
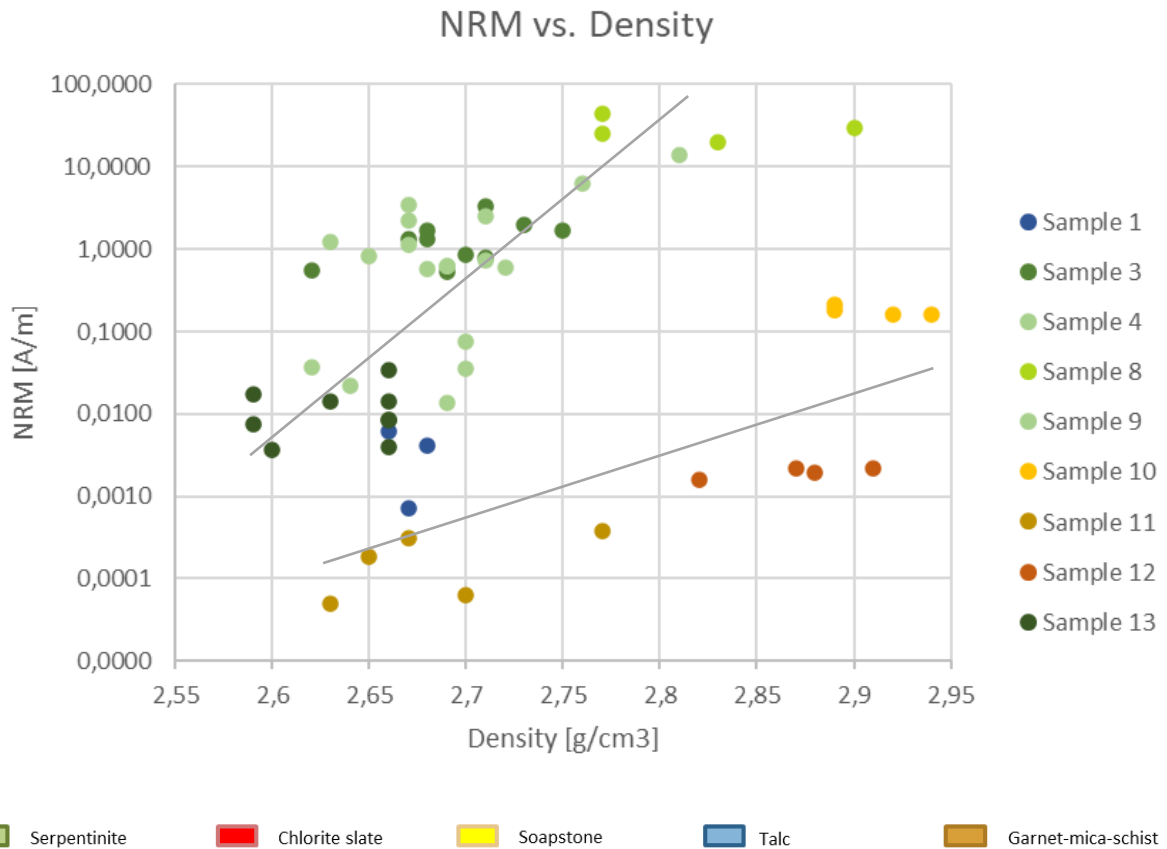
Figure 5-18: NRM versus density plot obtained from cylinders. The grey linear lines are trendlines for the two groupings. The NRM axis has a logarithmic scale. Sample localities are found in Fig 5-15.
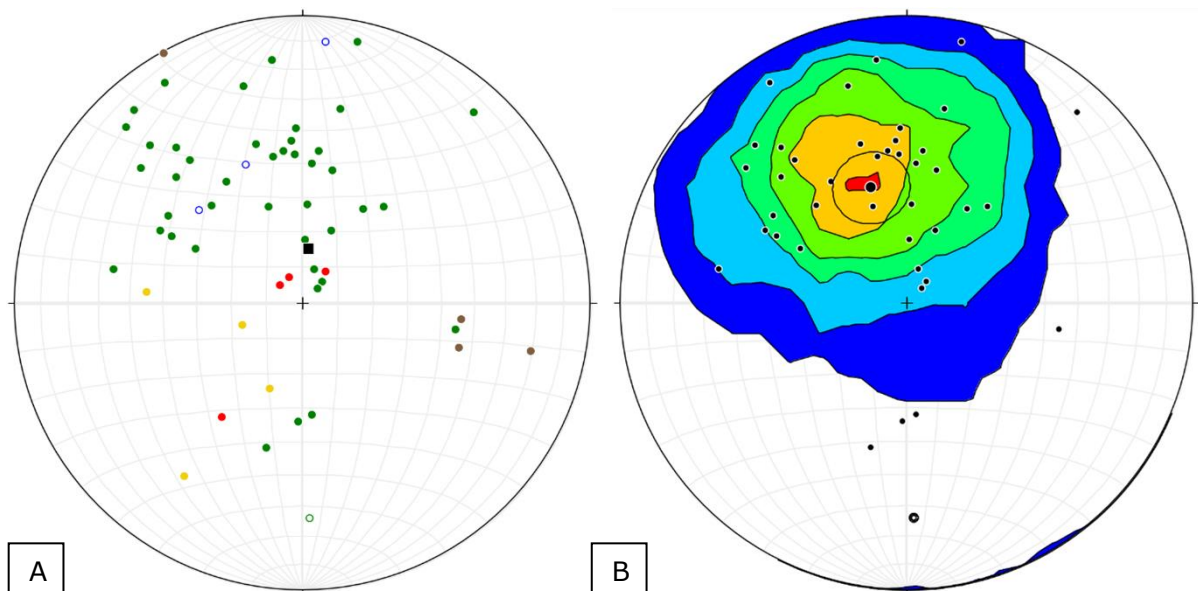
*Figure 5-19: Equal area stereonets with plotted NRM directions. Filled circle: upward inclination, open circle: downward inclination, black square: present-day field. **A**: Values from all lithologies (Sample 1, 3, 4, 8, 9, 10, 11, 12 & 12). **B**: Values from the serpentinites (3, 4, 8, 9 & 13) with contours. Big filled circle with an open circle around represent Ficher mean vector of 338 → 49.*

5.3.3 Q-value

Based on equation 8, the calculated Q-values show if the remanent or induced magnetization dominates within the cylinders. As illustrated in Fig 5-20, most of the samples plot with high precision, except for sample 4, which has a more significant spread. Induced magnetization dominates the chlorite slate, garnet mica-schist, and talc, while the remanent magnetization dominates within the soapstone. Most of the serpentinites plot with a Q-value <1, which indicates an induced dominated magnetization. However, sample 8, as well as some of the cylinders within sample 4, has Q-values closer to 10, which suggests a remanent dominated magnetization.
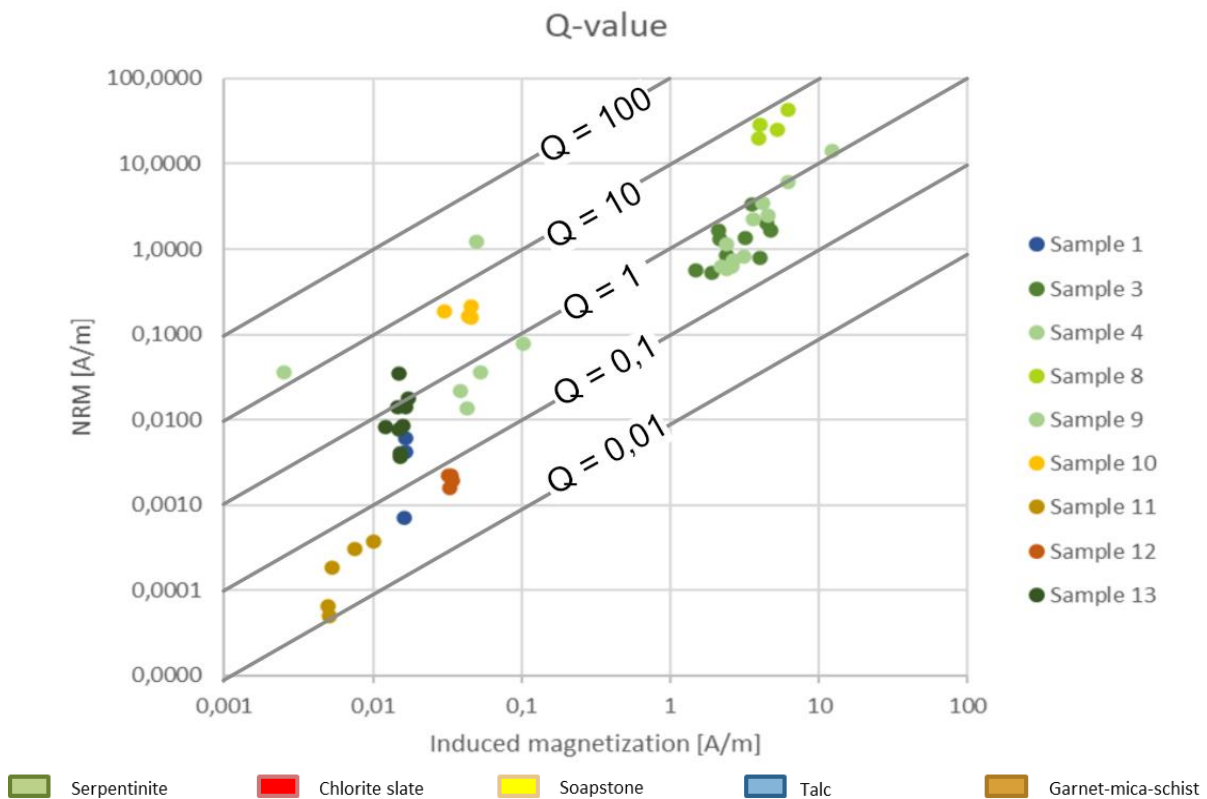
Figure 5-20: A Köningsberer ration (Q-value) plot based on NRM and induced magnetization by equation 8. Both axes have a logarithmic scale.

5.3.4 Calculated Magnetite Content

The potential magnetite content is calculated based on equation 6. As shown in Fig 5-21, all the cylinders plot within two distinct groups: one group with a low magnetite content (~0,01%) and one group with a higher magnetite content (~4%). Samples 3, 8, and 9 plot within the highest calculated volume% magnetite, with sample 9 containing one cylinder with a value of close to 9%. This value is almost ten times more than the average value of the lower group. As a general trend, increasing NRM results in a positive linear increase of the volume % magnetite.
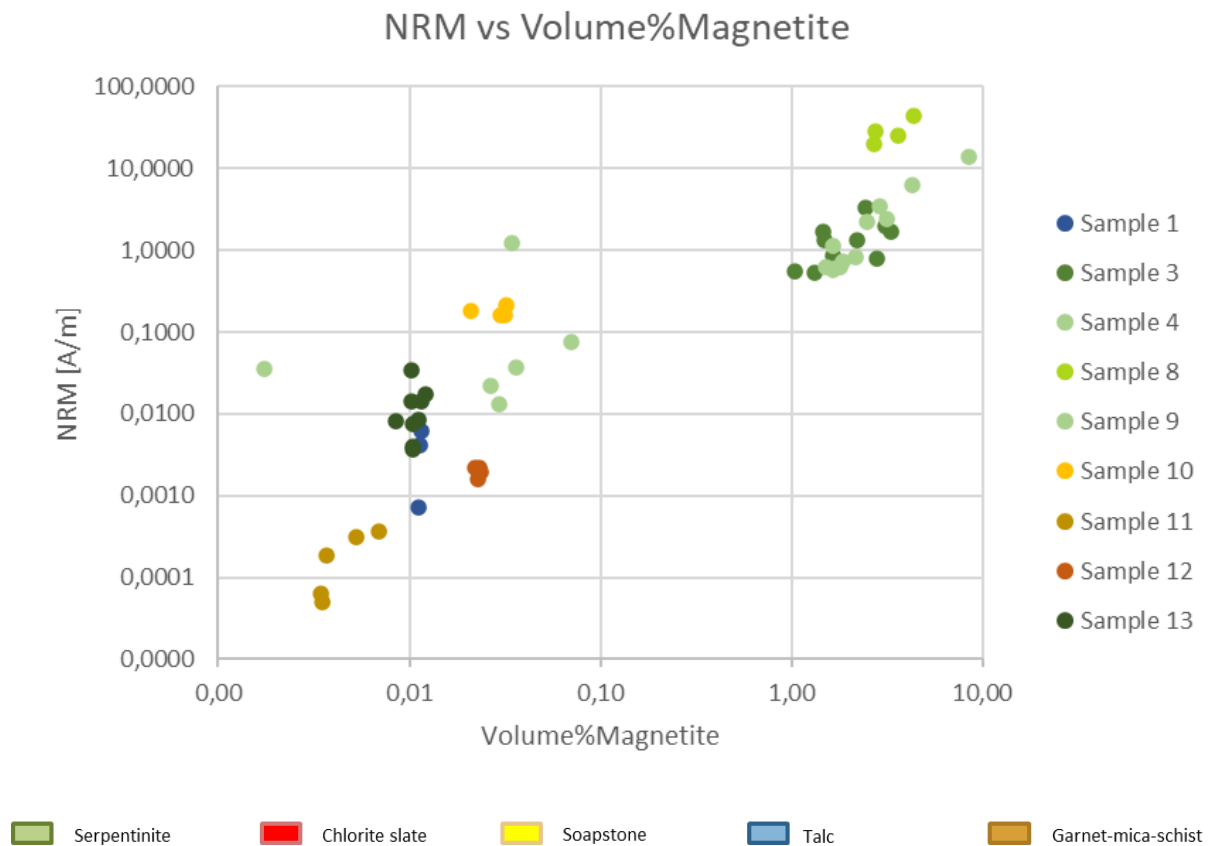
Figure 5-21: NRM versus Volume% magnetite from cylinders. The NRM axis is plotted on a logarithmic scale.

5.4 Mineralogical Zonation and Alteration in Magnetic Samples

Optical microscopy revealed, at an early stage, the appearance of zoned oxides in some of the samples. It was difficult to assign a mineral to each zone, and it was unclear if there could be more zoned oxides than the observed ones in optical microscopy. As the geophysical analysis also showed a clear division in magnetic properties, it was essential to investigate these oxides to fully understand the link between minerals and magnetic properties. As SEM is a semi-quantitative method, these results are indicators and not entirely reliable. A microprobe analysis would probably be more precise and consistent.

The brecciated serpentinite reveals significant (up to 1,5mm) zoned oxides surrounded by predominantly antigorite and magnesite. The size and number of zones within the oxides change between them. A general trend is the appearance of aluminum and chromium in the core that gradually develops towards a more iron-rich rim, as seen in Fig 5-22. Point analysis from the center to the rim indicates that the zones consist of minerals from the chromite-magnetite series in the spinel sub-group, as Mortenson (1973) also suspected. When looking at the normalized Cr/Fe ratio obtained from the point analysis in these zones, it is possible to assign each zone to a mineral within the chromite-magnetite series (Mindat, 2020b). Fig 5-25 illustrates how samples 2 and 3 mostly consist of iron-rich chromite variants and not magnetite as first assumed.

In addition to the large and zoned oxides, the brecciated serpentinite also contains smaller oxides (up to 0,4mm) surrounded by antigorite. They do not show the same zonation patterns and consist of magnetite. The magnetite is often surrounding magnesite, as seen in Fig 5-23.
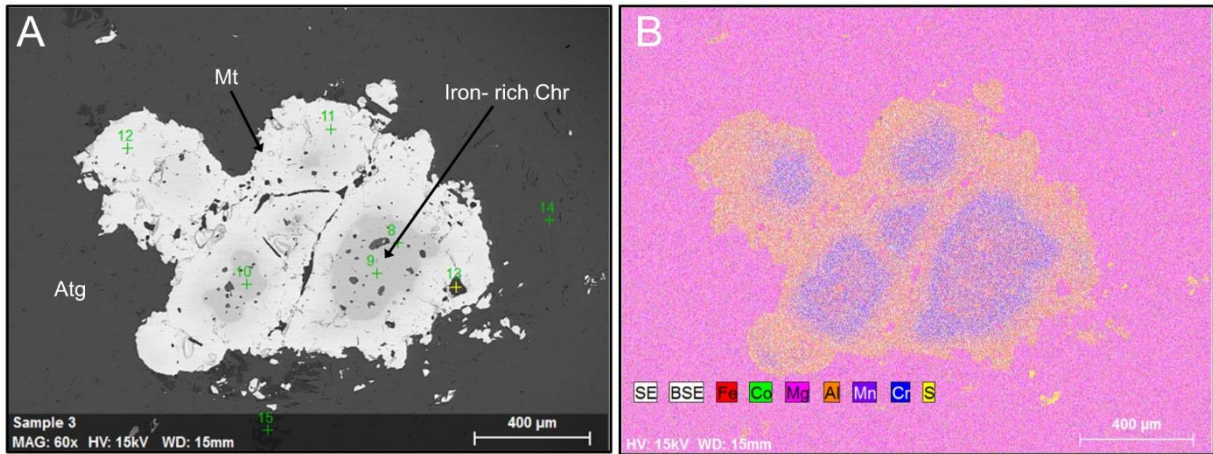
*Figure 5-22: SEM image of sample 3 – **A**: Zoned spinel grain with ferrian chromite (Chr) in the core gradually evolving to a magnetite (Mt) rim. Green numbers indicate the location of point analysis, summarized in Table 5. **B**: Mapped element distribution of zoned spinel grain. The grain has an aluminum and chromium-rich core and an iron-rich rim.*
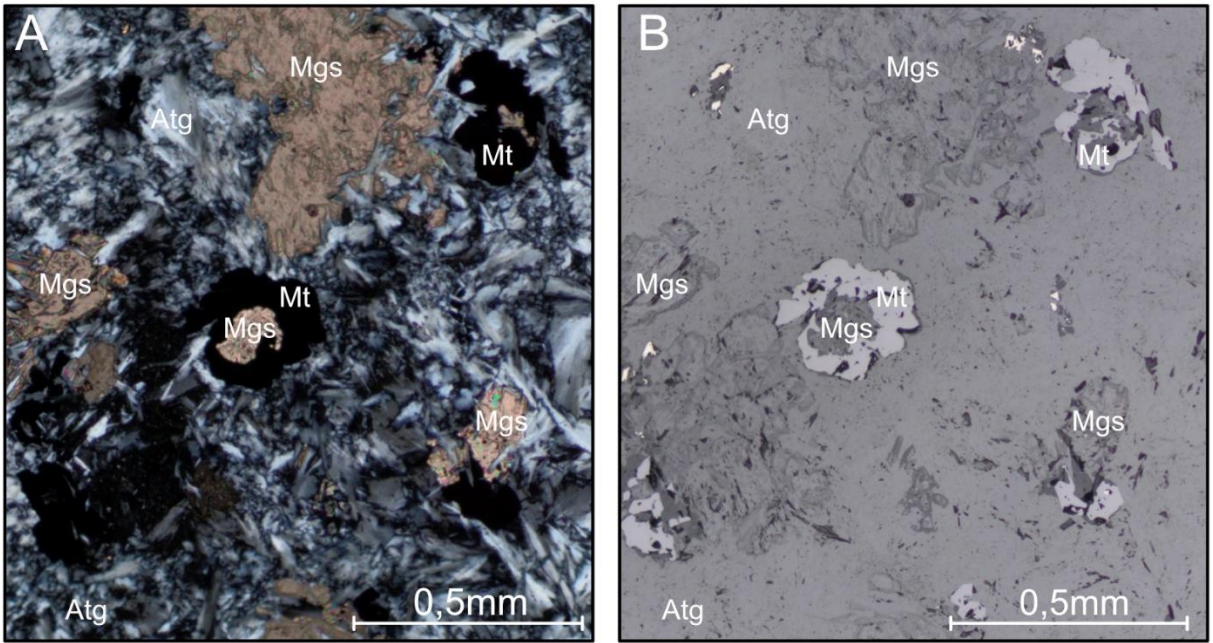
*Figure 5-23: Photomicrographs of sample 3 – **A** Magnesite (Mgs) grains with magnetite (Mt) rims around taken with Xpl in transmitted light. **B**: Same thin section area as in A, but taken with Ppl in reflected light.*

Table 5: Sample 3 - Point analysis from SEM. Fig 5-22 shows their location.

Point 8

Element	C Atom. [at. %]
Cr	17,57
O	48,49
Fe	12,78
Br	1,95
Al	4,72
C	10,53
Mg	3,93

Point 9

Element	C Atom. [at. %]
Cr	18,09
O	48,18
Fe	12,9
Br	1,96
Al	4,66
C	10,39
Mg	3,83

Point 10

Element	C Atom. [at. %]
Cr	17,85
O	48,24
Fe	13,05
Br	1,87
Al	4,88
C	10,29
Mg	3,57
Zn	0,25

Point 11

Element	C Atom. [at. %]
Fe	27,35
Cr	16,38
O	45,91
C	9,33
Mg	1,03

Point 12

Element	C Atom. [at. %]
Fe	41,85
O	45,33
C	10,66
Cr	2,21

Sample 8 is representative of the dark green serpentinite and is the most magnetic sample. Optical microscopy did not show any sign of mineral zonation, and the abundance of significant oxides is less compared to the brecciated serpentinite. By looking for mineral zonations using the SEM, it became evident that the majority of grains do not show a zonation pattern. However, some oxides clearly show an element zonation, as seen in Fig 5-24. The chromium-rich core is not as significant as in the brecciated serpentinite, and it has an accumulation of heazlewoodite in its outermost edges (see Appendix D for classification). As seen in Fig 5-24, haezelwoodite is seemingly confined to the surrounding olivine vein's structures.

Besides the larger oxides, the dark green serpentinite also holds micromagnetites. They occur both within the grains and on grain boundaries and do not show a clear zonation pattern. However, they sometimes contain increased amounts of chromium.
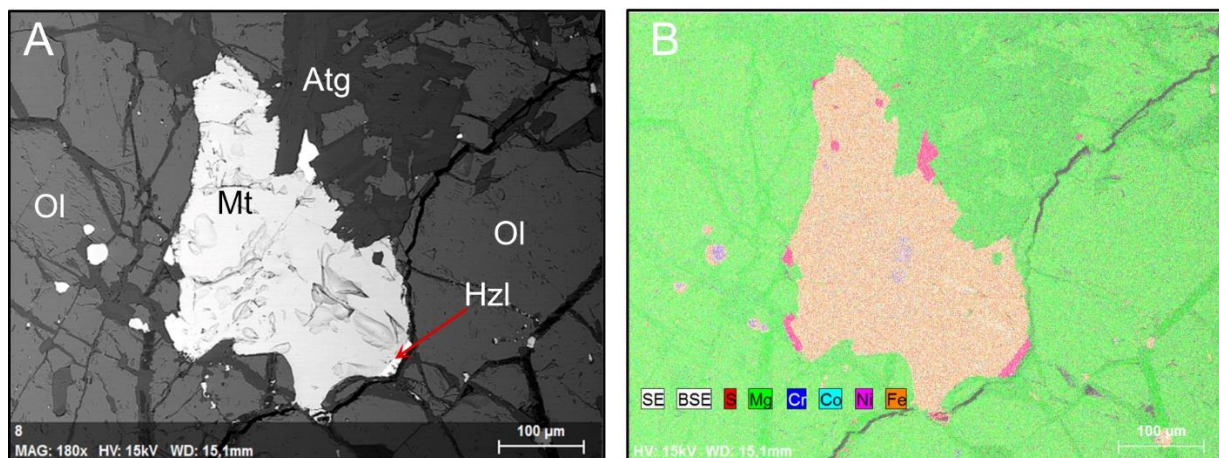
Figure 5-24: SEM image of sample 8 –A: BSE image of magnetite (Mt) grain surrounded by antigorite (Atg), olivine (Ol), and haezelwoodite (Hzl). B: Element mapping of the same magnetite grain as in A. The grain has a slight chromium-rich core and an accumulation of haezelwoodite in its outermost corners.

42

By comparing all the point analysis taken on the oxides from the magnetic samples, it is possible to assign a mineral within the spinel subgroup by looking at the normalized Cr/Fe ratio.

As seen in Fig 5-25, samples 2 and 3 (brecciated serpentinite) plot with a big scatter from ferrian chromite to magnetite. The magnetite points represent the rim in the zoned oxides and the smaller magnetite grains, while the chromium-rich points represent the core of the zoned oxides. All point locations are added to the Appendix at the end.

Even though a zonation pattern in sample 8 (dark green serpentinite) was not observable in optical microscopy, the SEM revealed a weak zonation pattern. As seen in Fig 5-25, the point analysis plot with a lower Cr/Fe ratio than the brecciated serpentinite, indicating that most of the oxides consist of magnetite. Furthermore, the most chromium-rich sample plots within the lower part of the ferrichromite field and represents the core of a zoned oxide. Compared with the core of the brecciated serpentinite, the dark green serpentinite is more iron-rich.
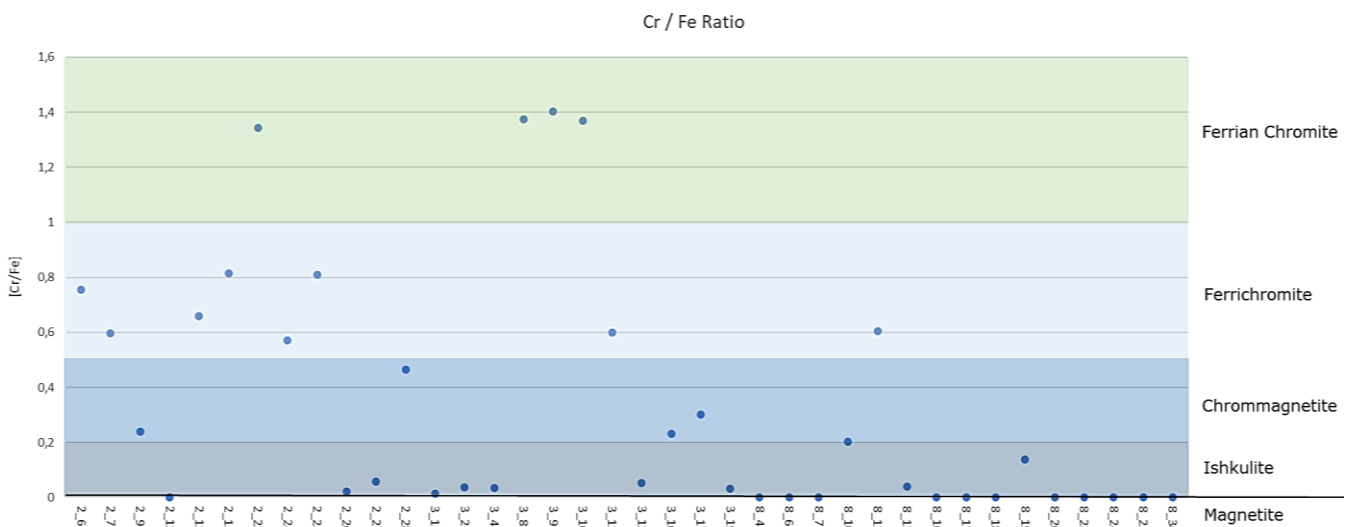
Figure 5-25: Chromite-magnetite subgroup mineral classification based on Cr/Fe ratio calculated from normalized point analysis from SEM.

5.5 Geophysical Modeling

5.5.1 Ground Magnetic Survey

As most of Slipsteinsberget and its surrounding areas are covered by vegetation, the ground magnetic survey was crucial in the investigation of lithological contacts. After treating the data obtained from the survey in Geosoft, it was used to create a total magnetic intensity (TMI) map over the field area, as shown in Fig 5-26. A gridding cell size of 1m and minimum curvature gridding (Dentith & Mudge, 2014) kept the data precise and accurate, which allowed detailed mapping of minor variations within the quarry. As seen in Fig 5-26, the TMI map has two distinct anomalies: one mostly positive anomaly over Slipsteinsberget (with values between 52,000 and 55,900nT), and one smaller anomaly with both a positive- and a negative signal ("Anomaly 2" with values of respectively 56,000 and 50,000nT). Due to lack of rock samples, "Anomaly 2" is left out from the primary modeling and is instead compared to the anomaly over Slipsteinsberget in the discussion section. Furthermore, the TMI map shows two very weak positive anomalies (with values between 51,900 and 52,700nT) marked by red stippled lines. These areas are essential when considering the regional background value for modeling (see section 5.5.3).
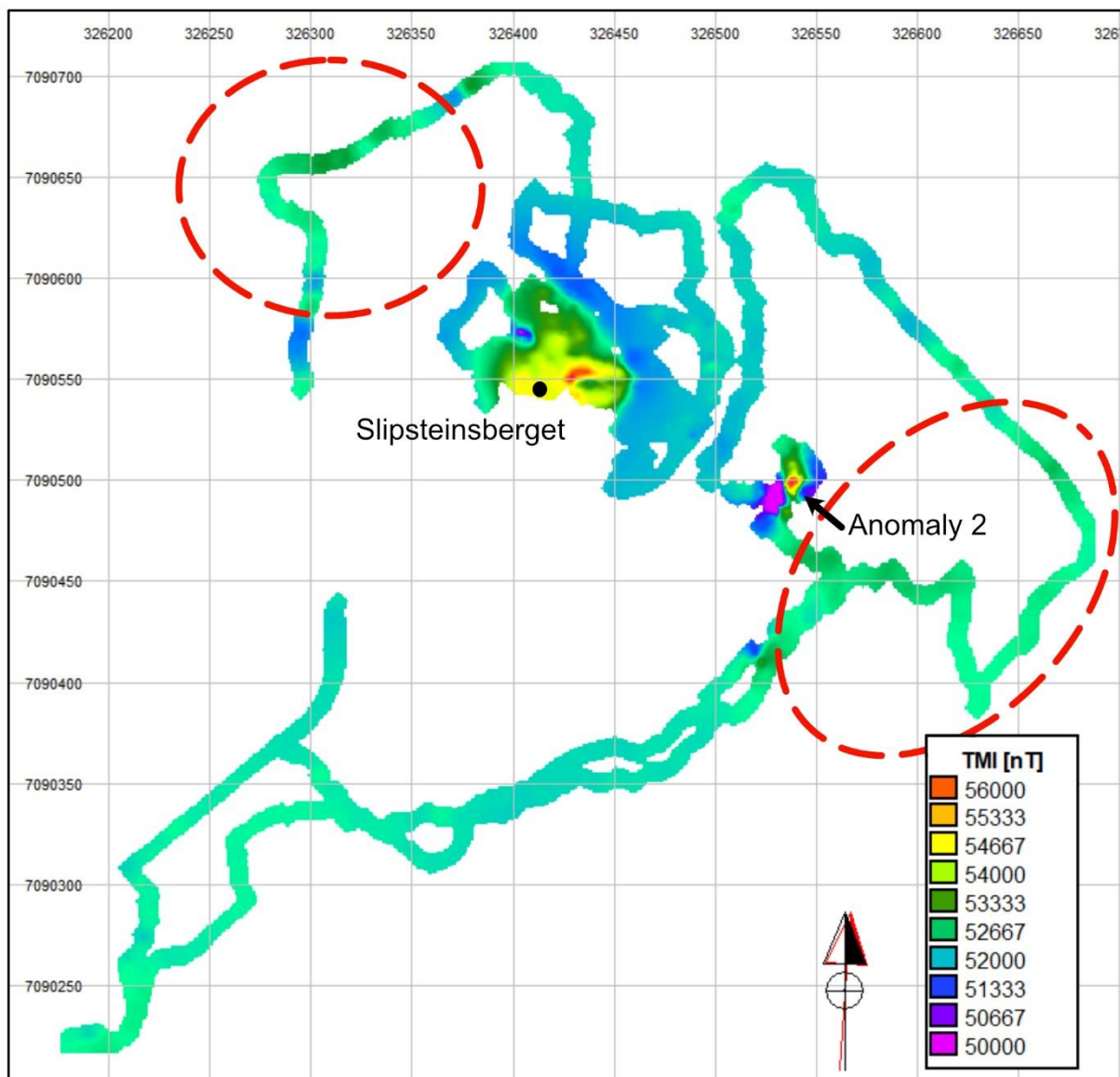
Figure 5-26: TMI map over Slipsteinsberget and its immediate enclosing rocks displayed with "Cray's Rainbow" palette. Red stippled circles indicate a weak positive anomaly. WGS84/UTM33N.

The coordinate system displayed in the maps is WGS84/UTM 33N. Focusing on Slipsteins-berget, the TMI shows some very interesting features in Fig 5-27. The outermost edges contain low TMI values, while the center, where Slipsteinsberget's quarry is located, show some highly elevated values. The magnetic anomaly has a distinct circular shape with abrupt and sharp edges. However, a slight variation in anomaly steepness occurs between the western and eastern sides. The west side of the anomaly does not contain as much data as the east side. However, it is possible to observe a broader wavelength on the west side compared to the east side. Further from the quarry, the TMI signal decreases away from the high values in the center before it slightly increases again in the outermost edges, creating a local negative anomaly around it. The negative anomaly is strongest in the northeastern side. A strong negative anomaly is also located within the quarry, right above bench four, but this anomaly is ignored in the modeling as it is the result of human activity, the removal of a drill rig.

Although Slipsteinsberget's topography expresses an almost circular dome, the magnetic response within it is not oriented in the same manner. The overall positive anomaly has a less magnetic part (dark green color on TMI map) on the northern side, as well as along the outermost edges. This zone correlates well with the observed brecciated serpentinite exposed in the quarry. As the top of the quarry is covered by vegetation, the TMI map reveals that the brecciated serpentinite most likely continues further north, where the owners of Slipsteinsberget have not yet been mining. A moderately high magnetic zone (yellow color on TMI map) dominates closer to the center of the anomaly and comprises most of bench four. This magnetic zone was not directly distinguishable in lithology in the field. However, the highest value within the whole survey (red color in TMI-map) correlates with the dark green serpentinite. It is located on the corner immediately above bench three. The highly magnetic body appears to have northeast to southwest strike and is slightly bent. Furthermore, an elevated signal is also detected on the south-western corner of bench three. As they are both located along edges, care was taken to assure that the signals are not a topographically created effect.
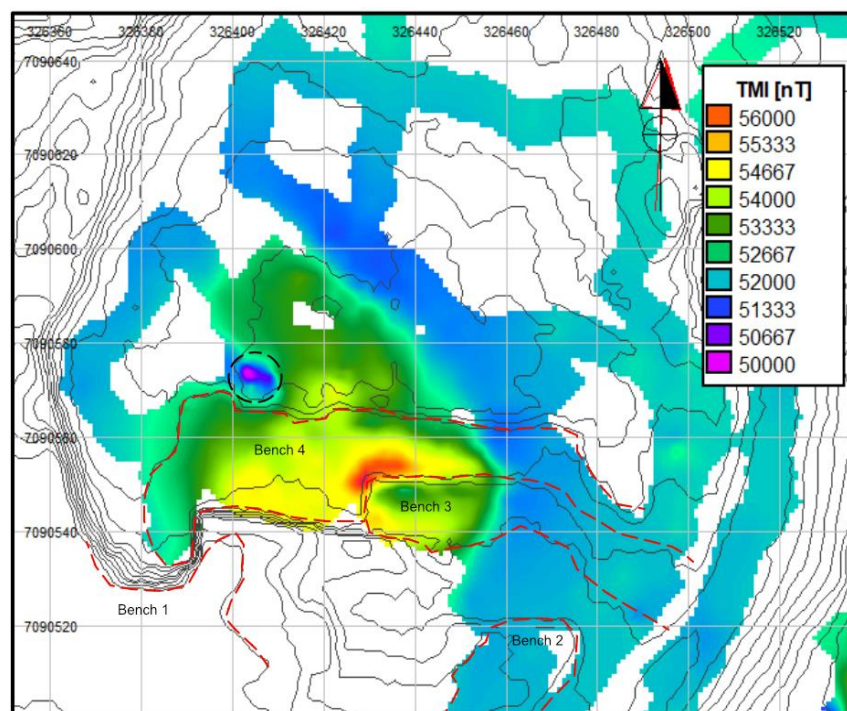
Figure 5-27: TMI over Slipsteinsberget displayed with "Cray's Rainbow" palette together with elevation contour lines in black. Equidistance = 2m. Red stippled lines indicate the edge of the benches, as defined in Fig 5-1. Black stippled circle shows the ignored magnetic low anomaly.

5.5.2 Constraints

Because, in theory, an infinity number of subsurface geometries with different susceptibility- and NRM-values can result in the same magnetic response, it was crucial to collect geological constraints to obtain a model as close as possible to reality. These constraints include field mapping, rock sampling, and lab analysis, as described previously.

The field mapping helped in placing the correct lithologies on the surface of the model. Two susceptibility-profiles along the walls of bench three and four reveled the magnetic properties in places where it was not possible to walk with the magnetometer. These profiles can be seen in Fig 5-28. Both profiles correlate quite well in the east with low susceptibility values outside the magnetic anomaly. The readings increase at the same location as the TMI-map does and are consistently high over most of the magnetic center. However, there is a slight mismatch in the measured susceptibility values on the western side of the anomaly. The TMI-map shows elevated values, while the susceptibility measurements indicate a nonmagnetic rock. Furthermore, the field mapping helped in predicting the subsurface. As the serpentinites did not show any tectonic indicators, the foliation of the surrounding garnet mica-schist was used for subsurface modeling.
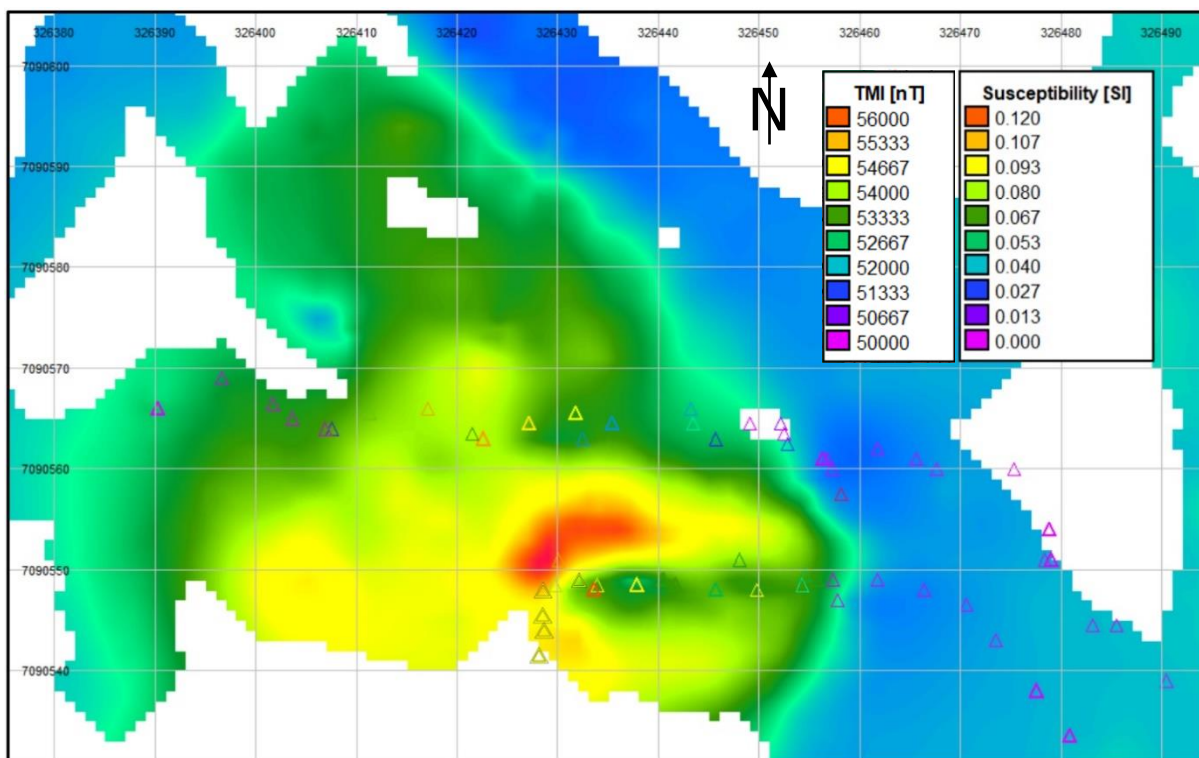
Figure 5-28: Susceptibility values (triangles) compiled from a handhold instrument superimposed on the TMI-map. The values are color-coded, as shown in the legend.

As several bodies with different magnetic properties can produce the same TMI-signal, it was crucial to assign correct magnetic properties for the modeled bodies. Oriented outcrop samples taken from the different lithologies were turned into cylinders that, with extensive lab testing, yielded suitable susceptibility, NRM value, and NRM direction measurements. These are listed in Table 6 and create important constraints on the model.

Finally, seven borehole cores stored at the Løkken Drill Core and Sample Center were investigated to connect the geophysical model to the geology were penetrated in the subsurface, at true depths. Unfortunately, the drill cores were taken on the west side of Slipsteinsberget and mostly consist of garnet mica-schist and talc; see Fig 5-29 for their location and orientation. In addition, a lot of the core material was missing, so the interpretation was limited. Borehole 15 encountered the green low magnetic serpentinite at a

46

depth of 15m and to the end of the core at 30m. This observation places the green serpentinite at a specific depth at a specific location. For the rest of the boreholes, they only helped in understanding where not to put the serpentinite.

5.5.3 Modeling

3D magnetic modeling was conducted to get a better understanding of the geometry and depth extent of the Slipsteinsberget serpentinite bodies. As illustrated in Fig 5-27, only some parts of Slipsteinsberget are magnetic. The none to very low magnetic bodies were not included in the modeling but instead were treated as a part of the background. A best-fit model of the serpentinites will be presented, together with maximum- and minimum-volume models for the magnetic rocks.

Before modeling, the regional background field had to be calculated. Aeromagnetic data over the area, provided by NGU, together with the ground magnetic survey (GMS), made it possible to calculate a suitable background value. As seen in Fig 5-26, the ground magnetic survey detected two weak positive anomalies outside Slip

Figure 5-29: Borehole location on the western side of Slipsteinsberget. Modified after Hultin 1964.

steinsberget. Combined with aeromagnetic data in Fig 5-30, it is evident that these anomalies correlate features on the aeromagnetic map. Furthermore, the acquisition lines show that Slipsteinsberget's anomaly is located between the flight lines and does not affect the aeromagnetics. Therefore, the aeromagnetic data could be used to construct a regional background field to avoid any disturbance from the prominent features outside Slipsteinsberget.

Two points with data from both the GMS-map and the aeromagnetic map were needed to create a representative regional background field. The points, highlighted in Fig 5-30, were chosen based on their signal from both Slipsteinsberget's anomaly and the two bigger prominent anomalies. It was desirable to have a low reading with few disturbances from the anomalies. The values of the aeromagnetic map in these two locations were recalculated to match the same values as the GMS-map at those exact positions. Then, the known factor and offset between them were used to adjust the whole aeromagnetic map:

$$\text{Regional background field} = \ (\text{Aeromagnetic map} - \text{mean}(\text{Aeromagnetic map})) * \text{factor} + \text{offset} \qquad (16)$$

$$\text{Factor} = 3.515$$

$$\text{Offset} = 51879 \ \text{nT}$$

$$\text{mean}(\text{Aeromagnetic map}) = \ -279\text{nT}$$

47

Figure 5-30: GMS map with an aeromagnetic map as a base layer. Different linear color scales displayed with the "Pseudocolor" palette. A = GMS-map, B = Aeromagnetic map. Black lines = flight lines, black circles = selected points for regional the background field.
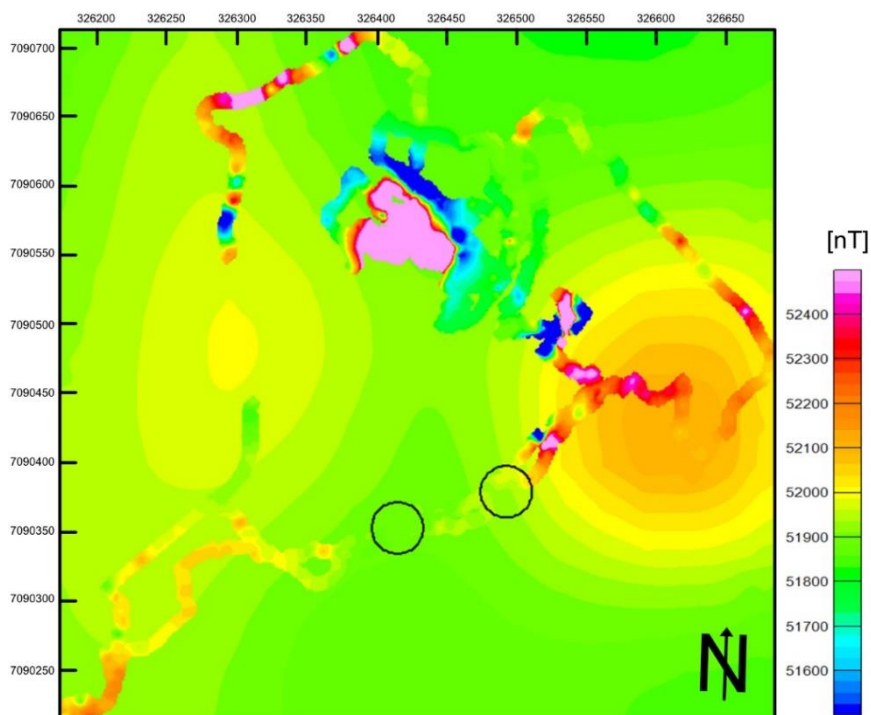
Figure 5-31: Calculated regional background field with a GMS map on top. They have the same color scale displayed by the "Pseudocolor" palette. Black circles = selected points for the regional background field.

48

Accordingly, a regional background field is obtained, as seen in Fig 5-31. The new map has the same color scale as the GMS, and their values at the two locations coincide. Other methods for calculating a regional background field exists (e.g., linear trend), and would probably result in a similar model as the regional background field is minimal compared to the measured TMI from the GMS. However, a linear trend would not be able to capture the highs marked in Fig 5-26 that are also found on the aeromagnetic data.

Ten profiles across the magnetic part of Slipsteinsberget are modeled. As Slipsteinsberget does not exhibit any obvious structural constraints, the profiles are placed parallel to the foliation of the surrounding garnet mica-schist to allow modeling along its strike with the use of "true dip", assuming the same orientation for the serpentinites. Furthermore, the profiles are strategically placed directly above prominent features for more precise modeling. The width of the bodies within one profile is the same, but they change between the profiles in such a way that the bodies align and leave no space.

The different bodies were chosen based on the extensive testing of cylinders combined with the lithological and petrophysical understanding. The green-, brecciated-, and dark green serpentinite showed a clear division in magnetic properties and appearance and were therefore presented as three different bodies. Their magnetic properties used in the modeling are displayed in Table 6. Each body has a constant susceptibility and NRM-value. The other rocks within Slipsteinsberget did not have a strong magnetic signal, as seen in Table 7. Modeling with these bodies would be challenging as there are too few constraints and multiple options for their subsurface geometries.

Table 6: Magnetic properties for the modeled serpentinites

Body	Susceptibility [SI]	NRM intensity [A/m]	NRM orientation	
			Inclination	Declination
Brecciated serpentinite	0.008	2.17	51	328
Dark green serpentinite	0.100	29	45	359
Green serpentinite	0.001	0.02	67	014

Table 7: Magnetic properties for the low magnetic lithologies

Body	Susceptibility [SI]	NRM intensity [A/m]	NRM orientation	
			Inclination	Declination
Chlorite slate	0.001	0.002	83	249
Soapstone	0.001	0.180	56	234
Talc slate	0.0004	0.004	38	342
Garnet mica-schist	0.0001	0.0002	45	078

5.5.3.1 Maximum- and Minimum Volume Model
Only the brecciated serpentinite and the dark green serpentinite are included in the model as they both have a strong magnetic response. The green serpentinite has a weak, almost negligible, effect on the modeled curve, as demonstrated in Fig 5-32. It was therefore left out and treated as a part of the background. It would be possible to model significant volumes of the green serpentinite without affecting the anomaly curve; the model is simply insensitive to volume changes of this type of serpentinite.

For 3D modeling, the colors red, orange, and blue have been used for the serpentinites instead of variants of green, as in 2D, in order to enhance the visibility of the different serpentinites. The maximum volume model, as seen in Fig 5-33, has a maximum thickness of approximately 50m and a calculated volume of 6 210 079m^3. The model is thickest in the center and gradually gets thinners towards the edges, especially in an east-west direction. The model demonstrates how the brecciated serpentinite follows the garnet mica-

schists orientation with a south-western dip direction. Seen together with LiDAR data from Slipsteinsberget in Fig 5-35, the model is confined to the south-western part of the hill.

The minimum volume model, as seen in Fig 5-34, has a more uniform thickness of approximately 10m compared to the maximum model. The minimum model has an elliptical shape and is elongated in an east-western direction with a calculated volume of 28 605m^3. The bodies are confined to the very top of Slipsteinsberget and follow the orientation of the garnet mica-schist. Seen together with LiDAR data over Slipsteinsberget in Fig 5-36, the minimum volume model has a more significant extent than the maximum volume model.
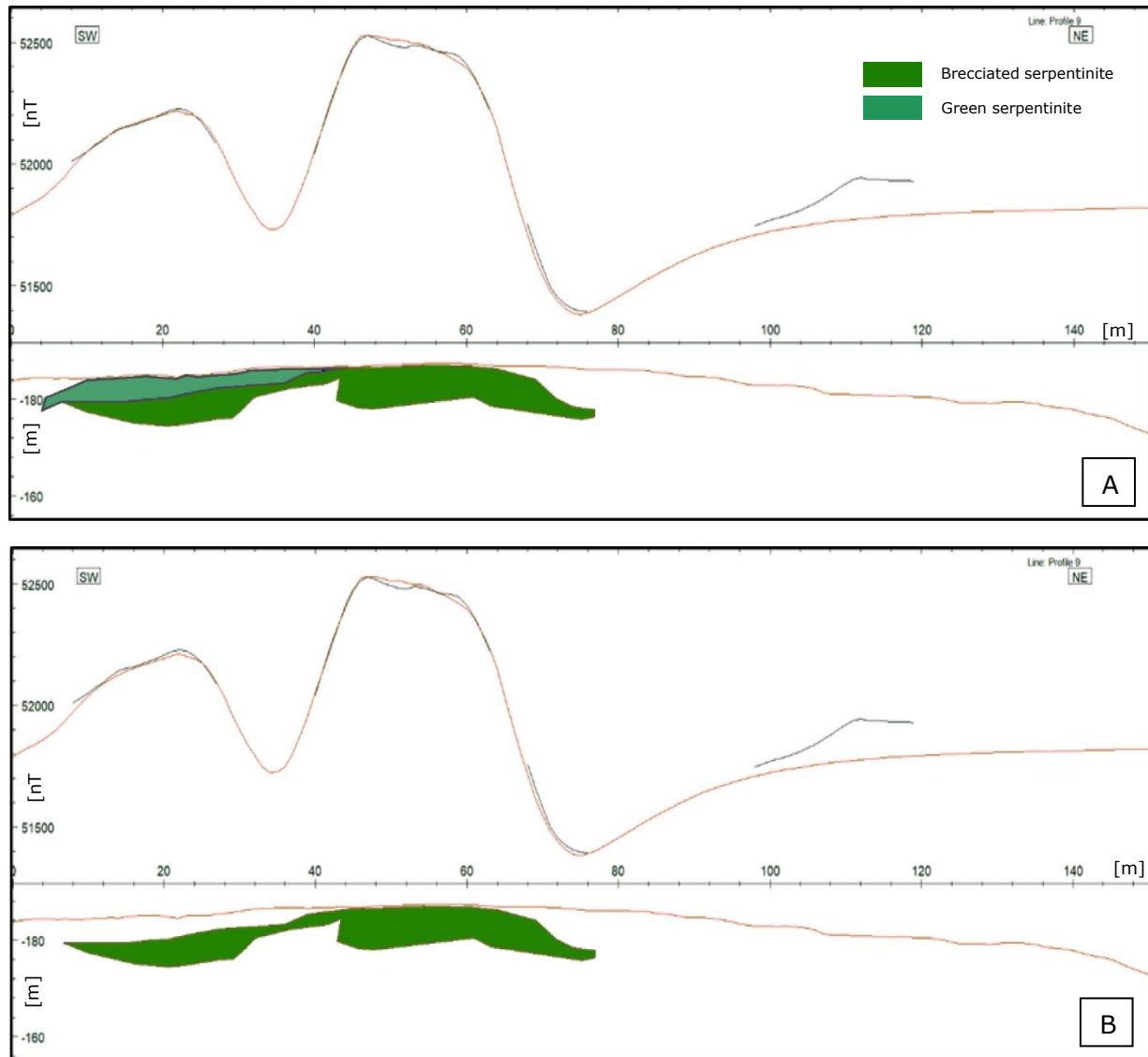
*Figure 5-32: Profile 9 in the maximum volume model. The profiles illustrate how little the green serpentinite contributes to the modeled graphs. **A**: Model containing green serpentinite. **B**: Same model, but without the green serpentinite. The curves are almost identical, but with a slight, practically non-detectable decrease in B.*
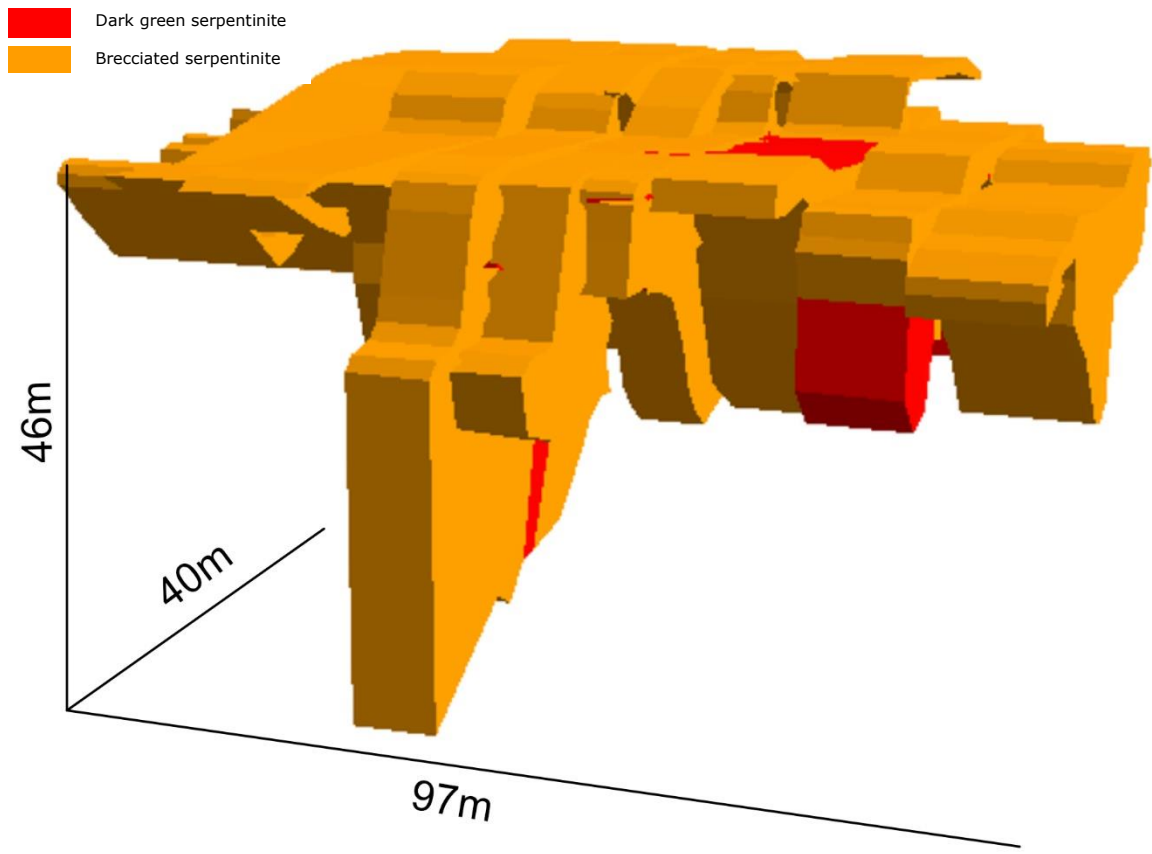
Figure 5-33: Maximum volume model. The model is seen with an azimuth of 5 and an inclination of 10. The scale is valid for the maximum extent.
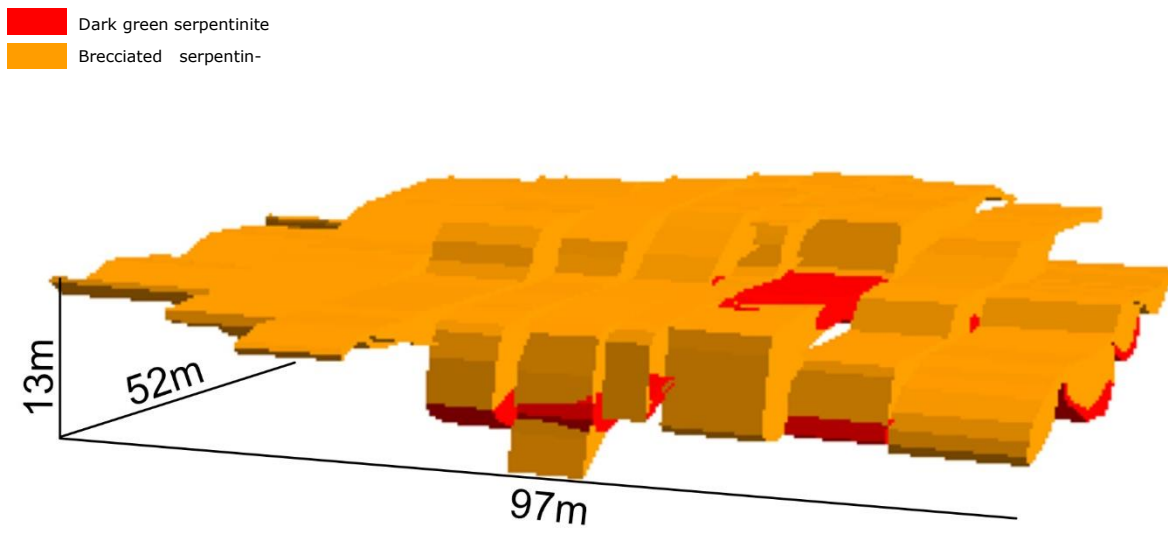
Figure 5-34: Minimum volume model. The model is seen with an azimuth of 5 and an inclination of 10. The scale is valid for the maximum extent.
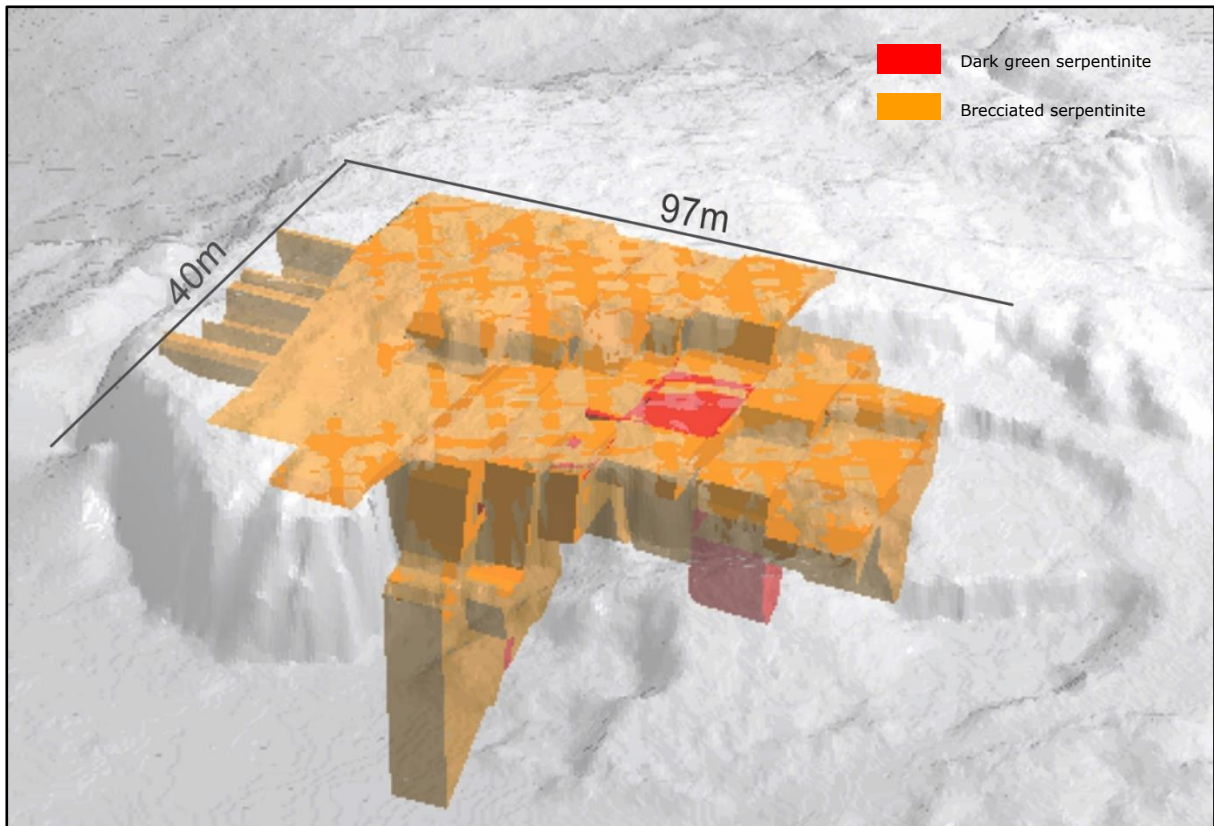
Figure 5-35: Maximum model combined with LiDAR data over Slipsteinsberget. The model is seen with an azimuth of 5 and an inclination of 30. The scale is valid for the maximum extent. See Fig 5-33 for maximum thickness.
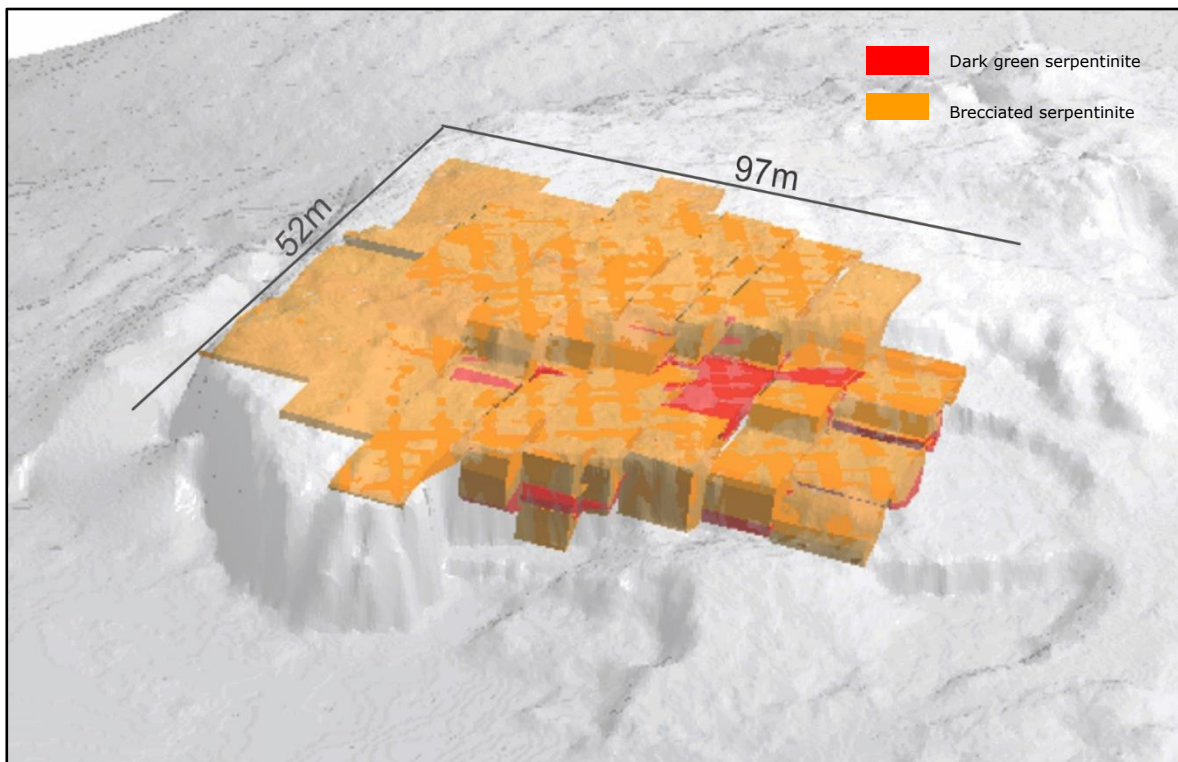
Figure 5-36: Minimum model combined with LiDAR data over Slipsteinsberget. The model is seen with an azimuth of 5 and an inclination of 30. The scale is valid for the maximum extent. See Fig 5-34 for maximum thickness.

5.5.3.2 Most-likely Model

The most likely model includes both the green serpentinite, the dark green serpentinite, and the brecciated serpentinite. The green serpentinite (blue) is incorporated, despite its low magnetic response, to represent the geometry of the serpentinites better.

As seen in Figs 5-37 and 5-38, the most-likely model has an elliptical shaped geometry with a dip direction towards the southwest. Furthermore, the modeled bodies are thicker in the western part of Slipsteinsberget (the modeled serpentinites have a maximum thickness of approximately 40m) and show a clear elliptical zonation pattern. The magnetic dark green serpentinite appears in the center of the model, enclosed in the brecciated serpentinite, which again is surrounded by the green serpentinite. However, due to excavation of masses within the quarry, the center of the zoned model is present at bench three, as the overlying masses are gone. Fig 5-37 illustrates how the serpentinites outcrop in the quarry.
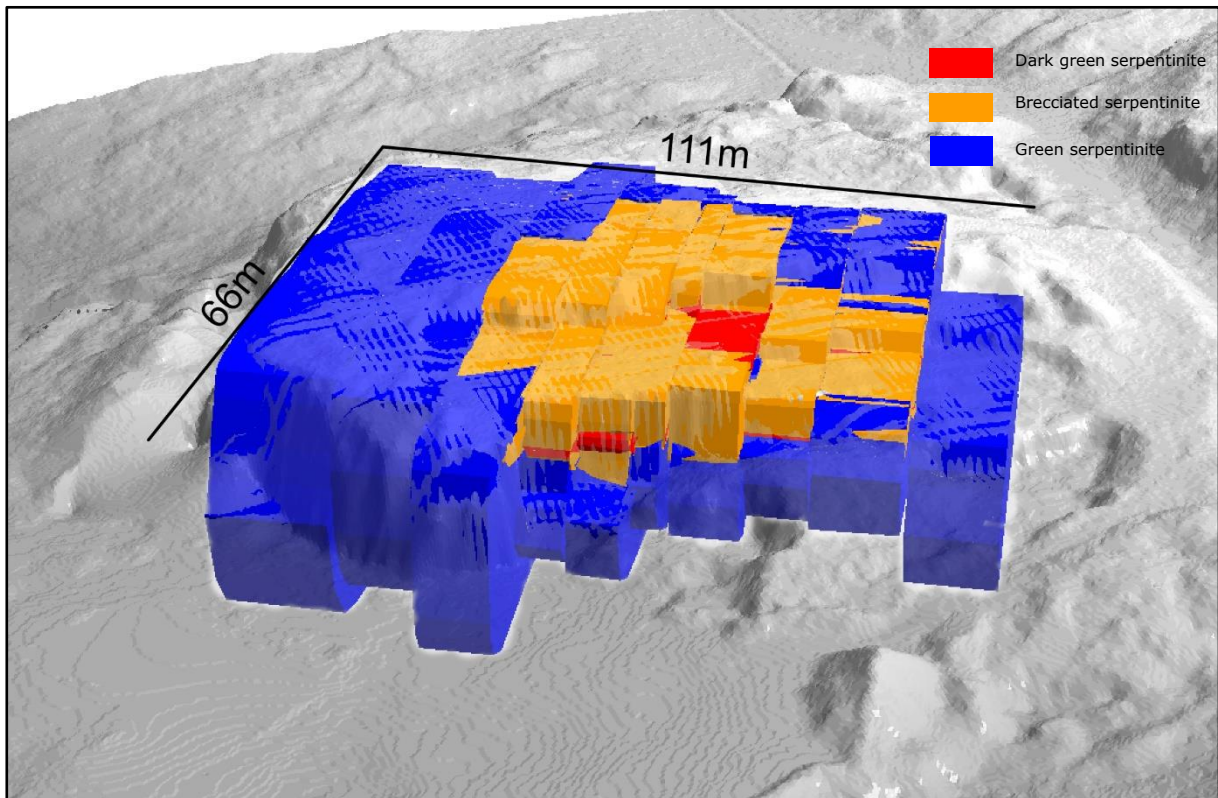
Figure 5-37: The most likely model, combined with LiDAR-data, is seen with an azimuth of 20 and an inclination of 24. The scale is valid for the maximum extent. See Fig 5-38 for modeled profiles over Slipsteinsberget with a precise scale.

For a volume assessment of the most likely model, the green serpentinite is left out of the calculations as in the maximum- and minimum models. As seen in Table 8, the most-likely model has a calculated volume of 124 965m^3, which is closer to the size of the minimum volume model than the maximum volume model. When adding the low-magnetic green serpentinite to the most-likely model, with a modeled volume of 174 961m^3, this leads to a total volume of 299 926m^3 for the three different serpentinites.

Table 8: Volume assessment of the magnetic serpentinites based on modeling

Model	Dark green serpentinite [m^3]	Brecciated serpentinite [m^3]	Total [m^3]
Maximum	3 308	6 210 079	6 210 079
Minimum	5 161	23 444	28 605
Most-likely	4 371	120 594	124 965
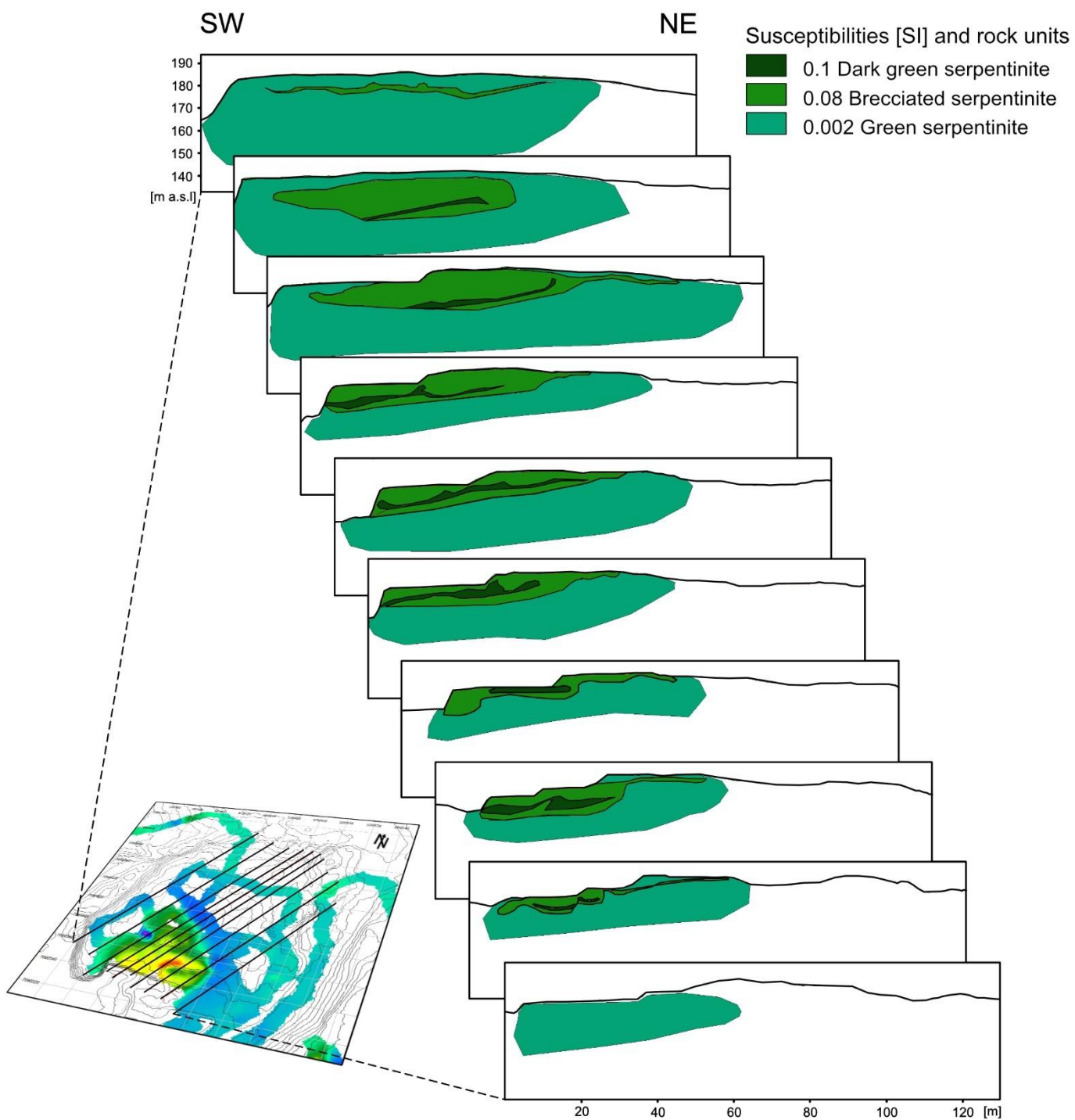
Figure 5-38: Most likely modeled profiles over Slipsteinsberget. Their location is seen in the TMI-map obtained by the ground magnetic survey (see Fig 5-27 for scale). They all have the same SW-NW orientation and the same scale. The dark horizontal line within the profiles represents topography.

When comparing the dark green serpentinite bodies in all the models, it is evident that there is a big difference in geometry and orientation. The maximum model has a much steeper orientation, almost vertical, than the minimum and most-likely model, and contains a Y-shaped body, as seen in Fig 5-39a. The minimum- and most-likely models have a geometry that looks like a curved horizon, as seen in Figs 5-39b and 5-40. Furthermore, the bodies in the maximum model are chaotically placed compared to the minimum- and most-likely model, where the dark green serpentinite appears as an almost continuous horizon. In the most likely model, the dark green serpentinite starts as a nearly continuous layer in the west that splits into two parts in the east, where the dark green serpentinite has a U-shaped geometry.
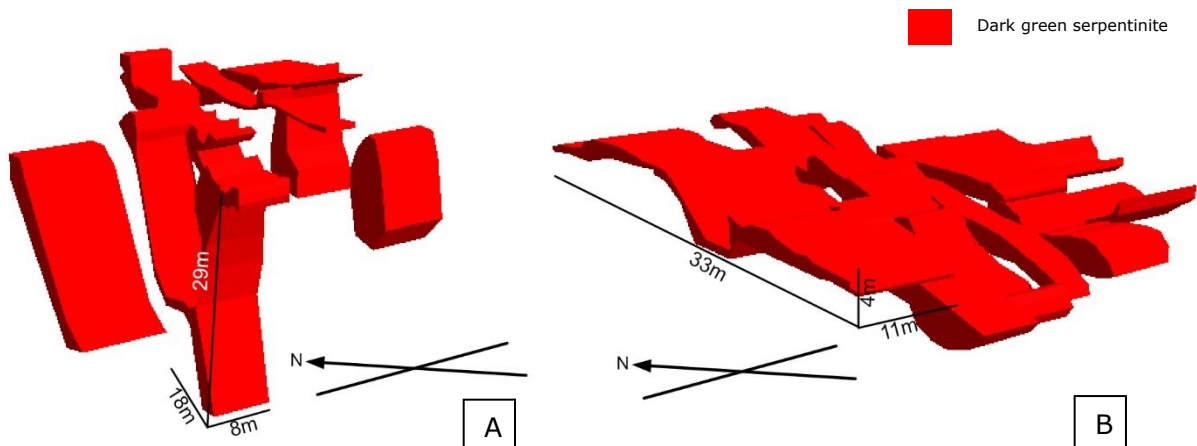
*Figure 5-39: Dark green serpentinite bodies in **A**: maximum model and **B**: minimum model. The scale is representative of the body it is placed next to.*
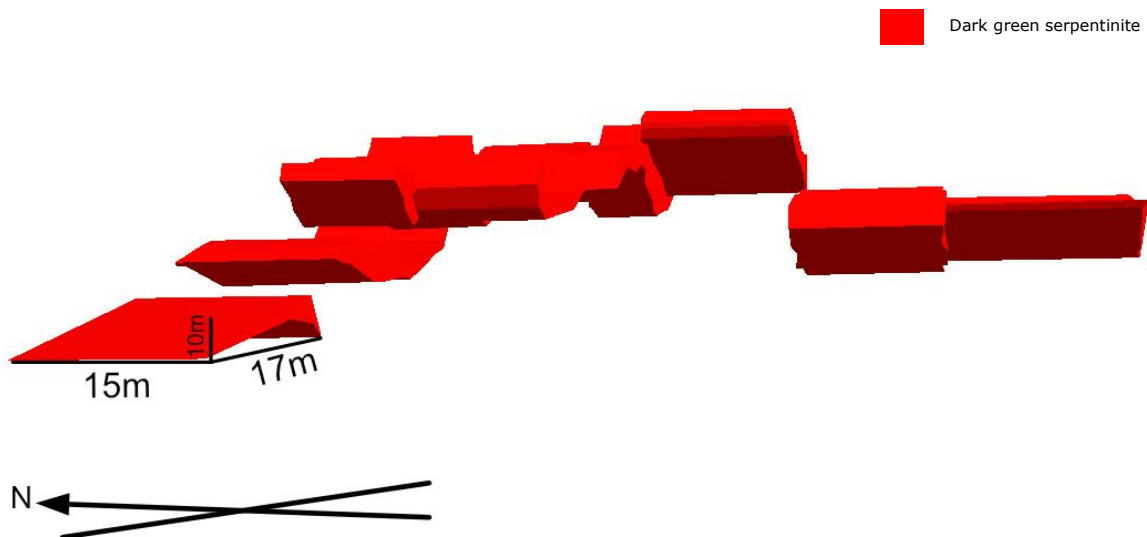
Figure 5-40: Dark green serpentinite bodies in the most-likely model. The model is seen with an inclination of -11 (seen from below) to enhance its geometry. The scale is representative of the body it is placed next to.

6 Discussion

The magnetic data indicates a significant positive anomaly coincident with the quarry at Slipsteinsberget, and a wide variety of methods have been used to explore the surface and subsurface further. The following sections discuss the magnetic petrology for this anomaly and compare Slipsteinsberget with other ultramafic bodies. Finally, a hypothesis for the formation and metamorphic evolution is proposed.

6.1 Geophysical Exploration of Slipsteinsberget

6.1.1 Magnetic Minerals
The quarry at Slipsteinsberget has a strong magnetic signal, as seen in Fig 5-27. To understand which minerals might be causing this positive anomaly, the possible magnetic minerals need to be further assessed.

Spinels are widespread as an accessory mineral within peridotites (Selbekk, 2015). Different members of the spinel group have been identified in the ultramafic rocks at Slipsteinsberget (Fig 5-25), such as minerals within the chromite-magnetite series (Mindat, 2020b), and trevorite, a strongly magnetic nickel-iron spinel (Bowles et al., 2011). Minerals of the chromite-magnetite series are found both within the brecciated serpentinite and in the dark green serpentinite, while trevorite is only observed in the soapstone. Magnetite is known to be an essential contributor to both remanent- and induced magnetization (Dentith & Mudge, 2014; Dunlop & Özdemir, 1997; Ferré et al., 2014; Michels et al., 2018), while the Cr-rich spinel behaves ferromagnetically only with a specific compositional range (Schmidbauer, 1983). According to Robbins et al. (1971) and Ferré et al. (2014), Cr-rich spinels are only magnetic if Al + Mg < 0,2 and Fe > 0,3, something that Slipsteinsberget partly contains. The soapstone also contains pyrrhotite, which also might act magnetic depending on its crystal system (Dekkers, 1988).

As magnetite is one of the products of serpentinization, magnetite was expected to be one of the magnetic minerals at Slipsteinsberget. The magnetite appears with two different morphologies: small circular grains (microcrystals) and thin layers surrounding Cr-rich spinel (zoned oxides). The microcrystals dominate in the dark green serpentinite while the zoned oxides exist in both the dark green- and the brecciated-serpentinite. The green serpentinite does not contain any significant amount of magnetite, which is consistent with its low magnetic properties.

As only a specific compositional range results in magnetic Cr-spinel, compositional calculations were conducted to see the contribution to the measured TMI from the core of the zoned oxides. Point analysis obtained in SEM indicates that 40% of the measured Cr-rich spinel in the brecciated serpentinite behaves ferromagnetically and therefore contributes to the measured TMI. The sample population obtained by point analysis in SEM is not sufficient to calculate any statistics for the Cr-rich zone in the dark green serpentinite as most of the oxides consisted of "pure" magnetite (although ferromagnetic Cr-spinels were identified).

As a result, it is reasonable to assume that magnetite is the strongest contributor to the measured TMI of the serpentinites. As not all the Cr-rich spinels are magnetic, the zoned oxides contribute less to the TMI than the microcrystals. As the brecciated serpentinite contains more zoned oxides than the dark green serpentinite, the brecciated serpentinite

is expected to have a lower TMI signal than the dark green serpentinite. This observation corresponds well to the measured values from the cylinders. Furthermore, single-domain and multidomain magnetite grains might also affect the TMI and are further discussed in subsection 6.1.2.

The occurrence of trevorite and pyrrhotite in the soapstone did not have a significant effect on the measured TMI as there is no correlation between the magnetic anomalies and the observed soapstone localities. There might be several reasons for this. First, the occurrence of trevorite and pyrrhotite minerals is minimal. Trevorite and pyrrhotite only occur as accessory minerals in altered grains, thus contributing to only a small percentage of the total mass of the rock unit. Furthermore, the pyrrhotite is only ferrimagnetic if it is monoclinic (Dekkers, 1988). As the crystal system of pyrrhotite is not known, this could also be a possible explanation for the lack of magnetic anomaly. The observed ilmenite in the chlorite slate was also evaluated as a magnetic contributor. However, as ilmenite is paramagnetic above temperatures of 57 kelvin (McEnroe et al., 2009), and no intergrowth of exsolved hematite and ilmenite was observed, the ilmenite was excluded as a contributor to the TMI of Slipsteinsberget.

Table 9 summarizes the important magnetic minerals found in the different rock units. The absence of magnetite in the green serpentinite is peculiar and will be further discussed in the formation and metamorphic evolution section (section 6.3).

Table 9: Magnetic minerals with significant magnetic importance located in microscopy

Rock Unit	Observed magnetic minerals
Dark green serpentinite	Magnetite, Zoned Cr-rich spinel and magnetite
Brecciated serpentinite	Magnetite, Zoned Cr-rich spinel and magnetite
Green serpentinite	-
Chlorite slate	Ilmenite*
Soapstone	Pyrrhotite, Trevorite

*Only important for temperatures less than 57 kelvin (Harrison & Feinberg, 2009; McEnroe et al., 2009).

6.1.2 Geophysical Analysis

When looking at the measured geophysical properties, it is evident that there is a significant disparity between the different samples. Even more so, there is also a variation between lithologies. To understand this, it is essential to link the properties to mineral content.

As seen in the susceptibility versus density plot (Fig 5-16), the samples plot with a weak positive trend. As magnetic minerals, e.g., magnetite, hemo-ilmenite, and chromite, are heavy minerals, increased content of them will lead to increased susceptibility and density, which results in a positive trend. This is the case for the brecciated and dark green serpentinite, both of which contain oxides from the magnetite-chromium-series. However, other dense, low- to nonmagnetic minerals, do exist and can explain the relatively high-density low susceptibility positioning for chlorite slate and soapstone. The occurrence of monazite, ilmenite, and apatite in the chlorite slate and the abundance of altered minerals in the soapstone may result in an increased density without any significant change in the susceptibility.

The susceptibility versus density plot (Fig 5-16) also shows a distinct grouping of the samples. Samples 3, 8, and 9 contain zoned magnetic oxides, and they plot within the same group of high susceptibility serpentinite. However, their density and oxide structure is different. Samples 3 and 9 (brecciated serpentinite) have the same density range, and both contain more chromite-rich oxides, while sample 8 (dark green serpentinite) plots with a

higher density value and contains more magnetite-rich oxides. As chromite has a lower density than magnetite (Mindat, 2020a, 2020c), this could be an explanation for their different density values. Samples 4 and 13 (green serpentinite) plot within the low-susceptibility serpentinite group together with the talc, soapstone, and garnet mica-schist, as they do not contain any magnetic minerals.

As the high susceptibility serpentinites contain ferrimagnetic minerals, the samples also plot with a high NRM value in the NRM versus density plot (Fig 5-18). However, the low susceptibility soapstone differentiates in the NRM versus density plot by having elevated NRM values. A possible explanation for the elevated remanence values might be the content of monoclinic pyrrhotite (Clark, 1997; Dekkers, 1988) and trevorite (Butler, 1972; Clark, 1997). As pyrrhotite has a lower susceptibility than magnetite (Pastore et al., 2018), this could explain why the soapstone has a high NRM value, but a lower susceptibility than the high-susceptibility serpentinites with magnetite. Besides, the pyrrhotite and trevorite occur as accessory minerals, and their magnetic signal will, therefore, not contribute very much to the total magnetic intensity.

The high NRM values observed in the brecciated- and dark green serpentinite (samples 3, 8, and 9 in Fig 5-18) might also be affected by the grain size of magnetite. According to Clark (1997), the effective upper limit for single domain (SD) magnetite behavior is extended to ~1μm and up tp ~20μm for the pseudo-single domain (PSD). The magnetite microcrystals in the brecciated- and dark green serpentinite have sizes corresponding to PSD magnetite. PSD grains could contribute to the elevated NRM values as they are strong remanence carriers (Clark, 1997). Even though no grains small enough to categorize as a SD magnetite grain were observed, there is a possibility that they exist and contribute to an even stronger NRM value.

When comparing the trendlines in the susceptibility versus density- and NRM versus density-plot (Fig 5-16 and 5-18), it is evident that the NRM versus density plot has steeper trendlines. There could be multiple possible explanations for this. First, the susceptibility range is smaller than the NRM-value range (SI-values [~0-1], NRM-values ~[0-100]), and can, therefore, lead to a difference in trendline steepness. Second, susceptibility (including paramagnetism and diamagnetism) and density are a product based on all the minerals in a rock, while NRM is only affected by the few minerals that carry remanence (Reynolds, 2011). Therefore, the addition of a small amount of, e.g., magnetite, will have a significant effect on the NRM (and on the susceptibility). However, its contribution to the density and susceptibility will be less as if it is only added to existing minerals that might already carry paramagnetic and diamagnetic minerals, resulting in a smaller total change.

When observing the calculated volume% magnetite after Clark (1997) in Fig 5-21, the plot indicates that samples 3, 8, and 9 contain elevated magnetite content, which is confirmed by thin-section microscopy. However, the results obtained by calculation are much lower compared to the results obtained from XRD and microscopy, as seen in Table 10. The empirical formula after Clark (1997) assumes an almost linear relationship between susceptibility and volume% magnetite for concentrations up to ~20%. However, the susceptibility might be affected by other minerals than magnetite. All the samples contain magnesite, which is a diamagnetic mineral (Potter et al., 2011), giving a weak negative susceptibility. Also, sample 8 contains forsterite, which is also proven to be diamagnetic (Belley et al., 2009). Consequently, these minerals may contribute to a low susceptibility resulting in an underestimate of volume% magnetite. However, the diamagnetic effects are small, and there may be other explanations, as, e.g., related to the grain size of the magnetite (Clark, 1997) or anisotropy (AMS).

Table 10: Average magnetite content obtained from three different methods.

Sample	Volume% magnetite (Clark, 1997)	XRD [%]	Microscopy [%]
3	2,08	7,37	5
8	3,35	6,23	7
9	2,80	2,65	5*

Microscopy is based on sample 2, which is taken from the same location as sample9, as there is no thin-section from sample 9.

Furthermore, samples 3 and 9, and possibly sample 8, are also the samples containing elevated AMS, as seen in Fig 5-17. An increase in AMS indicates that the samples have some statistically preferential alignment for their magnetic axes (Clark, 1997). AMS may be a result of magma flow (Knight & Walker, 1988), water flow (Mussett & Khan, 2000), strain, or crystallographic orientations (Borradaile & Henry, 1997). Samples 3, 8, and 9 came from the center of Slipsteinsberget and did not show any obvious large-scale strain indications, as could be expected along the outermost edges of Slipsteinsberget. However, there is a possibility that the magnetite preserves the water-flow direction attained during the serpentinization.

The Köenigsberger ratio, seen in Fig 5-20, has been calculated with a magnetic field of 41,6 A/m (International Geomagnetic Reference Field (IGRF) 2012-model) that corresponds to the ambient field at the sampling day. The Q-values indicate that most of the samples are dominated by induced magnetization as they plot with Q-values < 1. However, both sample 10 (soapstone) and sample 8 (dark green serpentinite) plot with Q-values between 3 and 7, indicating a remanence dominated rock. A high Q-value is a characteristic for monoclinic pyrrhotite and magnetite (Clark, 1997) and can explain their location in the diagram as samples 10 and 8 contain these minerals. Sample 4 (green serpentinite) has two cylinders with Q-values > 10, while the other four plot with Q-values < 1. The mineral content does not imply elevated NRM or susceptibility, and the two cylinders have not deviated significantly from the rest. However, there is a possibility that the sample might contain pores or small fractures filled with gases that did not escape during the water soaking before measuring, resulting in errors.

6.1.3 Geophysical Modeling

Three different models have been presented: a maximum-, minimum-, and most-likely model. As the dark green serpentinite and the soapstone have Q-values higher than 2, it was crucial to model with correct NRM directions and -intensities for the remanent dominated samples (McEnroe et al., 2009). In order to obtain models as close to reality as possible, the obtained NRM-values were used for all the bodies. Table 6 and Table 7 show the acquired average NRM directions, while Figure 5-19 shows all the measured NRM directions plotted in an equal area stereonet. Almost all of the samples have NRM directions close to the present-day field and did, therefore, not significantly affect the modeling.

For modeling, the measured surface values (dip/dip direction, susceptibility, and NRM) on the different rock units were assumed to be representative for the whole body and valid also at greater depths. This assumption is supported by measurements of drill cores taken from Slipsteinsberget that showed consistent values regardless of depth (see appendix F). However, since the magnetic anomaly from the rock units is strongest at shallower depths, as illustrated in Table 3, the models will consequently be more reliable closer to the surface.

The big difference between the three presented models is the structural orientation of the dark green serpentinite and its geometry. As they all fit the modeled anomaly and have the same petrophysical constraints, it is essential to evaluate how likely they are to form by common geological processes. The maximum volume model has a geometry resembling a teardrop or a lens with a root, while both the minimum- and most likely model do not seem to have a root system (Fig 5-35, 5-36, and 5-37). The latter seems reasonable as they represent "out-of-place" geometries compared to the surrounding garnet mica-schist. All models follow the south-western general dip direction of the garnet mica-schist. Depending on the age of Slipsteinsberget, this is a feature they might have inherited from one of the large orogenic episodes or other large-scale strain episodes, expressed by faulting (see section 6.3). When considering the dark green serpentinite, the rock unit appears with two different geometries in the models. The steep Y-shaped geometry in the maximum model indicates a complex formation event, while the more flat-lying horizon in the minimum- and most likely model suggest a simpler formation event. The Y-shaped geometry might be a result of fluid flow along fractures or the result of a faulted and highly fractured body. However, since the surrounding brecciated serpentinite does not follow the same geometry, it is unlikely that only the dark green serpentinite has this geometry, as all the other rocks at Slipsteinsberget seem to have a consistent zoned layering. The flat-lying dark green serpentinite in the other two models may indicate a uniform formation event starting from the edges of Slipsteinsberget and continuing into the core, resulting in a thin continuous olivine-rich layer in the center of the quarry. The possible formation and metamorphic evolution will be further discussed in section 6.3.

Looking at the most likely model of the serpentinites at Slipsteinsberget, the model has improved a lot compared to the previous model given by Mortenson (1973) (see Fig 6-1) and the first model of this thesis which was based only on field mapping (Fig 5-2). Mortenson (1973) did not differentiate between the different serpentinite rock-types, and the depth extent of the bodies is uncertain. As seen in the new model, the serpentinites are zoned with the dark green serpentinite in the middle. Comparing the two different models, they both have the same overall geometry with a thicker body on the western side of the quarry. The new models are flatter on top as there has been further activity on site since 1973, where Lilleberg has further removed masses of the quarry. The new most-likely model reaches a depth of 145 m a.s.l., resulting in a maximum thickness of 40m.

Furthermore, the only available volume estimate of Slipsteinsberget is the one made by Hultin (1964) with a total volume of 425 000m^3. Hultin (1964) based his calculations on elevation curves as no adequate model for the subsurface existed. Since 1964, additional

serpentinite masses have been taken out from the quarry, resulting in a smaller volume than today. The modeled volume for the serpentinites today, in the most-likely model, is ~300 000m^3, which is significantly smaller than the number attained by Hultin (1964). However, adding the chlorite-slate, soapstone, and talc slate to the estimate, the resulting number would probably be even larger than the estimate by Hultin (1964) by considering the full extent of Slipsteinsberget. Moreover, the presented model improves on the previous interpretations by including a more detailed zonation pattern, volume, and geometry.
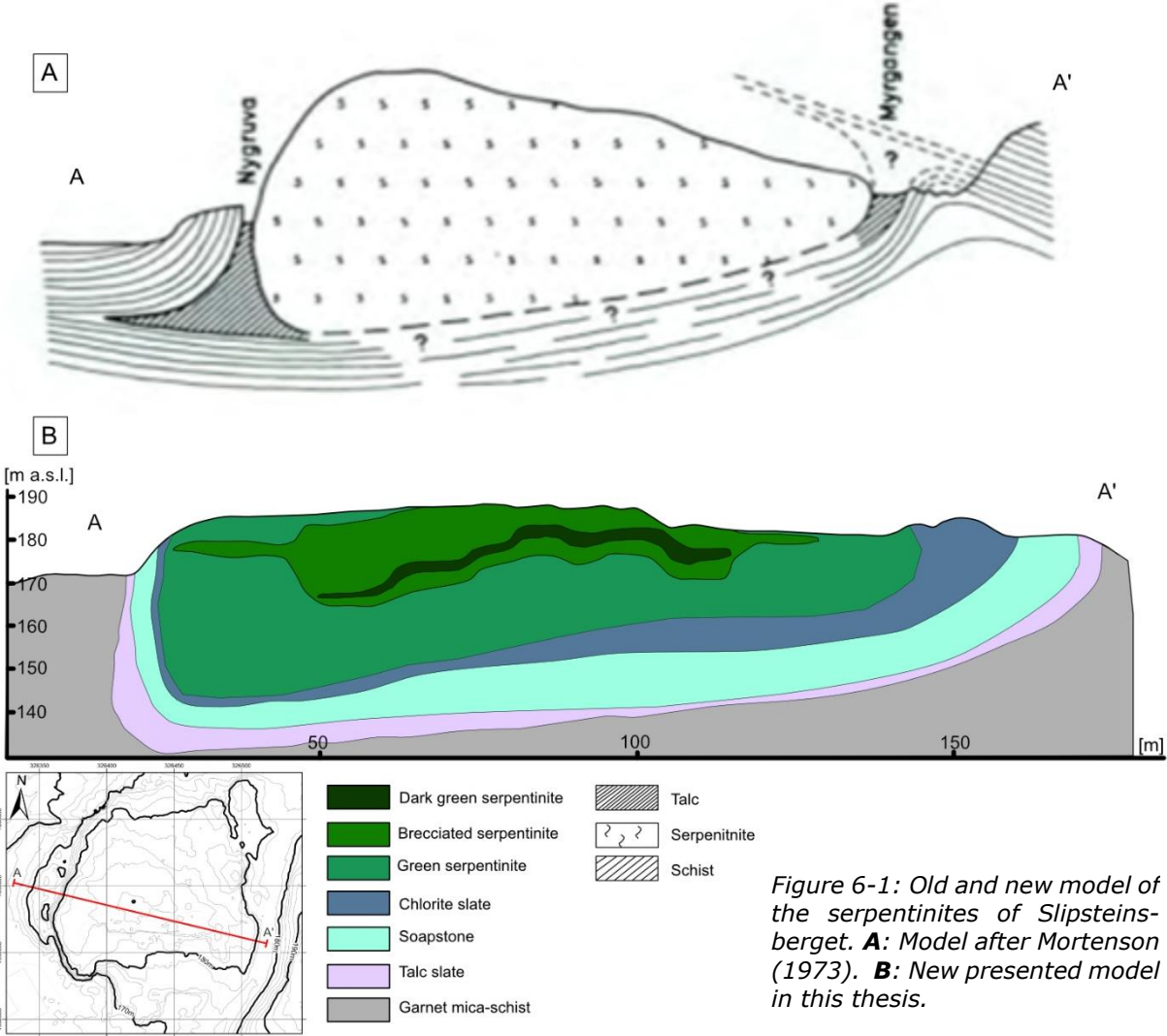
*Figure 6-1: Old and new model of the serpentinites of Slipsteinsberget. **A**: Model after Mortenson (1973). **B**: New presented model in this thesis.*

6.2 Correlation to Other Ultramafic Bodies

While studying the ultramafic rocks at Slipsteinsberget, it was useful to compare them to other ultramafic rocks referred to in the literature (Andersen et al., 2012; Jakob et al., 2017; Mortenson, 1973; Nilsson & Roberts, 2014; Roberts, 2010). Mortenson (1973) and Roberts (2010) located multiple ultramafic rocks around Sparbu, while Mortenson (1973) compared Slipsteinsberget to other similar ultramafic bodies in Norway.

6.2.1 Ultramafic Rocks at Sparbu

6.2.1.1 Geological Description

As seen in the bedrock map over Sparbu in Fig 6-2, four ultramafic bodies have been located by Mortenson (1973) and Roberts (2010). Furuberget is bigger than Slipsteinsberget, while both Bakaunberget and Smulstuen are quite small.

According to Mortenson (1973), Smulstuen is a flat-lying serpentinite that is very much altered to talc and magnesite. Its roof consists of a massive amphibolite, while the foot-wall borders to an olivine-rich gabbro. Smulstuen is also rich in chlorite. The mineral assemblage and structure in the talc-rich zone are similar to the talc-rich region at Slipsteinsberget. Furthermore, Smulstuen also contains magnetite. Bakaunberget deviates from Slip-steinsberget and Smulstuen by not being brecciated and lacks both magnesite and talc. Also, its mag-netite content is more coarse-grained compared to Slipsteinsber-get and Smulstuen. Mortenson (1973), therefore, concludes that Bakaunberget formed at a low tem-perature.

Furuberget lacks any thorough geo-logical description but is mapped as an ultramafic rock consisting of ser-pentinite and talc by Roberts (2010) in NGU's bedrock map.

6.2.1.2 Geophysical Description

When looking at the geophysical air-borne magnetic map superimposed on the bedrock map over Sparbu (both provided by NGU), it is possi-ble to compare the identified
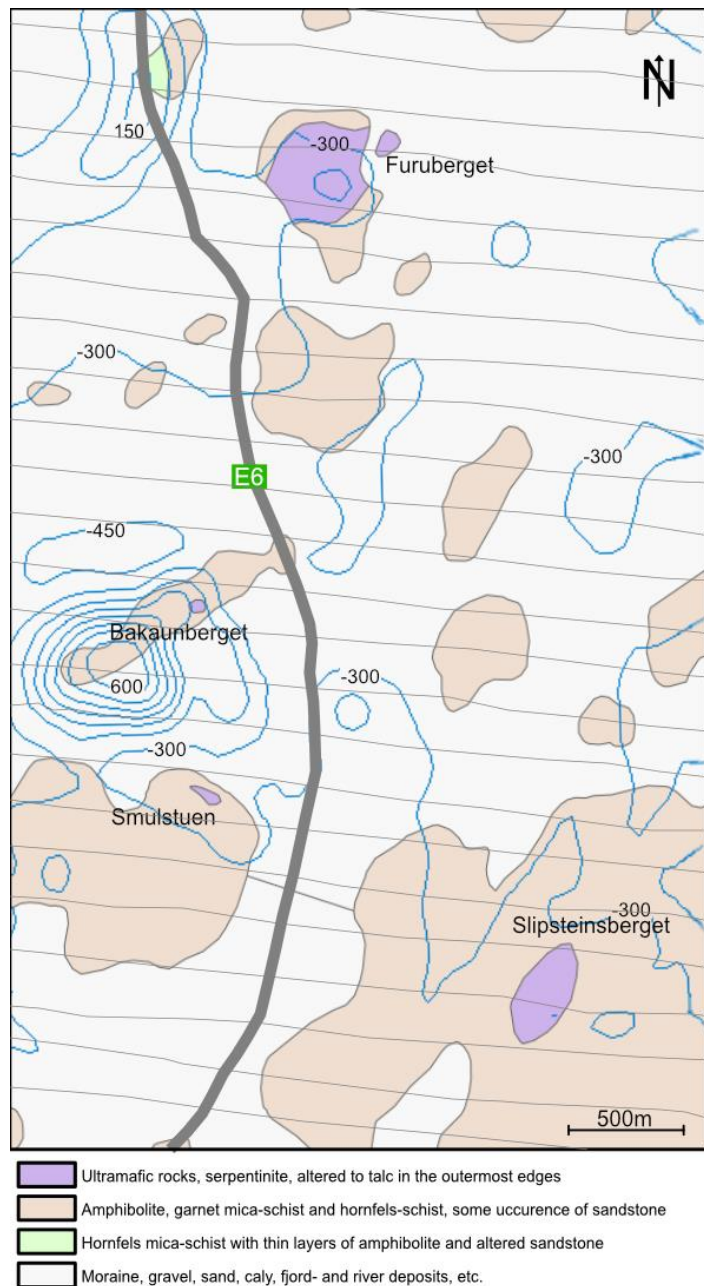
Figure 6-2: *Geological bedrock map of Sparbu area taken from ngu.no with superimposed airborne magnetic anoma-lies displayed by contours (blue lines with contour interval of 150nT). Magnetic anomalies are provided by NGU with flight line distance of 200m, marked as parallel grey lines.*

ultramafic rocks to the airborne magnetic map. As seen in Fig 6-2, there is a good corre-lation between the magnetic contours and Furuberget. The -300nT curve partly follows the outermost edges of Furuberget, and the magnetic anomaly placed above it reaches a max-imum value of -100nT in the center of Furuberget. There is no detectable correlation between the magnetic anomalies and the other three ultramafic bodies. As already seen in Fig 5-30, Slipsteinsberget's anomaly was not detected by the airborne magnetics as the flight line distance was too wide (200m, see Fig 5-30 for flight line spacing) and therefore did not capture the anomaly. As both Smulstuen and Bakaunberget also are quite small bodies, they are most likely dependent on a denser flight line spacing and a flight line crossing directly above them to be noticed on the airborne magnetics. However, as Mortenson (1973) detected magnetite in both Smulstuen and Bakaunberget, a ground magnetic survey over the two localities would most likely pick up their magnetic anomalies.

The airborne magnetic map holds two significant positive anomalies with their maximum values located approximately 500m southwest of Bakaunberget and 800m northwest of Furuberget, with magnetic values ranging between respectively -300nT to 744nT and -300nT to 195nT. As these values were obtained by an airborne magnetic survey, while Slipsteinsberget's anomaly was obtained by a ground magnetic survey, the signal from the rocks is not directly comparable as the magnetic anomaly is very much dependent on the distance (depth) from the sensor to the body, as seen in equation 13. By applying an upward continuation filter (Dentith & Mudge, 2014) on Slipsteinsberget's TMI, and then subtract the IGRF, they can be compared. After applying an upward continuation filter and subtracting the IGRF, Slipsteinsberget has a magnetic anomaly ranging from -137 to -21nT. This range corresponds to the magnetic anomaly following Furuberget. However, for a comparison to the two other positive anomalies located close to Bakaunberget and 800m northwest of Furuberget, they are significantly higher than Slipsteinsberget. This suggests that these bodies are either much larger or have a much higher magnetite content, or are due to other sources, including cultural noise. As Bakaunberget situates on the flanks of the large anomaly and is reported to contain coarse-grained magnetite, it would be very interesting to acquire a ground magnetic survey of the area to see if the outline of the ultramafic body correlates with the large anomaly. According to the owner of Slipsteins-berget (personal communication), citizens of Sparbu have found serpentinites on their properties when excavating to build houses. Consequently, there is a significant probability that there are more ultramafic bodies than already mapped in the area.

Finally, the bipolar anomaly of very small lateral extension mapped approximately 90m southwest of Slipsteinsberget, "Anomaly 2" in Fig 5-26, has a range of 47,400 to 56,000nT in the TMI map and is invisible in the upward continuation map. The 56,000nT corresponds to the value of the dark green serpentinite in Slipsteinsberget. The positive anomaly might be a fragment of these same ultramafic rocks, or a smaller magnetic object buried very close to the surface.

6.2.2 Ultramafic Rocks on a Large Scale

Both Andersen et al. (2012), Jakob et al. (2017), and Nilsson and Roberts (2014) have been studying and comparing multiple ultramafic bodies in Norway, which has contributed to a better understanding of their origins and possible relationships. Andersen et al. (2012) and Jakob et al. (2017) have studied mantle peridotites in a zone extending from southern Norway from Bergen to Røros, as marked by respectively red and orange circles in Fig 6-3. They suggest an almost continuous mélange zone originating from a hyperextended oceanic crust along the pre-Caledonian margin of Baltica. Nilsson and Roberts (2014) have combined personal fieldwork with old notebooks from the late Steinar Foslie in the 1930s and have mapped several ultramafic bodies stretching from Røros in the south to Raud-fjellet in the north along the Trøndelag-Jämtland border, marked as purple circles in Fig 6-3. They suggest that the ultramafic bodies have formed as a part of the ocean floor of an extending seaway, the Baltoscandic Sea. When working on Slipsteinsberget, Mortenson (1973) observed an apparent similarity to other well-known ultramafic bodies in Norway, such as, e.g., the serpentinite-talc deposits in Nord-Østerdal, Kvam, Sørli, and Altermark in Nordland. The ultramafic bodies in Nord-Østerdalen and Kvam are located within the study area of Andersen et al. (2012) and Jakob et al. (2017) and are marked by yellow stars together with Slipsteinsberget in Fig 6-3. Combining Andersen et al. (2012), Jakob et al. (2017), and Nilsson and Roberts (2014) work from Bergen to Raudfjellet, together with the study of large-scale faults and nappes, some interesting observations emerge.

As seen in Fig 6-3, the orange and red circles plot on an almost continuous zone stretching from Bergen to Røros. The comparable serpentinite-talc deposits to Slipsteinsberget, Nord-Østerdal and Kvam, as suggested by Mortenson (1973), are located along this zone, indicating that there might be a correlation between the mélange zone in southern Norway and Slipsteinsberget. However, the mélange zone of Andersen et al. (2012) is argued by Nilsson and Roberts (2014) to be misleading between Otta and Røros as the tectonostratigraphic positioning of these ultramafic rocks does not correlate to the rest. This claim is also supported by Corfu et al. (2014). The mélange zone is, therefore, instead believed to have an extent from Bergen to Lom. Consequently, the serpentinite-talc deposits in Nord-Østerdal and Kvam are most likely not correlated to the mélange zone in south-western Norway as they are located on the zone between Otta and Røros.

The work conducted by Nilsson and Roberts (2014) identified several small elongated lenses of partially serpentinized ultramafic rocks on the contact between the Skjøtningen Nappe and the Køli Nappe along the Trøndelag-Jämtland border (Fig 6-3). Based on regional-geological evidence, they suggested an age of latest Middle Cambrian to Early Tremadocian of the rocks. When comparing these rocks to Slipsteinsberget, they have many similarities. The small lensoidal shape of Slipsteinsberget is similar to the mapped ultramafic bodies along the Trøndelag-Jämtland border, and it is assumed to be of the same age (Mortenson, 1973; Roberts, 2010). As Slipsteinsberget is located on the Skjøt-ningen Nappe and borders to Støren Nappe in the west, which is the equivalent to the Køli Nappe in the region (NGU), this places Slipsteinsberget on a lower tectonostratigraphic position than the other located ultramafic bodies along the border. However, Nilsson and Roberts (2014) also mapped an isolated lense in the Skjøtningen Nappe in their work, thus accepting the tectonostratigraphic positioning. Additionally, the relative correlation between the mapped ultramafic bodies and Slipsteinsberget is also intriguing. As seen in Fig 6-3, the purple circles are positioned along a shear zone/fault that continues from Røros northwards to Raudfjellet, turns, and continues close to Slipsteinsberget before it ends at Steinkjær. The general foliation of the garnet mica-schist surrounding Slipsteinsberget (dip direction towards the southwest) have the same orientation as the shear zone/fault, something which strengthens the hypothesis of correlation between the ultramafic bodies along the Trøndelag-Jämtland border and Slipsteinsberget. However, the shear bands seen in Fig 5-12 indicates a dextral sence of shear towards the southeast, 90 degrees difference from

64

the foliation, something that is obscure. Since the shear bands are only located in one sample, they might be misleading. A more thorough comparison of the petrology and mineralogy of the ultramafic bodies is needed.

Figure 6-3: Locations of studied ultramafic rocks from Bergen to Raudfjellet from Andersen et al. (2012), Jakob et al. (2017), and Nilsson and Roberts (2014) superimposed on a simplified bedrock map (Bjørlykke and Olesen (2018), Corfu et al. (2014) and NGU) of southern Norway.
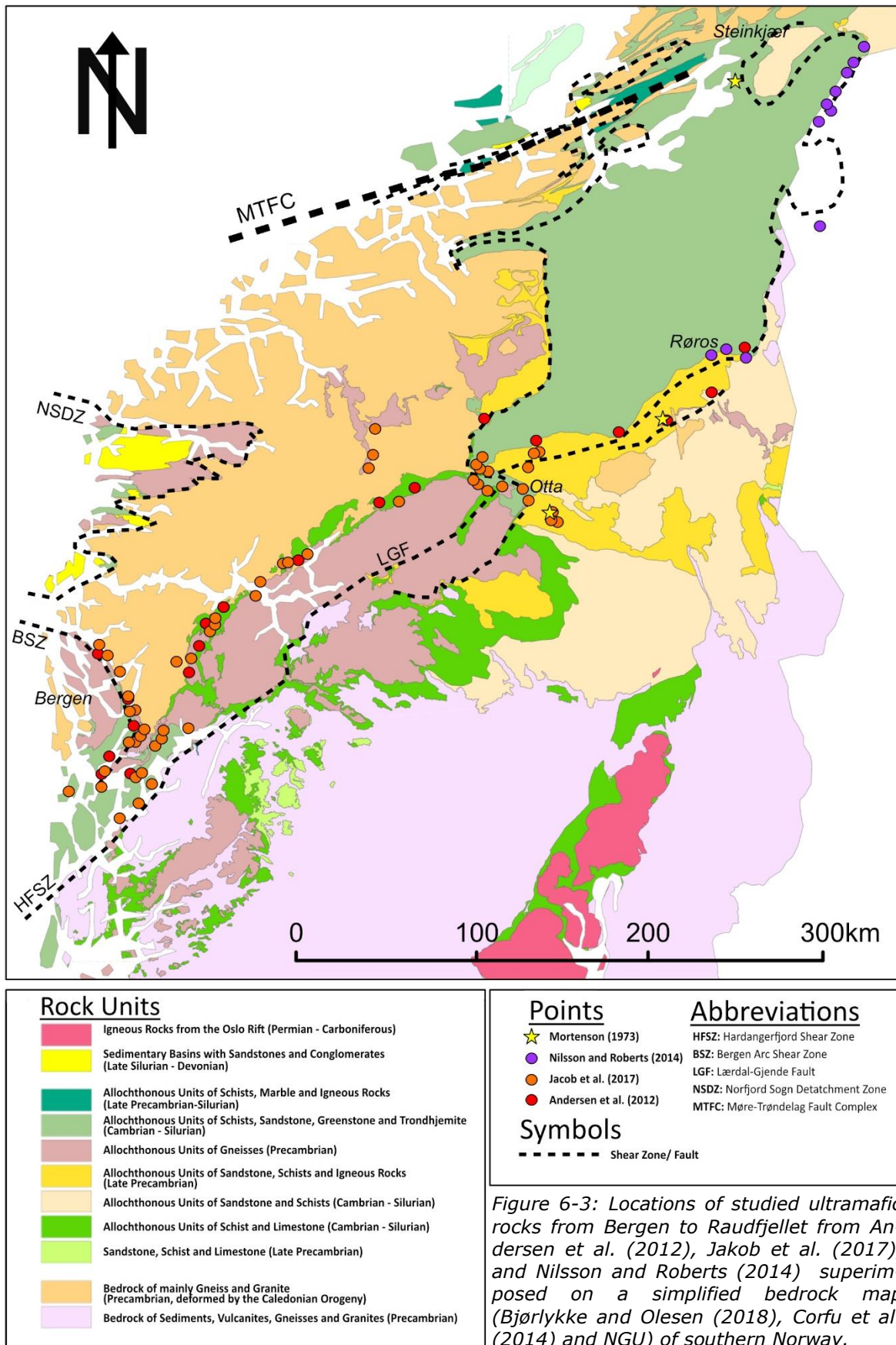
6.3 Formation and Metamorphic Evolution

As Slipsteinsberget comprises "out of place" lithologies compared to the surrounding garnet mica-schist, the metamorphic evolution is important in trying to understand the origin and formation of Slipsteinsberget. Since Slipsteinsberget shows distinct zonation patterns on multiple levels, both between rock units and within mineral grains, the zonation patterns hold vital information on its origin and history. Based on geological mapping, geophysics, mineralogical- and petrological investigations, together with comparisons to other well-known ultramafic bodies, a possible explanation for the formation and metamorphic evolution of Slipsteinsberget is presented below.

6.3.1 Metamorphic Evolution

Peridotite's main components are usually olivine, clinopyroxene, and orthopyroxene (Streckeisen, 1967). As almost none of these minerals are any longer detectable at Slipsteinsberget, it is reasonable to believe that the body has undergone metamorphism. More precisely, metamorphism and metasomatism, as serpentinization forms by hydration of MgFe-rich peridotites (Evans et al., 2013). Furthermore, its geophysical expression also indicates metamorphism, as unaltered peridotites normally are weakly magnetic (Clark, 1997). In order to understand the metamorphic evolution, whether Slipsteinsberget has experienced prograde- or retrograde metamorphism and to what extent, the mineral distribution needs to be further investigated.

A simplified mineralogical zonation of Slipsteinsberget was created for this thesis and is summarized in Fig 6-4. As ultramafic rocks correspond closely to the MgO-FeO-SiO_2 system, the mineralogy is usually relatively simple (≤ 3 principal phases in each zone) (Winter, 2014). This is also the case for Slipsteinsberget. Each zone has one primary phase comprising more than 50 volume percent of the respective zone, and two other phases. Furthermore, the zones have abrupt transitions over short distances. According to Winter (2014), zone boundaries in most metasomatically zoned ultramafic bodies are fairly abrupt, as the mineralogy changes quickly. The number of zones, and their mineralogy and thickness, depend on the nature and mobility of the fluids, as well as the stability of the minerals (Winter, 2014).
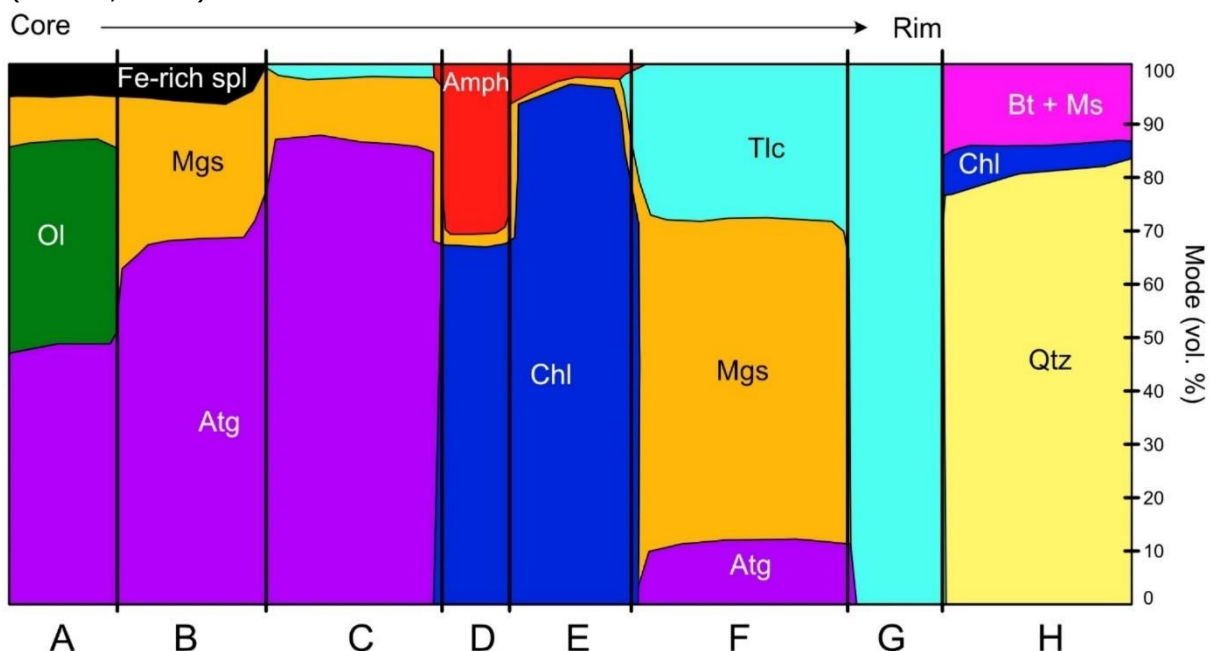
Figure 6-4: Simplified mineralogical zonation pattern over Slipsteinsberget with variation in mineral proportions. Based on XRD and microscopy. A-G: Zones from the core to rim. H: Country rock. Ol: Olivine, Atg: Antigorite, Mgs: Magnesite, Spl: Spinel, Amph: Amphibole, Chl: Chlorite, Tlc: Talc, Qtz: Quartz, Bt: Biotite, Ms: Muscovite.

The mineral zonation found throughout Slipsteinsberget (Fig 6-4) gives an indication of the metamorphic and metasomatic evolution of the ultramafic rocks. Based on petrological observations and comparisons to studies of other well-known ultramafic rocks, two possible hypotheses for the metamorphic evolution of Slipsteinsberget are discussed.

6.3.1.1 Hypothesis 1
Hypothesis 1 suggests that the different zones observed at Slipsteinsberget are a result of an increasing degree of metamorphism from the core (zone A) towards the rim (zone G), with formation under high temperatures up to ~700°C.

6.3.1.2 Hypothesis 2
Hypothesis 2 suggests that the different zones at Slipsteinsberget were formed by a combination of increasing temperatures, but also by the addition of CO_2-rich hydrothermal fluids entering through fractures in the ultramafic body. The CO_2-rich hydrothermal fluids allowed the zonation patterns observed at Slipsteinsberget to form at lower temperatures than in hypothesis 1.

Both hypotheses assume prograde metamorphism and assign the lowest degree of metamorphism to the core. The olivine and zoned spinels are crucial minerals in verifying the lowest degree of metamorphism in the core, as both hypotheses have in common. To decide on one of the hypotheses, or maybe a combination of both, the different zones and minerals need to be further investigated. The following is a brief investigation of some of the key minerals, whether they support or contradict these hypotheses.

As seen in Fig 6-4, olivine is only observed in zone A (the core). Since olivine might occur as both a primary- and a secondary mineral at different temperatures (Winter, 2014), it is a crucial mineral in understanding the metamorphic grade of the core. According to Winter (2014), secondary olivine tends to be more Mg-rich than the original peridotitic olivine. Point analysis taken in SEM (see Appendix) revealed high contents of Mg, supporting the case for secondary olivine. However, the olivine at Slipsteinsberget could also have initially been Mg-rich. Without knowing the primary Mg-content, or having another zone of olivine to compare against, the Mg-content cannot give the metamorphic grade itself. On the other hand, mineral textures obtained from microscopy, as seen in Fig 5-5, revealed olivine grains with undulose extinction, subgrain rotations, and interlobate boundaries, all pointing towards primary olivine. And hence, the lowest degree of metamorphism in the core. This is further supported by the presence of zoned spinels in zones A and B. The general zonation pattern with a small Cr-rich core that gradually changes to a Fe-rich rim, as seen in Fig 5-22, indicates that the Cr-rich phase formed first. As Cr-spinel is the primary oxide phase in peridotites (Clark et al., 1992; Ferré et al., 2014; Shive et al., 1988), as the lower end of the temperature range for spinel in peridotites is ~700°C (Facer et al., 2009), this suggests that the core has experienced the lowest degree of metamorphism and still contains some of its original minerals, such as olivine and spinel.

The zoned spinels are further investigated to understand the metamorphic evolution of the ultramafic rock. Clark et al. (1992) and Sanford (1982) suggest that serpentinization of peridotites forms secondary magnetite that may take two forms: discrete grains of nearly pure magnetite, and rims of Cr-magnetite around cores of primary Cr-spinel. Applying this observation to the spinels at Slipsteinsberget, it is compelling to believe that the Cr-rich core of the zoned spinels are primary, while the magnetite rim and the micromagneites are secondary minerals due to serpentinization. However, magnetite can also form at mantle depths without serpentinization (Ferré et al., 2013). As magnetite formed by low-temperature serpentinization will result in lower NRM-values compared to magnetite created closer to its Curie temperature (Michels et al., 2018) (585°C for magnetite (Mussett & Khan, 2000)), a large dataset of NRM-values can likely differentiate between primary and secondary magnetite if Slipsteinsberget contains both phases. Looking at the NRM

values in Fig 5-18, there are no distinct groups, but rather one almost continuous NRM range with a correlation to the density values. Since serpentinization usually leads to a density decrease and an increase in NRM values (due to the formation of secondary magnetite), this inverse correlation also indicates that the magnetite of Slipsteinsberget is secondary.

Furthermore, secondary magnetite is relatively coarse, pure, and often occurs as MD grains, giving low Q-values (Clark, 1997). As seen in Fig 5-20, the dark green serpentinite (zone A) has Q-values from 4-8, while the brecciated serpentinite (zone B) plots with Q-values <1. The Q-values in zone B suggest secondary magnetite, while the Q-values in zone A do not. However, Shive et al. (1988) claim that Q-values decrease in a fairly linear relationship with the degree of serpentinization. Therefore, since zone A has seemingly experienced the lowest degree of serpentinization, an elevated Q-value might not reject the hypothesis of secondary magnetite.

The presence of olivine and spinel supports both hypotheses and validates the assumption of the lowest degree of metamorphism in the core. However, their metamorphic evolution differs from zone C and outwards. To decide which hypothesis is most likely, the distribution of magnesite, magnetite, olivine, and talc is essential.

Since secondary magnetite is dependent on the degree of serpentinization (Clark et al., 1992), an increase in magnetite content is expected along the increasing degree of serpentinization from zones A to C. However, as seen in Fig 6-4, the magnetite is only observed in zone A and B. There could be multiple explanations for this, where the first possibility is in favor of hypothesis 2. According to Clark et al. (1992), intense carbonate-talc alteration demagnetizes serpentinites, with iron from magnetite going into carbonate instead. As Slipsteinsberget experienced a volume increase during serpentinization that resulted in the formation of fractures, especially along its edges, the newly formed fractures most likely allowed CO_2-rich hydrothermal fluids (Mortenson, 1973) to infiltrate and alter the silicates to magnesite and talc:

$$Atg + Fo + CO_2 \rightarrow Tlc + Mgs \tag{17}$$

Mortenson (1973) explains how the newly formed magnesite and talc possibly occurred as a gel mass that was driven towards the rim of the body due to the pressure created by an increasing volume. If the newly formed carbonate and talc reacted with magnetite and later got driven towards the rim, this can explain why there is no magnetite outside zone B, as the outermost edges likely experienced the highest amount of fractures and therefore also the most talc and magnesite. Another possible explanation for the distribution of magnetite, supporting hypothesis 1, could be that the peridotite was originally zoned with only a Fe-rich core, resulting in the solitary formation of magnetite in zone A and B. However, this is peculiar since peridotites are normally rich in iron.

The absence of secondary olivine is curious in hypothesis 1 as olivine can already start to form at temperatures of ~400°C (Winter, 2014). According to the equations in section 4.2, the metamorphism and corresponding temperatures of hypothesis 1 can be determined based on the mineral distribution in Fig 6-4. The abundance of antigorite, and the lack of lizardite and chrysotile, suggest that the core experienced temperatures above ~250°C (Auzende et al., 2006). Furthermore, the volume of antigorite, and hence, also the degree of serpentinization, increases from zone A to zone C, supporting the theory of increasing metamorphism towards the rim. In zone D and E, chlorite and amphibole (and possibly tremolite) appear, implying temperatures higher than ~530°C. The chlorite abundance indicates that Slipsteinsberget did not experience temperatures higher than ~700°C, as there are no signs of chlorite breakdown. Also, the breakdown of chlorite would lead to the formation of Mg and Al bearing spinels (Shive et al., 1988), something that is also not

observed. As the abundance of talc increases from zone F to G, while antigorite disappears at zone F, the limit of antigorite's stability field was most likely reached at a temperature of ~570°C where talc instead of antigorite was produced. Assuming temperatures greater than ~570°C, but lower than ~700°C, the presence of secondary olivine is expected as the serpentinite can no longer hold its water (Hirth & Guillot, 2013). Nevertheless, the absence of olivine might indicate that Slipsteinsberget did not experience temperatures higher than ~400°C, something that contradicts hypothesis 1. On the other hand, there might not have been enough available magnesium, iron, and silica to form secondary olivine. However, this is unlikely as Slipsteinsberget is rich in magnesium, and the breakup of antigorite would have provided silica, according to equation 10, 11 and 12.

The lack of secondary olivine, the restricted abundance of spinel to zone A and B, and the increase in antigorite content from zone A to C indicate that hypothesis 2 is the most likely scenario. However, the primary olivine in zone A and the increasing antigorite content towards zone C implies increasing degrees of metamorphism from zone A to C. Since the presence of CO_2-rich hydrothermal fluids is suggested by Mortenson (1973), it is possible that the zonation patterns outside zone C are created by metasomatism with selective deposition, resulting in the observed zonation patterns. According to Winter (2014), only a small amount of CO_2 will lower the stability field of antigorite and produce talc and magnesite already at lower temperatures. A similar zonation pattern is also observed by Sanford (1982) in western New England, as seen in Fig 6-5. However, the talc and carbonate minerals are still located close to the ultramafic assemblage and have not been squeezed outwards to the rim, as suggested for Slipsteinsberget.

Ultramafic Assemblage	Talc Carbonate	Talc	Ca-Amphibole Chlorite	Chlorite	Transitional Country rock	Country rock

Figure 6-5: A generalized zonation pattern of ultramafic rocks metamorphosed at greenschist to amphibolite facies with the addition of CO_2 studied by Sanford (1982). Ultramafic assemblage is typically antigorite.

A greenschist to amphibolite facies has been assigned to the zonation pattern observed by Sanford (1982) in Fig 6-5. To assign metamorphic facies to Slipsteinsberget, the stability field of the observed minerals is crucial. A minimum and maximum temperature estimate of ~250°C and ~550°C, respectively, are presented for Slipsteinsberget due to the presence of haezelwoodite (Kullerud, 1963) and antigorite. However, as secondary olivine starts to form at temperatures above ~400°C, it is reasonable to assume that the zonation pattern did not form at temperatures higher than the stability field of secondary olivine. A greenschist to amphibolite facies is indicated. According to Sanford (1982), the ultramafic assemblage is antigorite, while the Ca-amphibole is tremolite or actinolite in greenschist facies. At amphibolite facies, the ultramafic assemblage is olivine + talc, and the Ca-amphibole-chlorite zone is partly replaced by talc + anthophyllite. Therefore, the metamorphic facies at Slipsteinsberget is probably closer to the greenschist facies than the amphibolite facies. However, the presence of CO_2 affects the mineral stability fields, but due to unknown CO_2-concentrations, no improved temperature estimates can be obtained. Fig 6-6 illustrates a suggested temperature range for the formation of the observed zonation pattern at Slipsteinsberget.

```
250°C                        400°C                        550°C
|----------------------------|----------------------------|  Haezelwoodite and antigorite

|----------------------------|  No secondary olivine

|- - - - - - - - - - - - - -|  Presence of CO
```
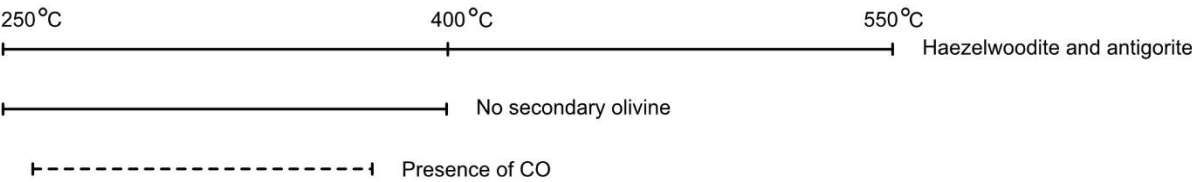
Figure 6-6: Temperature estimates of Slipsteinsberget based on mineralogy and presence of fluids

69

6.3.2 Formation

As discussed in section 4.2, multiple tectonic settings allow serpentinites to form. However, one of them is particularly interesting concerning Slipsteinsberget. Since Slipsteinsberget is a part of the Skjøtningen Nappe, which originated during the opening of the Iapetus Ocean, it is reasonable to believe that Slipsteinsberget has gone through the same sequence of formation as the Nappe itself. During the opening of the Iapetus Ocean, extensive stretching and faulting resulted in a thinning of the crust, and magma intruded the overlying thick sand deposits (Roberts, 1997). Such a tectonic setting (oceanic to continent transition, OCT) will have an exhumed mantle due to isostasy where water might penetrate, forming serpentinites (Guillot et al., 2015). Serpentinites formed in this tectonic setting lack the typical sheeted-dike complexes of an oceanic crust (Andersen et al., 2012), something that also is absent at Slipsteinsberget. It is reasonable to believe that the ultramafic body of Slipsteinsberget was formed during the opening of the Iapetus Ocean (in an OCT setting) and later obducted onto Baltica where it is located today. If Slipsteinsberget has a connection to the ultramafic bodies located by Nilsson and Roberts (2014) (shown in Fig 6-3), a formation in an OCT setting fits well, especially as Nilsson and Roberts (2014) also suggested the same tectonic setting for their ultramafic rocks along the Trøndelag-Jämtlands border. However, Nilsson and Roberts (2014) located gabbro above some of the ultramafic bodies. Gabbro is not found at Slipsteinsberget. On the other hand, Mortenson (1973) located gabbro at the footwall of Smulstuen, which is suggested to have the same origin as Slipsteinsberget. There is a possibility that Slipsteinsberget also once was connected to a gabbro and, therefore, fits the description of Nilsson and Roberts (2014).

During the "Finnmarkian" event, the Skjøtningen Nappe, along with other nappes, was thrusted upon Baltica. The thrusting created pressure and temperatures corresponding to amphibole, and possibly eclogite facies (Jakob et al., 2019), which probably affected Slipsteinsberget. However, Slipsteinsberget does not show signs of eclogite- and amphibole facies based on its mineralogy (as seen in Fig 6-6), but rather greenschist facies. Since Slipsteinsberget also experienced another lower grade metamorphic event during the Caledonian orogeny (Roberts, 1997), it is not possible to separate the respective metamorphic contribution from each event. However, the presence of monazite in the chlorite zone might give a possibility for age estimation, if dated, which can help to differentiate between the two orogenic events.

After the orogenic events, Slipsteinsberget's tectonostratigraphic positioning was probably located further down in the nappe stack due to thrusting. As serpentinites are extremely ductile (Pirajno, 2013), they might protrude along vertical faults due to density contrast, as seen in Fig 4-9. If the overlying nappes consisted of denser rocks, such as e.g. greenstones and amphibolites, Slipsteinsberget's serpentinites might have protruded into the overlying rocks as isolated "out of place" lenses. As seen in both Figs 2-2 and 6-3, Slipsteinsberget is located in short proximity to large-scale faults that might have acted as a natural pathway for Slipsteinsberget's displacement. In this tectonic setting, the chemical contrast between the country rock and the ultramafic body, and the addition of hydrothermal CO_2-rich fluids through faults and fractures, might have caused diffusion and infiltration that gradually altered Slipsteinsberget into its present-day zoned form.

Since there are no age estimations on the different metamorphic events on Slipsteinsberget, Slipsteinsberget's NRM directions have been compared to palaeomagnetic data from Norway obtained by Torsvik and Cocks (2005). Comparing the NRM directions of the serpentinites to Torsvik and Cocks (2005) work, the age of ~300Ma would give a match. However, this age does not correspond to any discussed serpentinite forming events as this is an age much younger than the discussed metamorphic events. This age estimate

could indicate that the magnetites in the serpentinites were formed after the obduction. However, it needs to be noted, that the paleomagnetic scale covers only the more recent period of the earth's history, and a similar palaeomagnetic field direction may also have occurred longer back in time.

Finally, the NRM directions of Slipsteinsberget may not represent the original NRM directions as serpentinites are extremely ductile and might have changed their geographical orientation during thrusting, protrusion, and faulting. Furthermore, when comparing the NRM direction of the highly magnetic serpentinites to the surrounding garnet mica-schist, they differ. Possible reasons for this might be that they have formed at different ages or that they even formed at the same age, but later on have experienced different movements.

7 Conclusion

In the area around Sparbu in Trøndelag county, Norway, several small lensoidal-shaped ultramafic bodies within the Skjøtningen Nappe are exposed in outcrops. Slipsteinsberget, which is well exposed within a quarry, is one of them. Published geological maps, as well as descriptions of the subsurface, are rather simple. This thesis has used a wide variety of methods to improve the understanding of Slipsteinsberget's geology, geometry, and magnetic expression, as well as its formation and metamorphic history. Possible correlations to other ultramafic bodies, both a local and regional scale, are also discussed.

Slipsteinsberget is a zoned ultramafic body dominated by an antigorite core that gradually grades to chlorite, magnesite, and talc towards the rim. The core is highly magnetic and contains up to 7% micromagnetites and zoned Cr-rich spinels. Furthermore, the serpentinites can be divided into three distinct subgroups based on their mineralogical and magnetic expression. The dark green serpentinite is located in the core and is the most magnetic rock correlating with total magnetic intensity (TMI) values between 54,700 and 55,900nT. It is enclosed by a less magnetic brecciated serpentinite with TMI values between 52,000 and 54,700nT. The outermost green serpentinite is considered non-magnetic compared to the other two serpentinites, with TMI values between 51,900 and 52,000nT. Magnetite is the main contributor to the TMI, but some iron-rich Cr-spinels, pyrrhotite, and trevorite are also observed. The volume of the magnetic part of the ultramafic body has been estimated by 3D magnetic modeling. Three possible models have been presented: a maximum, a minimum, and a most-likely model. They all follow the general foliation trend of the surrounding garnet mica-schist, which dips towards the southwest. The most-likely model has a calculated total serpentinite volume of $\sim$300 000m^3 and a maximum thickness reaching 40m on the western side of Slipsteinsberget.

Aeromagnetic data made it possible to use Slipsteinsberget as an analog to the other less studied ultramafic bodies around Sparbu. Furuberget has a similar magnetic anomaly as Slipsteinsberget, while the other two known bodies at Sparbu are not detectable on the aeromagnetic map. However, other large anomalies with magnitudes exceeding Slipsteinsberget's are present on the aeromagnetic map, which might indicate the presence of larger, unrecognized, and unmapped ultramafic bodies in the area.

Comparing Slipsteinsberget to other well-known ultramafic bodies along the Trøndelag-Jämtland border shows many resemblances: similar age, occurring as isolated lenses, and placing in a very similar tectonostratigraphic position. Furthermore, they are all located near a large-scale fault/shear zone.

Combining observations from this thesis with former work, it is reasonable to argue that Slipsteinsberget may have formed during the opening of the Iapetus Ocean in a hyperextended continental crust, similar to the ultramafic bodies along the Trøndelag-Jämtland border. The hyperextended crust resulted in an exhumed mantle that got serpentinized by the contact with water. Later on, prior to and during the genesis of the Scandinavian Caledonides, the serpentinized ultramafic body was obducted onto Baltica and protruded along faults into its present-day location. This interpretation is supported by the presence of olivine and Cr-spinels in the core of Slipsteinsberget that suggests that this is the least metamorphosed part. Finally, it is also proposed that later on, CO_2-rich hydrothermal fluids reacted with the serpentinite and formed talc and magnesite that were pushed towards the rim due to a volume increase, resulting in the present-day zonation pattern of Slipsteinsberget. Greenschist facies is suggested as the maximum degree of metamorphism.

8 Further Work

While working on Slipsteinsberget, many interesting observations were made that could have been a topic for a master thesis by themselves. The following is a list of observations that need some follow-up to better understand Slipsteinsberget and its correlation to other ultramafic bodies.

The dataset used for this master thesis is only based on 57 cylinders. Even though they revealed consistent trends, an increased number of cylinders from a larger area of Slipsteinsberget would improve the reliability and the consistency of the magnetic properties of each rock unit. The observed division of high- and low susceptibility in the field for the brecciated and dark green serpentinite was not observed in the cylinders. Maybe an increased number of cylinders could detect the observations from the field. Furthermore, an increased database of NRM values could improve the investigating of palaeomagnetism, both concerning dating and structures.

A ground magnetic survey above the located positive anomalies on the aeromagnetic map of Sparbu could improve the geological bedrock map of Sparbu and the understanding of the correlation between the ultramafic rocks. Furthermore, the already detected positive anomaly located approximately 90m southeast of Slipsteinsberget would also be very exciting to sample and model. A thorough investigation of the magnetic properties of all the ultramafic rocks at Sparbu could furthermore help in understanding their formation and metamorphic history.

In microscopy, the search for single-domain and multidomain grains could improve the understanding of the elevated magnetic properties of the dark green serpentinite. A purple isolated ~10cm nodule was also located at Slipsteinsberget but was not investigated due to its low abundance. However, Bouilhol et al. (2009) have identified a similar nodule as a chromite pod in an ultramafic body. It would be interesting to have a thin section or XRD of the nodule.

Concerning the dating of Slipsteinsberget, the identified monazites would be very interesting. Furthermore, the investigation of a suitable thermobarometry based on the mineralogy of Slipsteinsberget could also increase the knowledge of the metamorphic history of Slipsteinsberget.

To improve the understanding of how the serpentinites formed and got placed at Sparbu, a more thorough structural geological investigation is needed, especially in the surrounding garnet mica-schists, which holds a lot of structural indicators such as shear bands, foliation and pressure shadows. Furthermore, investigating the exact orientation of the Møre-Trøndelag fault complex and the large-scale fault/shear zone on the eastern side of Slipsteinsberget is needed. Chemical analysis of incompatible elements could also help in identifying a primary tectonic setting.

References

Allen, P. A., & Allen, J. R. (2005). *Basin analysis: Principles and application to petroleum play assessment* (2 ed.): John Willey and Sons.

Andersen, T. B., Corfu, F., Labrousse, L., & Osmundsen, P.-T. (2012). Evidence for hyperextension along the pre-Caledonian margin of Baltica. *Journal of the Geological Society, 169*(5), 601-612. doi:10.1144/0016-76492012-011

Auzende, A.-L., Guillot, S., Devouard, B., & Baronnet, A. (2006). Serpentinites in an Alpine convergent setting: Effects of metamorphic grade and deformation on microstructures. *European Journal of Mineralogy, 18*. doi:10.1127/0935-1221/2006/0018-0021

Belley, F., Ferré, E. C., Martín-Hernández, F., Jackson, M. J., Dyar, M. D., & Catlos, E. J. (2009). The magnetic properties of natural and synthetic (Fex, Mg1−x)2 SiO4 olivines. *Earth and Planetary Science Letters, 284*(3), 516-526. doi:https://doi.org/10.1016/j.epsl.2009.05.016

Bjørlykke, A., & Olesen, O. (2018). Caledonian deformation of the Precambrian basement in southeastern Norway. *Norwegian Journal of Geology/Norsk Geologisk Forening, 98*(4). doi:https://dx.doi.org/10.17850/njg98-4-05

Blakely, R. J., Brocher, T. M., & Wells, R. E. (2005). Subduction-zone magnetic anomalies and implications for hydrated forearc mantle. *Geology, 33*(6), 445-448. doi:10.1130/g21447.1

Bloxham, J., Zatman, S., & Dumberry, M. (2002). The origin of geomagnetic jerks. *Nature, 420*(6911), 65-68. doi:10.1038/nature01134

Bogdanova, S. V., Bingen, B., Gorbatschev, R., Kheraskova, T. N., Kozlov, V. I., Puchkov, V. N., & Volozh, Y. A. (2008). The East European Craton (Baltica) before and during the assembly of Rodinia. *Precambrian Research, 160*(1), 23-45. doi:https://doi.org/10.1016/j.precamres.2007.04.024

Borradaile, G. J., & Henry, B. (1997). Tectonic applications of magnetic susceptibility and its anisotropy. *Earth-Science Reviews, 42*(1), 49-93. doi:https://doi.org/10.1016/S0012-8252(96)00044-X

Bouilhol, P., Burg, J.-P., Bodinier, J.-L., Schmidt, M., Dawood, H., & Hussain, S. (2009). Magma and fluid percolation in arc to forearc mantle: Evidence from Sapat (Kohistan, Northern Pakistan). *Lithos, 107*, 17-37. doi:10.1016/j.lithos.2008.07.004

Bowles, J., Howie, R., Vaughan, D., & Zussman, J. (2011). *Rock-forming minerals* (2 ed.): Geological Society, London.

Butler, J. P., Beaumont, C., & Jamieson, R. A. (2015). Paradigm lost: Buoyancy thwarted by the strength of the Western Gneiss Region (ultra)high-pressure terrane, Norway. *Lithosphere, 7*(4), 379-407. doi:10.1130/l426.1

Butler, R. F. (1972). Natural remanent magnetization and thermomagnetic properties of the Allende meteorite. *Earth and Planetary Science Letters, 17*(1), 120-128.

Butler, R. F. (1992). *Paleomagnetism: magnetic domains to geologic terranes* (Vol. 319): Blackwell Scientific Publications Boston.

Clark, D. (1997). Magnetic petrophysics and magnetic petrology: Aids to geological interpretation of magnetic surveys. *AGSO journal of Australian geology & geophysics, 17*, 83-104.

Clark, D. A., French, D. H., Lackie, M. A., & Schmidt, P. W. (1992). Magnetic petrology: application of integrated rock magnetic and petrological techniques to geological interpretation of magnetic surveys. *Exploration Geophysics, 23*(2), 65-68. doi:https://doi.org/10.1071/EG992065

Coleman, R. (1971). Plate tectonic emplacement of upper mantle peridotites along continental edges. *Journal of Geophysical Research, 76*(5), 1212-1222.

Collett, B. M. (2007). Scanning electron microscopy: A review and report of research in wood science. *Wood and Fiber Science, 2*(2), 113-133.

Corfu, F., Andersen, T. B., & Gasser, D. (2014). The Scandinavian Caledonides: main features, conceptual advances and critical questions. *Geological Society, London, Special Publications, 390*(1), 9-43.

Deer, W. A., FRS, Howie, R. A., & Zussman, J. (2013). *An Introduction to the Rock-Forming Minerals*: Mineralogical Society of Great Britain and Ireland.

Dekkers, M. (1988). Magnetic properties of natural pyrrhotite Part I: Behaviour. *Physics of the Earth and Planetary Interiors, 52*, 376-393.

Dentith, M., & Mudge, S. T. (2014). *Geophysics for the mineral exploration geoscientist*: Cambridge University Press.

Dunlop, D. J., & Özdemir, Ö. (1997). *Rock magnetism: fundamentals and frontiers*: Cambridge university press.

Evans, B. W., Hattori, K., & Baronnet, A. (2013). Serpentinite: What, Why, Where? *Elements, 9*(2), 99-106. doi:10.2113/gselements.9.2.99

Facer, J., Downes, H., & Beard, A. (2009). In situ Serpentinization and Hydrous Fluid Metasomatism in Spinel Dunite Xenoliths from the Bearpaw Mountains, Montana, USA. *Journal of Petrology, 50*(8), 1443-1475. doi:10.1093/petrology/egp037

Ferré, E. C., Friedman, S. A., Martín-Hernández, F., Feinberg, J. M., Conder, J. A., & Ionov, D. A. (2013). The magnetism of mantle xenoliths and potential implications for sub-Moho magnetic sources. *Geophysical Research Letters, 40*(1), 105-110. doi:10.1029/2012gl054100

Ferré, E. C., Friedman, S. A., Martin-Hernandez, F., Feinberg, J. M., Till, J. L., Ionov, D. A., & Conder, J. A. (2014). Eight good reasons why the uppermost mantle could be magnetic. *Tectonophysics, 624*, 3-14.

Fichler, C., Odinsen, T., Rueslåtten, H., Olesen, O., Vindstad, J. E., & Wienecke, S. (2011). Crustal inhomogeneities in the Northern North Sea from potential field modeling: Inherited structure and serpentinites? *Tectonophysics, 510*(1-2), 172-185.

Fossen, H. (2000). Extensional tectonics in the Caledonides: Synorogenic or postorogenic? *Tectonics, 19*(2), 213-224.

Fossen, H., Pedersen, R.-B., Bergh, S., & Andresen, A. (2013). Creation of a mountain chain. In I. B. Ramberg, I. Bryhni, A. Nøttvedt, & K. Rangnes (Eds.), *The making of a land: Geology of Norway* (pp. 178-231). Trondheim: Norsk geologisk forening.

Gabrielsen, R. H., Odinsen, T., & Grunnaleite, I. (1999). Structuring of the Northern Viking Graben and the Møre Basin; the influence of basement structural grain, and the particular role of the Møre-Trøndelag Fault Complex. *Marine and Petroleum Geology, 16*(5), 443-465. doi:https://doi.org/10.1016/S0264-8172(99)00006-9

Gee, D. G., & Sturt, B. (1985). *The Caledonide orogen: Scandinavia and related areas* (Vol. 2): Wiley.

Geometrics (Producer). (2011). Operation manual: G-859AP Mining mag cesium magnetometer. [User manual] Retrieved from https://geometrics.com/wp-content/uploads/2018/10/859Manual-4.pdf

Gilbert, W. (1958). *De magnete*: Courier Corporation.

Grenne, T. (1988). Marginal basin type metavolcanites of the Hersjø Formation, eastern Trondheim district, central Norwegian Caledonides. *NGU bulletin, 412*, 29-42.

Guillot, S., & Hattori, K. (2013). Serpentinites: Essential Roles in Geodynamics, Arc Volcanism, Sustainable Development, and the Origin of Life. *Elements, 9*(2), 95-98. doi:10.2113/gselements.9.2.95

Guillot, S., Schwartz, S., Reynard, B., Agard, P., & Prigent, C. (2015). Tectonic significance of serpentinites. *Tectonophysics, 646*, 1-19. doi:https://doi.org/10.1016/j.tecto.2015.01.020

Harrison, R. J., & Feinberg, J. M. (2009). Mineral Magnetism: Providing New Insights into Geoscience Processes. *Elements, 5*(4), 209-215. doi:10.2113/gselements.5.4.209

Hartz, E. H., & Torsvik, T. H. (2002). Baltica upside down: A new plate tectonic model for Rodinia and the Iapetus Ocean. *Geology, 30*(3), 255-258. doi:10.1130/0091-7613(2002)030<0255:Budanp>2.0.Co;2

Hinze, W. J., Von Frese, R. R., & Saad, A. H. (2013). *Gravity and magnetic exploration: Principles, practices, and applications*: Cambridge University Press.

Hirth, G., & Guillot, S. (2013). Rheology and Tectonic Significance of Serpentinite. *Elements, 9*(2), 107-113. doi:10.2113/gselements.9.2.107

Hultin, I. (1964). Diamantboringer i talkskifer i Slipsteinsberget. *Geological survey of Norway, Report, 546*, 1-8.

Inkson, B. J. (2016). Scanning electron microscopy (SEM) and transmission electron microscopy (TEM) for materials characterization. In G. Hübschen, I. Altpeter, R. Tschuncky, & H.-G. Herrmann (Eds.), *Materials Characterization Using Nondestructive Evaluation (NDE) Methods* (pp. 17-43): Woodhead Publishing.

Jakob, J., Alsaif, M., Corfu, F., & Andersen, T. B. (2017). Age and origin of thin discontinuous gneiss sheets in the distal domain of the magma-poor hyperextended pre-Caledonian margin of Baltica, southern Norway. *Journal of the Geological Society, 174*(3), 557-571. doi:10.1144/jgs2016-049

Jakob, J., Andersen, T. B., & Kjøll, H. J. (2019). A review and reinterpretation of the architecture of the South and South-Central Scandinavian Caledonides—A magma-poor to magma-rich transition and the significance of the reactivation of rift inherited structures. *Earth-Science Reviews, 192*, 513-528.

Knight, M. D., & Walker, G. P. L. (1988). Magma flow directions in dikes of the Koolau Complex, Oahu, determined from magnetic fabric studies. *Journal of Geophysical Research: Solid Earth, 93*(B5), 4301-4319. doi:10.1029/JB093iB05p04301

Kullerud, G. (1963). Thermal stability of pentlandite. *The Canadian Mineralogist, 7*(3), 353-366.

Ladenberger, A., Be'eri-Shlevin, Y., Claesson, S., Gee, D. G., Majka, J., & Romanova, I. V. (2014). Tectonometamorphic evolution of the Åreskutan Nappe–Caledonian history revealed by SIMS U–Pb zircon geochronology. *Geological Society, London, Special Publications, 390*(1), 337-368.

Li, Z. X., Bogdanova, S. V., Collins, A. S., Davidson, A., De Waele, B., Ernst, R. E., . . . Vernikovsky, V. (2008). Assembly, configuration, and break-up history of Rodinia: A synthesis. *Precambrian Research, 160*(1), 179-210. doi:https://doi.org/10.1016/j.precamres.2007.04.021

Luo, Q. (2018). Electron Microscopy and Spectroscopy in the Analysis of Friction and Wear Mechanisms. *Lubricants, 6*(3), 58.

McEnroe, S. A., Fabian, K., Robinson, P., Gaina, C., & Brown, L. L. (2009). Crustal Magnetism, Lamellar Magnetism and Rocks That Remember. *Elements, 5*(4), 241-246. doi:10.2113/gselements.5.4.241

McEnroe, S. A., Harrison, R. J., Robinson, P., & Langenhorst, F. (2002). Nanoscale haematite–ilmenite lamellae in massive ilmenite rock: an example of 'lamellar magnetism' with implications for planetary magnetic anomalies. *Geophysical Journal International, 151*(3), 890-912. doi:10.1046/j.1365-246X.2002.01813.x

Merrill, R., McElhinny, M., & McFadden, P. L. (1996). *The magnetic field of the earth: paleomagnetism, the core, and the deep mantle* (Vol. 63). International geophysics series: Academic Press.

Michels, A., McEnroe, S., & Fichler, C. (2018). Geophysical expression of the Leka Ophiolite, Norway modeled from integrated gravity, magnetic and petrophysical data.

Mindat. (2020a). Chromite. Retrieved from https://www.mindat.org/min-1036.html

Mindat. (2020b). Chromite-Magnetite Series. Retrieved from https://www.mindat.org/min-43495.html

Mindat. (2020c). Magnetite. Retrieved from https://www.mindat.org/min-2538.html

Mortenson, M. (1973). Talc - serpentinite deposits at Sparbu, Nord-Trøndelag. *Geological survey of Norway, Skrifter, 290*(4), 1-16.

Mussett, A. E., & Khan, M. A. (2000). *Looking into the earth: an introduction to geological geophysics*: Cambridge University Press.

Nasuti, A., Pascal, C., & Ebbing, J. (2012). Onshore–offshore potential field analysis of the Møre–Trøndelag Fault Complex and adjacent structures of Mid Norway. *Tectonophysics, 518-521*, 17-28. doi:https://doi.org/10.1016/j.tecto.2011.11.003

Nesse, W. D. (2012). *Introduction to mineralogy*.

NGU. Database for geologiske enheter, Størensdekket. Retrieved from http://aps.ngu.no/pls/utf8/geoenhet_SokiDb.Vis_enhet?p_id=147615&p_spraak=N. Genino Retrieved 26.01.2020, from NGU http://aps.ngu.no/pls/utf8/geoenhet_SokiDb.Vis_enhet?p_id=147615&p_spraak=N

Nilsson, L. P., Kero, L., Johansson, R., Roberts, D., & Mogaard, J. O. (2014). Geophysical expression of the Raudfjellet ophiolite, Nord-Trøndelag, central Norwegian Caledonides. *Geological survey of Norway Bulletin, 453*, 13-27.

Nilsson, L. P., & Roberts, D. (2014). A trail of ophiolitic debris and its detritus along the Trøndelag-Jämtland border: correlations and palaeogeographical implications. *Geological survey of Norway Bulletin, 453*, 29-41.

Nilsson, L. P., Roberts, D., & Ramsay, D. M. (2005). The Raudfjellet ophiolite fragment, Central Norwegian Caledonides: principal lithological and structural features. *Geological survey of Norway Bulletin, 445*, 101.

Nordgulen, Ø., & Andresen, A. (2013). The Precambrian. In I. B. Ramberg, I. Bryhni, A. Nøttvedt, & K. Rangnes (Eds.), *The making of a land: Feology of Norway* (pp. 62-119). Trondheim: Norsk geologisk forening.

Nystuen, J. P. (2013). Break-up of the Cambrian continent. In I. B. Ramberg, I. Bryhni, A. Nøttvedt, & K. Rangnes (Eds.), *The making of a land: Geology of Norway* (pp. 120-147). Trondheim: Norsk geologisk forening.

Osmundsen, P. T., Eide, E. A., Haabesland, N. E., Roberts, D., Andersen, T. B., Kendrick, M., . . . Redfield, T. F. (2006). Kinematics of the Høybakken detachment zone and the Møre–Trøndelag Fault Complex, central Norway. *Journal of the Geological Society, 163*(2), 303-318. doi:10.1144/0016-764904-129

Passchier, C. W., & Trouw, R. A. (2005). *Microtectonics*: Springer Science & Business Media.

Pastore, Z., Fichler, C., & McEnroe, S. (2018). Magnetic anomalies of the mafic/ultramafic Seiland Igneous Province.

Pirajno, F. (2013). Effects of metasomatism on mineral systems and their host rocks: alkali metasomatism, skarns, greisens, tourmalinites, rodingites, black-wall alteration and listvenites. In *Metasomatism and the Chemical Transformation of Rock* (pp. 203-251): Springer.

Potter, D. K., Al-Ghamdi, T. M., & Ivakhnenko, O. P. (2011). Sensitive carbonate reservoir rock characterization from magnetic hysteresis curves and correlation with petrophysical properties. *Petrophysics, 52*(01), 50-57.

Rey, P., Burg, J.-P., & Casey, M. (1997). The Scandinavian Caledonides and their relationship to the Variscan belt. *Geological Society, London, Special Publications, 121*(1), 179-200. doi:10.1144/gsl.Sp.1997.121.01.08

Reynolds, J. M. (2011). *An introduction to applied and environmental geophysics*: John Wiley & Sons.

Robbins, M., Wertheim, G. K., Sherwood, R. C., & Buchanan, D. N. E. (1971). Magnetic properties and site distributions in the system FeCr2O4-Fe3O4(Fe2+Cr2−xFex3+O4. *Journal of Physics and Chemistry of Solids, 32*(3), 717-729. doi:https://doi.org/10.1016/S0022-3697(71)80412-2

Roberts, D. (Cartographer). (1997). Geological bedrock map Grong, M 1: 250,000, Geological Survey of Norway

Roberts, D. (Cartographer). (2010). Geological bedrock map Stiklestad 1722 IV, M 1:50000, preliminary edition, Geological Survey of Norway

Roberts, D., & Wolff, F. C. (1981). Tectonostratigraphic development of the Trondheim region Caledonides, Central Norway. *Journal of Structural Geology, 3*(4), 487-494. doi:https://doi.org/10.1016/0191-8141(81)90048-1

Sanford, R. F. (1982). Growth of ultramafic reaction zones in greenschist to amphibolite facies metamorphism. *American Journal of Science, 282*(5), 543-616.

Saumur, B.-M., Hattori, K. H., & Guillot, S. (2010). Contrasting origins of serpentinites in a subduction complex, northern Dominican Republic. *GSA Bulletin, 122*(1-2), 292-304. doi:10.1130/b26530.1

Schmidbauer, E. (1983). Magnetization of Fe-Cr-Ti spinels. *Physics and Chemistry of Minerals, 9*(3), 124-126. doi:10.1007/BF00308368

Selbekk, R. S. (2015). *Minerals of Norway* (2 ed.): Geological Survey of Norway.

Seranne, M. (1992). Late Paleozoic kinematics of the Møre-Trøndelag Fault Zone and adjacent areas, central Norway. *Norsk Geologisk Tidsskrift, 72*, 141-158.

Shive, P. N., Frost, B. R., & Peretti, A. (1988). The magnetic properties of metaperidotitic rocks as a function of metamorphic grade: implications for crustal magnetic anomalies. *Journal of Geophysical Research: Solid Earth, 93*(B10), 12187-12195.

Slagstad, T., Roberts, N., & Kulakov, E. (2017). Linking orogenesis across a supercontinent; the Grenvillian and Sveconorwegian margins on Rodinia. *Gondwana Research, 44*, 109-115. doi:10.1016/j.gr.2016.12.007

StatisGeo (Producer). (n.d.). User manual: Kappameter KM-7 magnetic susceptibility meter. [User Manual] Retrieved from http://www.satisgeo.com/PDF/KM-7.pdf

Storemyr, P. (2015). The medieval quarries at Sparbu: A Central Norwegian 'little sister'of the Purbeck quarry landscape in England. *Exploitation of Outfield resources–Joint research at the University Museums of Norway, Skrifter*(32), 141-154.

Storemyr, P., & Heldal, T. (2002). Soapstone production through Norwegian history: geology, properties, quarrying and use. *ASMOSIA, 5*, 359-369.

Streckeisen, A. L. (1967). Classification and nomenclature of igneous rockes. *Neues Jahrbuch fur Mineralogie Abhandlungen, 107*, 144-240.

Tegner, C., Andersen, T. B., Kjøll, H. J., Brown, E. L., Hagen-Peter, G., Corfu, F., . . . Torsvik, T. H. (2019). A mantle plume origin for the Scandinavian Dyke Complex: a "piercing point" for 615 Ma plate reconstruction of Baltica? *Geochemistry, Geophysics, Geosystems, 20*(2), 1075-1094.

Torsvik, T. H., & Cocks, L. R. M. (2005). Norway in space and time: A Centennial cavalcade. *Norwegian Journal of Geology/Norsk Geologisk Forening, 85*.

Winter, J. D. (2014). *Principles of igneous and metamorphic petrology* (Second edition ed.): Pearson Education Limited.

Wolff, F. (Cartographer). (1976). Bedrock map, Trondheim. Scale, 1: 250 000

Østerås, B. (2017). Slipsteinberget Soapstone Vessel Quarry. Home Production or Professional Craft? *University of Bergen Archaeological Series, 9*, 153-163.

9 Appendices

Appendix A – Mineral Abbreviations

Abbreviations	Mineral
Amph	Amphibole
Atg	Antigorite
Bt	Biotite
Chl	Chlorite
Grt	Garnet
Hzl	Haezelwoodite
M	Mackinawite
Mgs	Magnesite
Ms	Muscovite
Mt	Magnetite
Ol	Olivine
Po	Pyrrhotite
Qtz	Quartz
Spl	Spinel
Tlc	Talc
Trv	Trevorite

Appendix B – Microscopy

Sample ET.4.nr1	Rock name: Serpentinite
Field description	Melanocratic, aphanitic green serpentinite. Have cm-scale areas with darker and lighter green-color that resembles a grain. Contain less than 1% fine-grained dark minerals. Very light and soft erosional surface.
Major phases	95% antigorite, 5% (~4% talc and ~1% magnesite)
Minor phases	Opaque minerals: very white, pale yellow and grey
The overall shape of grain aggregates	Xenoblastic, seriate-interlobate
Microstructures and textures	The magnesite and talc appear together. The talc dominates and has developed grains with cleavage. The serpentinite takes two different forms: blade-like, which is the lighter areas on the thins section, and a smaller needle-like form that look browner in ppl and darker in xpl. Traces of old altered grains appear brown in ppl-
XRD	71% antigorite, 13% olivine, 7% lizardite, 6%talc, 2% chrysotile, less than 1% magnetite

Sample: ET.4.nr2	Rock name: Serpentinite
Field description	An area containing nodules or big clasts (3cm-1m) with a melanocratic rim and a leucocratic interior. The rim is thin (up to 5cm). The interior is light brown (corroded magnesite?) and typically has dark, chaotic thin veins penetrating it. A groundmass of green to black serpentinite with magnesite veins is hosting the clasts. The rock is predominantly aphanitic but has zones of darker and greener serpentinite. Overall, both the groundmass and clasts contain black phaneritic grains up to 2mm in size (almost porphyritic). The dark grains are evenly distributed throughout the rock.
Major phases	70% antigorite, 20% magnesite and 7% opaque minerals (5% magnetite + 2% chromite)
Minor phases	Sulfides (and something around the magnetite)
The overall shape of grain aggregates	Xenoblastic, seriate-interlobate
Microstructures and textures	Felsitic texture. Some of the magnesite is oriented parallel to the contact between the rim and the interior, and some are randomly oriented. The antigorite appears in a blade-like structure and small thin needles. The magnetite is surrounded by a rim of another darker mineral and is sometimes zoned. The magnetite appears inequigranular.
XRD results	51% antigorite, 36% magnesite, 10% magnetite, 2% lizardite, less than 1% chrysotile + quartz

Sample: ET.4.nr3	Rock name: Serpentinite
Field description	Looks like the "groundmass" in sample 2, but with much darker grains (5-10%?). Aphanitic and melano-cratic serpentinite with up to 2mm dark grains equally distributed throughout the sample. It contains magnesite veins.
Major phases	80% Antigorite, ,10% magnesite 7% oxides (5% magnetite + 3% chromite)
Minor phases	Sulfides
The overall shape of grain aggregates	Xenoblastic, seriate-interlobate
Microstructures and textures	Felsitic texture. The magnesite is sometimes altered to magnetite. The magnetite has zonation and a thin darker mineral edging it. The magnesite mostly accumulates in the veins, but also randomly throughout the specimen. Needle-like texture for the serpentinite. The magnetite is randomly distributed, circular, and up to 2mm in size.
XRD results	80% antigorite, 8% magnesite, 7% magnetite, 4% lizardite, less than 1% chrysotile

Sample ET.4.nr4	Sample name: Serpentinite
Field description	Leucocratic, fine-grained, green serpentinite. Much more light green compared to the rest of the serpen-tinites. Lack of "typical" black areas. The serpentinite is mostly aphanitic but contains some small (up to 1mm) black grains evenly distributed throughout the sample. Some areas are almost entirely white.
Major phases	80% Antigorite, 20% magnesite
Minor phases	Opaque minerals: sulfides and oxides
The overall shape of grain aggregates	Xenoblastic seriate-interlobate
Microstructures and textures	Foliated with discontinuous layers of magnesite and serpentine. The serpentine occurs as bigger blade-like and needle-like textures. The opaque minerals are mostly associated with the magnesite.
XRD	73% antigorite, 23% magnesite, 2% lizardite and 2% chrysotile

Sample ET.4.nr5	Rock name: Chlorite slate + amph
Field description	Groundmass of aphanitic chlorite with phaneritic, radial, acicular, white amphibole up to 1cm in size. They intergrow and appears to overtake the chlorite. Magnesite appears as cubes just 2 m away.
Major phases	55% Chlorite, 40% Amphibole (tremolite?), 5% Talc
Minor phases	Opaque minerals
The overall shape of grain aggregates	Amphibole is hypidioblastic, but overall the thin section is xenoblastic.
Microstructures and textures	Groundmass of brown/green chlorite. Acicular radial amphibole (up to 6mm) + small prismatic amphibole (0,08mm) with clear 120 angle cleavage. The amphibole had grains of 1 order yellow, and some have 2order yellow. The thin section has some outfall.
XRD	64% Chlorite, 23% amphibole, 7% talc, 2,5% feldspar, 2% Siderite, 1% magnesite

Sample ET.4.nr6	Rock name: Chlorite slate
Field description	Melanocratic, aphanitic foliated chlorite. Predominantly chlorite but contains rhombohedral (up to 5mm) magnesite grains. The rhombohedral magnesite seems to be out of equilibrium as they erode, leaving empty holes in the rock.
Major phases	Chlorite 90%, magnesite 10%
Minor phases	Two different oxides, small prismatic grains in magnesite, epidote
The overall shape of grain aggregates	Hypidioblastic, seriate-interlobatic
Microstructures and textures	Groundmass of a foliated cryptocrystalline chlorite with two euhedral magnesite (5mm) grains. Small epidote grains (0,1mm) with a blue halo (corona/depletion halo?) is found throughout the chlorite groundmass, possible zoisite. Bigger chlorite veins (2mm thick) penetrate through the chlorite groundmass. The vein contains bladed chlorite grains, and big oxides are accumulated here. The whole thin section contains small (mm) oxide grains that are situated within grains and on grain boundaries.
XRD	96% chlorite, 3% dolomite, less than 1% magnesite and magnetite

Sample ET.4.nr7	Rock name: Schistose chlorite rich meta-ultramafic-rock
Field description	A melanocratic, equigranular, aphanitic massive rock consisting of predominantly chlorite. It contains chaotic veins of a shiny flakey mineral (feldspar?!). Occurs over a small area between the serpentinite and the chlorite-rich zone to the east in the quarry.
Major phases	50% Chlorite, 35% Feldspar (plagioclase), 15% amphibole (tremolite?)
Minor phases	Oxides (almost nothing)
The overall shape of grain aggregates	Xenoblastic, seriate-amoeboid
Microstructures and textures	Groundmass of foliated cryptocrystalline chlorite with veins of feldspar and needle-like amphiboles. One vein contains shape and crystallographic oriented feldspar with pressure solutions oriented parallel to foliation in chlorite, while the other veins have randomly oriented feldspar. The feldspar has lamella and good cleavage. Amphiboles occur as randomly distributed needles and bigger grains (2mm) with two good cleavages with 120 degrees angle. Some of the oxides are corroded in groups together with amphiboles. Foliated rock.
XRD	95% Chlorite, 4% Hornblende

Sample ET.3.nr8	Rock name: Serpentinite
Field description	Melanocratic (darkest rock in the master thesis), aphanitic equigranular rock. Have some lighter areas and some darker in a flow-like texture. Contains veins with an oriented crystal growth perpendicular to the vein. The vein contains a dark and a light mineral. It contains small (less than 1mm) dark, semi-shiny grains.
Major phases	45% serpentine, 30% olivine, 18% magnesite 7% magnetite
Minor phases	Opaque minerals: mostly oxides with some sulfides
The overall shape of grain aggregates	Xenoblastic/allotriomorphic seriate-interlobate
Microstructures and textures	The thin section is divided into areas consisting of serpentine with needle-blade texture and olivine and magnesite rich areas. The olivine (up to 600 micrometers) is equigranular and cracked, have undulose extinction, subgrain rotations, and interlobate boundaries. Magnesite (up to 2mm) occur both together with olivine and in veins. The veins have grain-oriented minerals and contain opaque minerals. The opaque minerals can be divided into bigger grains (1-2mm) and smaller grains (20-155 micrometers). Poikilitic olivine-chromite cumulate?
XRD	48% Antigorite, 35% olivine, 8% magnesite, 6% magnetite, 3% lizardite

83

Sample KL.nr10	Rock name: Soapstone
Field description	Leucocratic, equigranular fine-grained rock. It contains white, light-grey, black, and yellow-brown grains. The black and yellow-brown grains are phaneritic, while the others are aphanitic. Black grains are less than 1%.
Major phases	35% talc, 55% magnesite, 10% serpentine
Minor phases	Opaque minerals: a light oxide with veins of darker oxide chromite?
The overall shape of grain aggregates	Xenoblastic seriate-interlobate
Microstructures and textures	Groundmass of "dusty" talc with bigger carbonate grains (up to 2mm) and big talc grains (2mm). The big talc grains have a good cleavage. The opaque minerals and the serpentine avoid forming in the big talc grains or the opposite. The serpentinite and oxides overlap both the groundmass and the calcite. The serpentinite has a needle-like texture.
XRD	34% Magnesite, 29% Talc, 24% dolomite, 12% antigorite

Sample GL.nr11	Rock name: Garnet mica schist
Field description	Foliated, leucocratic, inequigranular rock with an overall aphanitic texture. The garnets are red, easily spotted, and vary in size from 1mm up to almost 1 cm (phorphorytic?). The foliation is made up of layers of mica, quartz, and a darker fine-grained mineral. Foliation has a general trend of 30-60 degrees dip towards SW. The rock shows a C'-type shear bands, indicating dextral shear sense (towards the SW).
Major phases	80% Quartz, 10% muscovite, 7% biotite 3% garnet
Minor phases	Chlorite, Feldspar, Oxides
The overall shape of grain aggregates	Hypidioblastic inequigranular-interlobate
Microstructures and textures	Foliated with mm thick layers of small quartz grains (50-200micrometer), bigger quartz grains (up to 2mm), and muscovite. The layers are stacked and folded. Garnets (up to 2mm) only occur in the quartz layers, while muscovite occurs in all layers. Lepidoblastic texture for micas. Pressure solutions and subgrain rotation in the quartz grains. The garnets show randomly oriented poikilitic texture and pressure shadows. It has chlorite and mica grains wrapped around it (porphyroblast) with some min.
XRD	75% quartz, 12% muscovite, 7% albite, 2% biotite 2% chlorite, 1% alamdine

Sample ET.4.nr12	Rock name: Chlorite slate
Field description	Melanocratic foliated chlorite slate. Have a groundmass of chlorite with many small (less than 1mm) black minerals. The samples contain some chaotic white veins that occasionally holds up to 2mm big metallic grains. The sample is very soft. Easily scratched with a knife. No magnesite grains.
Major phases	60% Chlorite, 20% (Opx)pyroxene(?), 20% oxides
Minor phases	Ca-Pyroxene/talc/epidote (parallel utslokning med kløv, 3.ordens grønn, høyt positivt rieleff)
The overall shape of grain aggregates	Xenoblastic seriate-interlobate
Microstructures and textures	Lepidoblastic groundmass of chlorite and oxides. Green depletion halo/reaction rim around the talc/epidote/pyroxene that is in contact with the chlorite. The chlorite occurs as a fine-grained mass without any distinct grains and occasionally as bigger crystals (up to 0,75mm). The oxides are oriented along the foliation of the groundmass. The pyroxenes are accumulated in two veins parallel to the foliation with big oxides.
XRD	65% Chlorite, 9% Ilmenite, 2%Hematite, 6% Bornite, 10% Talc, 4% epidote, 2% Hematite, 2% diopside

Sample: ET.3.nr13	Rock name: Serpentinite
Field description	Massive, aphanitic, green to black serpentinite. Looks like the groundmass in sample 3, but without the black grains (mostly green, but with some dark-green areas. White magnesite veins penetrating it.) Have a chaotic flow-like texture.
Major phases	95% antigorite, 5% (~3% magnesite and ~2% talc)
Minor phases	Sulfides and oxides
The overall shape of grain aggregates	Xenoblastic seriate-interlobate
Microstructures and textures	The magnesite and talc appear together. The serpentinite takes two different forms: blade-like, which is the lighter areas on the thins section, and a smaller needle-like form that look browner in ppl and darker in xpl.
XRD	91% antigorite, 4% lizardite, 5% talc

Appendix C – Geophysical Measurements

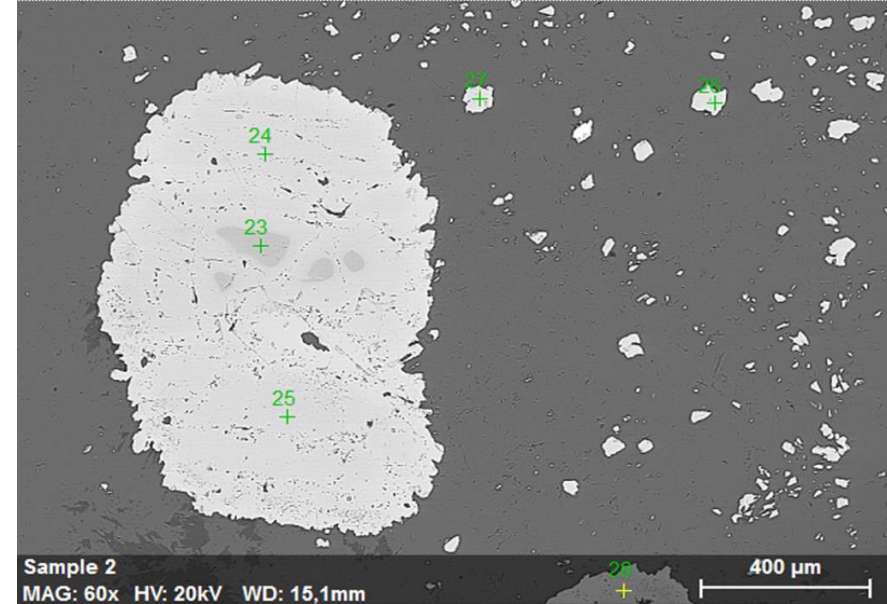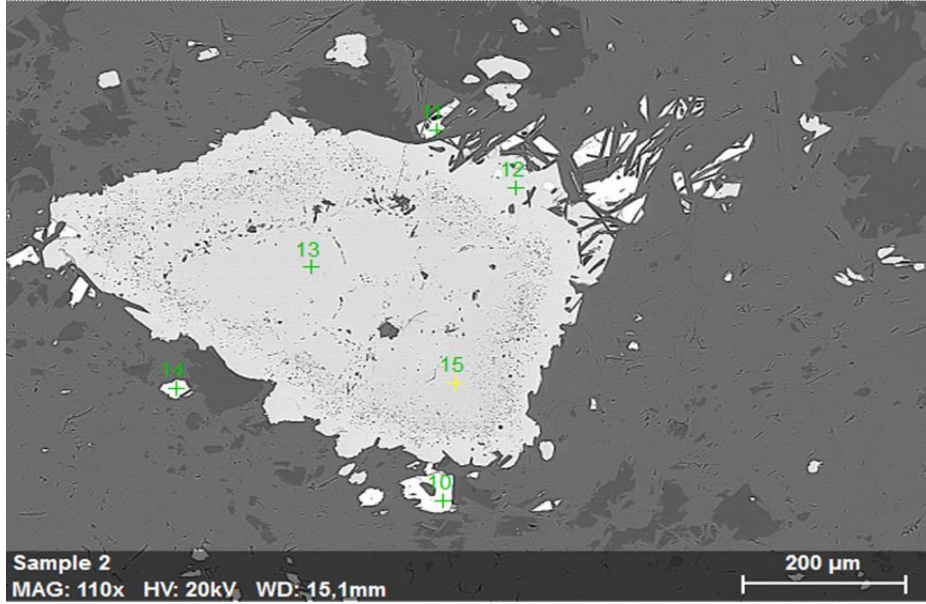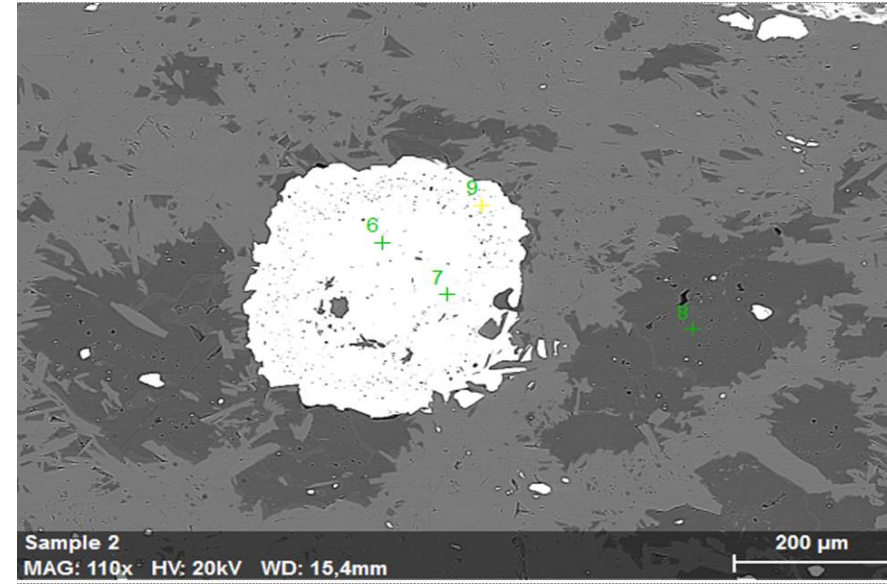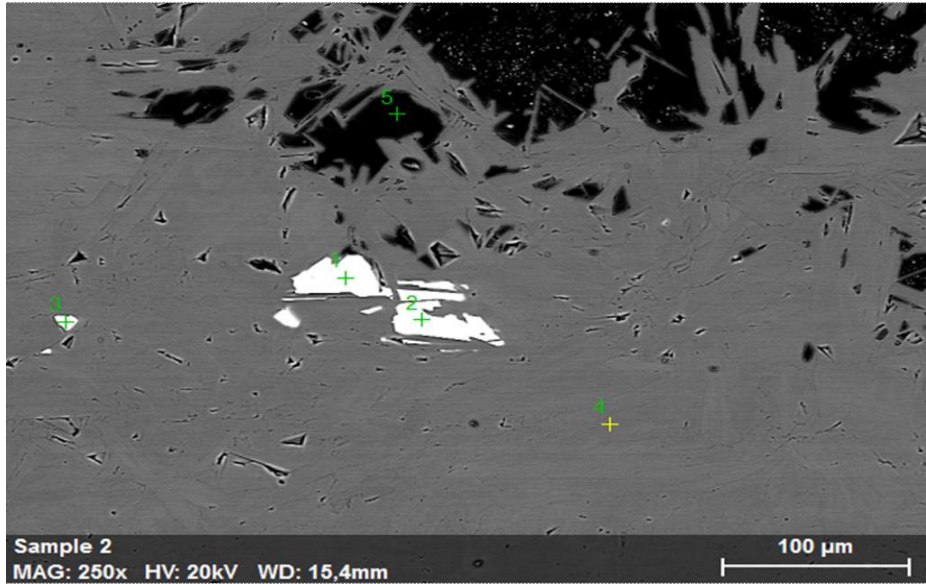| Name	Density [g/cm3]	Volume [cm3]	Km	Anisotropy (P)	Volume corrected Km [SI]	Field in A/m	Induced [A/m]	Modulus [A/m]	NRM of sample [A/m]	Decl (Spec.S)	Incl (Spes.S)	Volume%magnetite	Q-value
1A1	2,66	9,67	3,89E-03	1,004	0,000	41,58138882	0,016709956	0,005893	0,0061	36,20	-87,50	0,01	0,36
1B1	2,67	9,44	3,66E-03	1,056	0,000	41,58138882	0,016112788	0,000675	0,0007	67,20	-28,90	0,01	0,04
1C1	2,68	9,46	3,73E-03	1,04	0,000	41,58138882	0,016412781	0,003937	0,0042	84,70	-71,50	0,01	0,25
3A1	2,67	9,65	4,95E-01	1,401	0,051	41,58138882	2,131638658	1,279012	1,3254	71,20	44,20	1,48	0,62
3A2	2,7	9,63	5,48E-01	1,392	0,057	41,58138882	2,365346292	0,815638	0,8470	45,40	33,30	1,64	0,36
3A3	2,69	9,64	4,45E-01	1,326	0,046	41,58138882	1,917747455	0,512882	0,5320	60,50	19,50	1,33	0,28
3B1	2,71	9,65	9,35E-01	1,382	0,097	41,58138882	4,028008525	0,765111	0,7929	103,70	58,10	2,79	0,20
3B2	2,73	9,81	1,05E+00	1,365	0,107	41,58138882	4,45484604	1,966903	2,0050	66,20	53,60	3,09	0,45
3B3	2,75	9,61	1,10E+00	1,294	0,114	41,58138882	4,759576244	1,595805	1,6606	75,40	49,30	3,30	0,35
3C1	2,62	9,84	3,53E-01	1,266	0,036	41,58138882	1,489577191	0,554189	0,5632	0,90	-13,00	1,03	0,38
3C2	2,71	9,57	8,09E-01	1,535	0,084	41,58138882	3,513344932	3,183594	3,3266	49,50	37,70	2,43	0,95
3C3	2,68	9,7	4,93E-01	1,425	0,051	41,58138882	2,11336337	1,623007	1,6732	77,40	75,60	1,46	0,79
3C3_1	2,68	9,47	7,24E-01	1,285	0,076	41,58138882	3,178100235	1,272260	1,3435	56,70	48,10	2,20	0,42
4A1	2,7	9,74	2,39E-02	1,079	0,002	41,58138882	0,101818904	0,074530	0,0765	33,70	77,70	0,07	0,75
4A2	2,62	9,89	1,25E-02	1,039	0,001	41,58138882	0,052554839	0,035958	0,0364	42,90	43,30	0,04	0,69
4A3	2,63	9,99	1,20E-02	1,04	0,001	41,58138882	0,049739499	1,235195	1,2364	186,30	-70,20	0,03	24,86
4B1	2,69	9,59	9,80E-03	1,045	0,001	41,58138882	0,042483258	0,012846	0,0134	358,40	34,50	0,03	0,32
4B2	2,7	9,69	5,88E-04	1,064	0,000	41,58138882	0,002522347	0,034415	0,0355	339,00	62,10	0,00	14,08
4B3	2,64	9,84	9,10E-03	1,044	0,001	41,58138882	0,038454333	0,021554	0,0219	282,10	77,70	0,03	0,57
8A1	2,77	9,74	1,23E+00	1,235	0,126	41,58138882	5,233961262	24,841980	25,5051	307,50	14,60	3,63	4,87
8A2	2,83	9,78	9,19E-01	1,244	0,094	41,58138882	3,90771518	19,443980	19,8814	311,30	16,50	2,71	5,09
8B1	2,77	9,24	1,39E+00	1,337	0,150	41,58138882	6,237208323	40,075230	43,3715	318,90	12,00	4,32	6,95
8B2	2,9	9,78	9,37E-01	1,248	0,096	41,58138882	3,982544674	28,400680	29,0396	315,80	16,30	2,76	7,29
9A1	2,71	9,64	6,18E-01	1,335	0,064	41,58138882	2,665694843	0,718162	0,7450	48,40	60,30	1,85	0,28
9A2	2,71	9,74	1,06E+00	1,661	0,109	41,58138882	4,533822888	2,396252	2,4602	55,80	30,10	3,14	0,54
9A3	2,81	9,34	2,75E+00	1,952	0,294	41,58138882	12,22065442	13,209230	14,1426	57,50	45,60	8,47	1,16
9B1	2,65	9,94	7,53E-01	1,677	0,076	41,58138882	3,149560125	0,805112	0,8100	92,20	73,50	2,18	0,26
9B2	2,67	9,9	8,58E-01	1,645	0,087	41,58138882	3,601620294	2,192903	2,2151	66,10	50,00	2,50	0,62
9B3	2,76	9,67	1,45E+00	1,55	0,149	41,58138882	6,213558102	6,000251	6,2050	84,90	57,60	4,31	1,00
9C1	2,72	9,65	5,63E-01	1,591	0,058	41,58138882	2,425509199	0,574916	0,5958	19,00	63,90	1,68	0,25
9C2	2,69	9,85	6,11E-01	1,663	0,062	41,58138882	2,577623961	0,617695	0,6271	3,30	58,50	1,79	0,24
9C3	2,67	9,88	5,63E-01	1,474	0,057	41,58138882	2,367361459	1,131918	1,1457	82,80	65,40	1,64	0,48
9D1	2,68	9,41	5,36E-01	1,345	0,057	41,58138882	2,368062303	0,541415	0,5754	309,70	82,20	1,64	0,24
9D2	2,69	9,73	5,11E-01	1,376	0,053	41,58138882	2,185480189	0,604372	0,6211	349,80	80,40	1,51	0,28
9D3	2,67	10,01	1,01E+00	1,596	0,101	41,58138882	4,199678731	3,499348	3,4959	79,40	63,00	2,91	0,83
10A1	2,92	9,58	1,05E-02	1,177	0,001	41,58138882	0,0456614	0,152974	0,1597	14,60	30,60	0,03	3,50
10A2	2,89	9,22	6,69E-03	1,165	0,001	41,58138882	0,030162292	0,169757	0,1841	353,10	25,10	0,02	6,10
10B1	2,89	9,5	1,05E-02	1,187	0,001	41,58138882	0,046002147	0,199181	0,2097	322,50	37,10	0,03	4,56
10C1	2,94	9,46	9,90E-03	1,153	0,001	41,58138882	0,043528593	0,154153	0,1630	34,80	64,60	0,03	3,74
11A1	2,65	9,68	1,24E-03	1,062	0,000	41,58138882	0,00531795	0,000176	0,0002	307,90	35,70	0,00	0,03
11A2	2,7	9,76	1,17E-03	1,099	0,000	41,58138882	0,004988915	0,000063	0,0001	310,10	43,20	0,00	0,01
11B1	2,77	9,59	2,32E-03	1,09	0,000	41,58138882	0,010067986	0,000357	0,0004	279,10	36,80	0,01	0,04
11C1	2,63	10,11	1,23E-03	1,093	0,000	41,58138882	0,005062976	0,000050	0,0000	149,30	39,20	0,00	0,01
11D1	2,67	9,83	1,79E-03	1,083	0,000	41,58138882	0,007554869	0,000302	0,0003	94,90	15,40	0,01	0,04
12A1	2,88	9,47	7,73E-03	1,084	0,001	41,58138882	0,033945693	0,001835	0,0019	354,20	73,80	0,02	0,06
12A2	2,82	9,84	7,75E-03	1,078	0,001	41,58138882	0,032753795	0,001542	0,0016	344,50	71,90	0,02	0,05
12B1	2,91	9,34	7,18E-03	1,074	0,001	41,58138882	0,031978492	0,002052	0,0022	337,20	62,40	0,02	0,07
12B2	2,87	9,58	7,66E-03	1,082	0,001	41,58138882	0,03325209	0,002080	0,0022	334,70	62,10	0,02	0,07
13A1	2,66	9,67	2,85E-03	1,023	0,000	41,58138882	0,012237914	0,008029	0,0083	335,70	3,50	0,01	0,68
13A2	2,66	9,61	3,50E-03	1,044	0,000	41,58138882	0,015161414	0,003863	0,0040	308,90	42,20	0,01	0,27
13A3	2,6	10,07	3,68E-03	1,034	0,000	41,58138882	0,015174936	0,003681	0,0037	35,60	55,10	0,01	0,24
13B1_1	2,59	9,29	3,89E-03	1,041	0,000	41,58138882	0,017420319	0,016400	0,0177	33,30	12,00	0,01	1,01
13B1_2	2,66	9,18	3,54E-03	1,041	0,000	41,58138882	0,016030124	0,007753	0,0084	338,80	-11,90	0,01	0,53
13B2	2,59	9,81	3,53E-03	1,04	0,000	41,58138882	0,014941325	0,007429	0,0076	11,80	45,60	0,01	0,51
13B3	2,66	9,53	3,39E-03	1,053	0,000	41,58138882	0,014800007	0,032813	0,0344	169,70	75,70	0,01	2,33
13C1	2,63	9,7	3,89E-03	1,024	0,000	41,58138882	0,016662563	0,013671	0,0141	0,40	34,00	0,01	0,85
13C2	2,66	9,59	3,39E-03	1,028	0,000	41,58138882	0,014685731	0,013489	0,0141	359,80	32,10	0,01	0,96

Appendix D – SEM Results

Following is a table of all the point analysis from SEM. They are listed in normalized atom % and have been used for mineral identification.
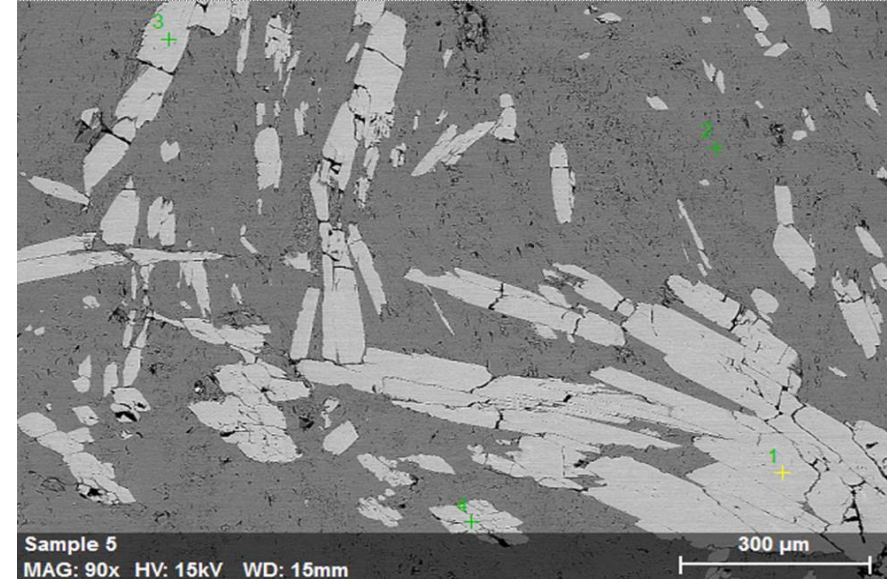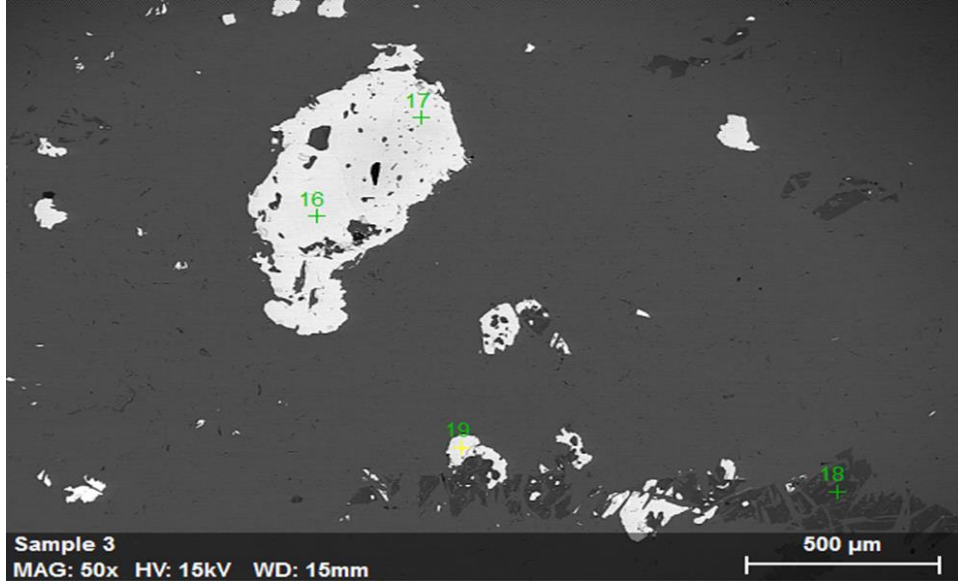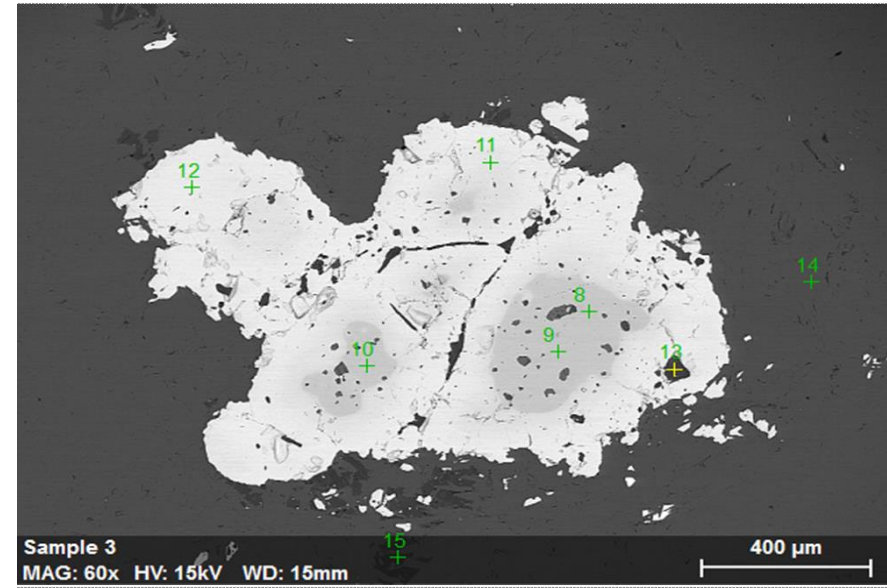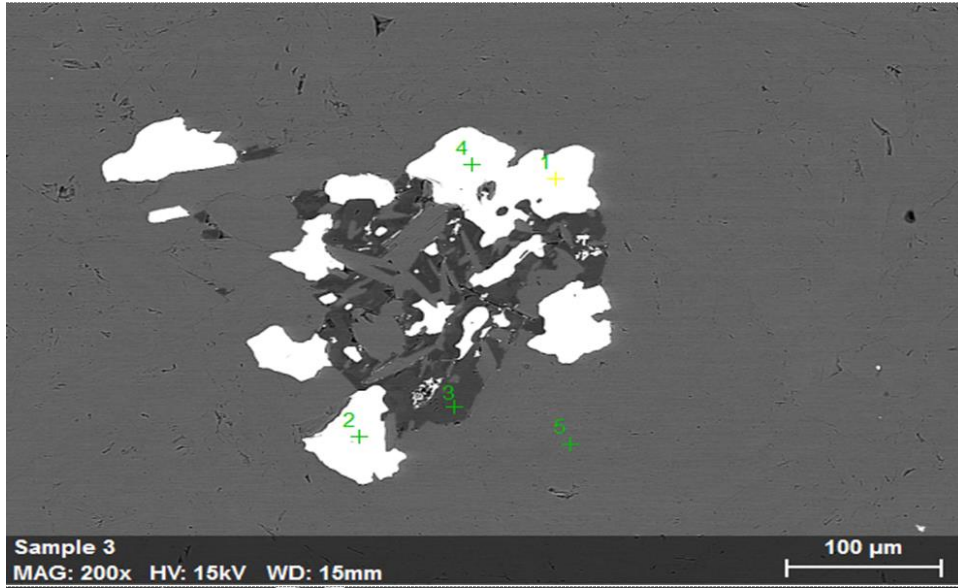
Point	Mineral	Fe	Cr	O	C	Mg	Mn	Ni	S	Al	Si	Ca	Br	Zn	Ti	Zr	Hf	La	P	Ba	Ag/Th	V	Cs	F	Y	Co	W
5_1	Ca-rich amphibole	1,51		51,07	6,95	11,19					22,97	6,31															
5_3	Ca-rich amphibole	1,23		50,46	9,62	10,55					22,13	6															
5_4	Ca-rich amphibole	1,7		51,46	6,74	10,93					22,9	6,28															
5_5	Ca-rich amphibole	1,73		50,7	8,42	10,67					22,29	6,18															
5_6	Ca-rich amphibole	1,55		50,34	9,17	10,59					22,3	6,05															
5_7	Ca-rich amphibole	1,71		50,58	9,1	10,57					21,99	6,04															
7_4	Ca-rich amphibole	1,7		52,12	6,05	10,97					22,55	6,32															
7_5	Ca-rich amphibole	1,52		51,87	8,09	11,07					20,59	6,86															
5_2	Chlorite	3,22	0,36	53,51	11,06	14,25				5,38	12,22																
5_8	Chlorite	3,49	0,26	52,72	11,09	14,62				5,44	12,38																
6_6	Chlorite	2,98		54,89	6	14,47				5,52	12,36																
6_28	Chlorite	3,46		54,06	9,73	14,32				5,99	12,43																
7_1	Chlorite	3,01	0,27	57,28		17,56				7,29	14,6																
7_2	Chlorite	3,23		57,89		16,97				7,13	14,86																
7_3	Chlorite	4,05	0,26	58,13		16,56				6,73	14,26																
7_7	Chlorite	4,3	0,3	53,66	11,43	13,6				5,32	11,38																
12_10	Chlorite	5,26		58,95		14,39				8,74	12,66																
2_9	Chrommagnetite	34,12	8,17	44,22	12,82	0,67																					
2_28	Chrommagnetite	28,83	13,43	44,58	12,35	0,81																					
3_16	Chrommagnetite	35,69	8,24	45,21	10,11	0,76																					
3_17	Chrommagnetite	33,59	10,13	45,94	9,63	0,7																					
2_23	Ferrian Chromite	12,89	17,3	45,56	12,3	3,46				8,5																	
3_8	Ferrian Chromite	12,78	17,57	48,49	10,53	3,95								1,95													
3_9	Ferrian Chromite	12,9	18,09	48,18	10,39	3,83				4,66				1,96													
3_10	Ferrian Chromite	13,05	17,85	48,24	10,29	3,57				4,88				1,87	0,25												
2_6	Ferrichromite	23,38	17,63	44,94	12,68	1,37																					
2_7	Ferrichromite	26,31	15,7	44,06	12,78	1,15																					
2_13	Ferrichromite	25,22	16,63	45,46	11,44	1,24																					
2_15	Ferrichromite	22,98	18,71	45,59	11,28	1,44																					
2_24	Ferrichromite	26,3	15	45,39	12	1,31																					
2_25	Ferrichromite	22,76	18,41	45,52	11,71	1,6																					
3_11	Ferrichromite	27,35	16,38	45,91	9,33	1,03																					
8_11	Ferrichromite	25,77	15,59	48,22	7,19	3,23																					
8_1	Forsterite	6,12		51,76		25,61					16,51																
8_2	Forsterite	5,31		51,28		25,75					17,66																
8_8	Forsterite	5,57		51,5		26,23					16,7																
8_9	Forsterite	5,69		50,99		27,33					15,99																
8_15	Forsterite	5,32		48,96	7,91	22,24					15,56																
8_22	Forsterite	5,17		52,04		24,85					17,93																
8_3	Heazlewoodite			2,37	14,64			55,11	27,88																		
8_1a	Heazlewoodite			2,9	16,22			53,02	27,86																		
8_2a	Heazlewoodite			2,96	17,15			53,34	26,54																		
12_17	Hydroxyapatite			51,34	6,3							29,4							11,71					1,28			
12_1	Hydroxylapatite			51,46	5,19							30							12,24					1,15			
12_2	Hydroxylapatite			51,57	0,48							29,6							12,04					1,1			
12_7	Hydroxylapatite			51,17	6,45							29,2							11,81					0,25			
12_8	Hydroxylapatite			50,58	6,45							28,8							12,44					1,72			
12_9	Hydroxylapatite			50,43	6,78							27,5							14,16					1,17			

Point	Mineral	Fe	Cr	O	C	Mg	Mn	Ni	S	Al	Si	Ca	Br	Zn	Ti	Zr	Hf	La	P	Ba	Ag/Th	V	Cs	F	Y	Co	W
6_1	Ilmenite	19,82		48,76	8,92		1,76								20,74												
6_2	Ilmenite	19,71		48,4	8,58		1,83								21,47												
6_3	Ilmenite	19,86		47,93	9,41		1,81								20,99												
6_15	Ilmenite	19,77		48,71	8,57		1,83								21,12												
6_16	Ilmenite	19,16		49,07	9,28		1,77								20,72												
6_18	Ilmenite	19,97		48,41	8,46		1,93								21,23												
6_19	Ilmenite	20,3		48,58	8,43		1,86								20,82												
6_20	Ilmenite	19,41		48,89	8,78		1,72								21,2												
6_23	Ilmenite	19,9		48,42	8,66		1,75								21,27												
6_24	Ilmenite	19,32		48,97	8,45		1,94								21,32												
12_5	Ilmenite	19,78		48,85	8,56		1,12								21,69												
12_6	Ilmenite	20,56		48,98	8,14		1,22								21,1												
12_14	Ilmenite	20,2		49,56	8,25		1,15								20,83												
12_15	Ilmenite	20,54		48,82	8,22		1,27								21,15												
12_16	Ilmenite	20,04		48,8	8,45		1,17								21,54												
12_22	Ilmenite	19,85		48,72	8,53		1,15								21,76												
2_27	Ishkulite	40,25	2,34	43,85	13,55																						
3_12	Ishkulite	41,85	2,21	45,33	10,66																						
8_10	Ishkulite	36,56	7,42	48,07	6,3	1,65																					
8_13	Ishkulite	44,32	1,75	47,06	6,88																						
8_19	Ishkulite	37,67	5,22	48,2	7,66	1,26																					
10_1	Mackinawite	46,52			18,8				34,67																		
10_2	Mackinawite	46,73			18,1				35,16																		
10_4	Mackinawite	50,37			17,44				32,19																		
2_5	Magnesite	1,51		55,39	16,55	25,87	0,23					0,45															
2_8	Magnesite	0,51		56,12	21,32	21,26	0,78																				
3_3	Magnesite	4,41		59,38	11,93	24,28																					
3_13	Magnesite	4,96		59,05	13,88	21,85						0,26															
3_15	Magnesite	0,16		58,53	14,36	24,84																					
3_18	Magnesite	1,47		57,1	18,53	22,9																					
8_12	Magnesite	0,85		57,64	16,79	24,72																					
8_21	Magnesite	1,64		58,07	16,7	23,5																					
2_12	Magnetite	41,3		45,14	13,56																						
2_26	Magnetite	41,59	0,89	43,62	14,23																						
3_1	Magnetite	44,58	0,66	44,33	10,43																						
3_2	Magnetite	43,55	1,59	44,3	10,56																						
3_4	Magnetite	43,48	1,56	45,05	9,9																						
3_19	Magnetite	43,3	1,34	44,33	11,03																						
8_4	Magnetite	48,51		50,52			0,97																				
8_6	Magnetite	49,22		49,98			0,92																				
8_7	Magnetite	43,78		47,14	8,23		0,86																				
8_16	Magnetite	43,92		47,84	7,17		1,07																				
8_17	Magnetite	49,54		49,4			1,07																				
8_18	Magnetite	89,55		4,57	4,27		1,6																				
8_20	Magnetite	44,11		47,7	7,2		0,98																				
8_23	Magnetite	44,2		47,9	7,03		0,86																				
8_24	Magnetite	43,77		47,78	7,5		0,95																				
8_25	Magnetite	44,19		47,57	7,29		0,95																				
8_3a	Magnetite	48,2		51,02			0,77																				

Point	Mineral	Fe	Cr	O	C	Mg	Mn	Ni	S	Al	Si	Ca	Br	Zn	Ti	Zr	Hf	La	P	Ba	Ag/Th	V	Cs	F	Y	Co	W
6_5	Monazite			55,34	13,87						1,19							5,02	17,26	3,21	1,3	2,37	0,44				
6_8	Monazite			55,48	14,17						0,93							4,95	17,47	3,21	0,94	2,41	0,43				
6_9	Monazite			55,19	14,78						1,03							4,94	16,58	3,27	1,2	2,51	0,5				
6_10	Monazite			56,24	13,12						1,34							4,27	16,63	3,28	1,48	2,63					
6_11	Monazite			54,88	14,73						0,77							5,23	17,3	3,39	0,75	2,48	0,47				
6_13	Monazite			55,52	13,74						1,03							5,24	17,06	3,37	1,15	2,46	0,46				
6_14	Monazite			58,42	8,6						1,1							5,57	18,42	3,5	1,25	2,6	0,54				
6_17	Monazite			55,37	13,67						0,89							5,37	17,44	3,39	0,73	2,64	0,52				
6_21	Monazite			55,26	14,21						0,89							5,3	16,92	3,36	0,97	2,64	0,46				
6_22	Monazite			58,16	11,46						1,24							5,31	16,34	3,37	1,57	2,55					
6_25	Monazite			56,89	12,06						1,15							5,48	17	3,44	1,27	2,72					
6_26	Monazite			55,17	14						0,89							5,14	17,79	3,33	0,8	2,43	0,45				
12_18	Monazite			56,84	13,48													5,19	16,85	3,85	0,3	2,93	0,56				
12_20	Monazite			57,08	12,03						0,9							5,41	17,11	3,51	1,26	2,71					
12_21	Monazite			56,07	12,29						0,96							5,41	18,48	3,46	0,68	2,66					
2_1	Pentlandite	17,41		1,96	29			26,02	25,6																		
2_2	Pentlandite	16,7		1,82	30,26			26,52	24,7																		
2_3	Pentlandite	16,71		1,69	31,24			24,51	25,84																		
2_10	Pentlandite	17,4		1,29	30,87			24,86	25,59																		
2_11	Pentlandite	15,84		0,21	31,56			23,32	27,29																		
2_14	Pentlandite	17		1,3	31,26			25	25,44																		
10_7	Pyrrhotite	34,61		3,76	19,88			1,16	40,5																		
10_8	Pyrrhotite	35,05			21,29				42,66																		
2_4	Serpentine	1,4		53,03	9,95	19,57					16,04																
3_5	Serpentine	1,91		58,37		19,87					19,85																
3_14	Serpentine	1,62		53,68	7,43	16,45					16,19																
8_5	Serpentine	1,66	0,24	57,7		20,57					19,82																
8_14	Serpentine	1,24	0,34	58,07		20,83					19,51																
10_3	Trevorite	27,76		58,42	4,51			7,25			1,36	0,71															
10_5	Trevorite	25,09		58,25				11,27			0,85																
10_6	Trevorite	30,95		62,21				5,95			0,06																
10_9	Trevorite	29,01		59,71	8,13			2,49			0,06																
6_12	*Unknown*	1,78		52,95	12	6,85				3,87	4,93							3	10,68	1,96	0,52						
7_6	*Unknown*	30,16		58,16	5,2	0,8	1,78				3,46	0,4															
12_3	*Unknown*	0,74		55,85	13,15						2,92	0,81							13,35						0,72	0,98	
12_4	*Unknown*			55,22	12,87						2,18	1,11							14,49						13,86		0,28
6_4	Zircon	0,5		43,68	19,53						18,38				0,58	16,7	0,58										
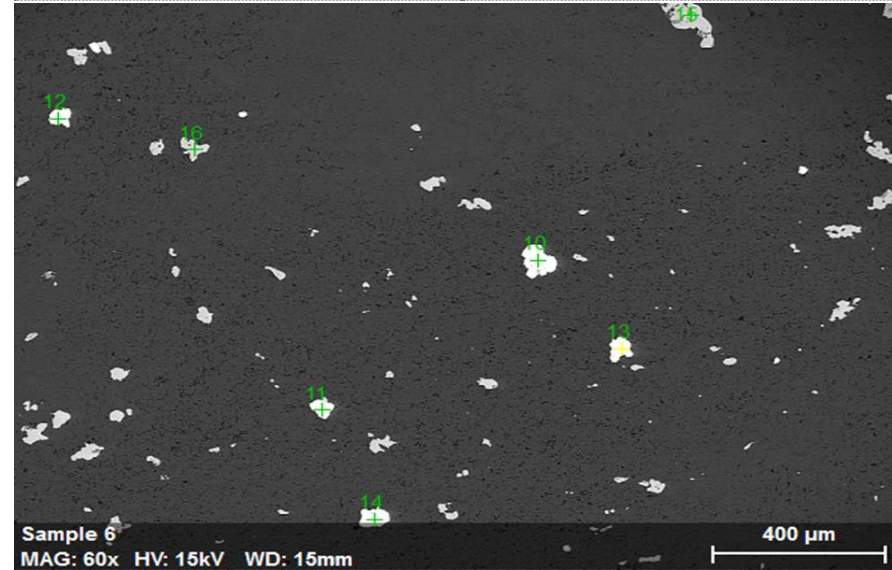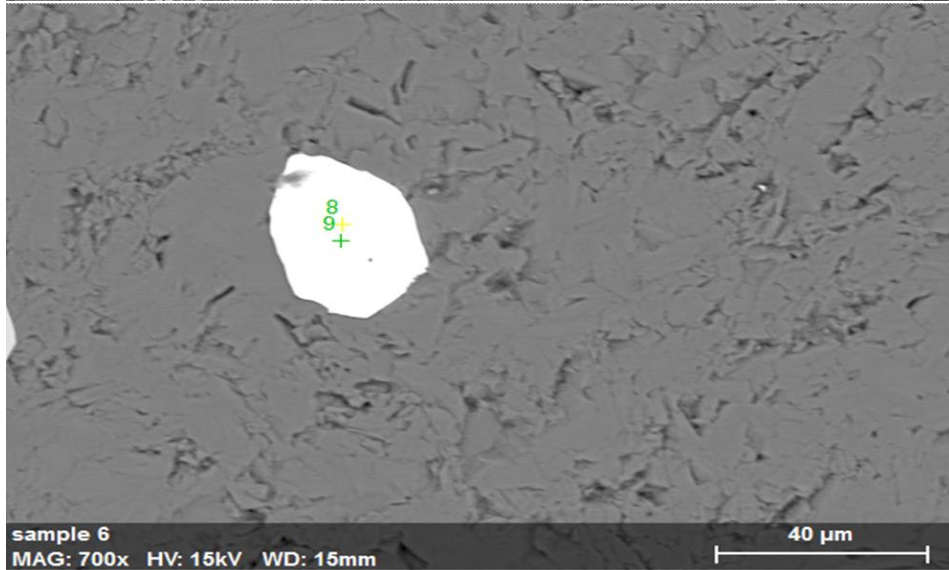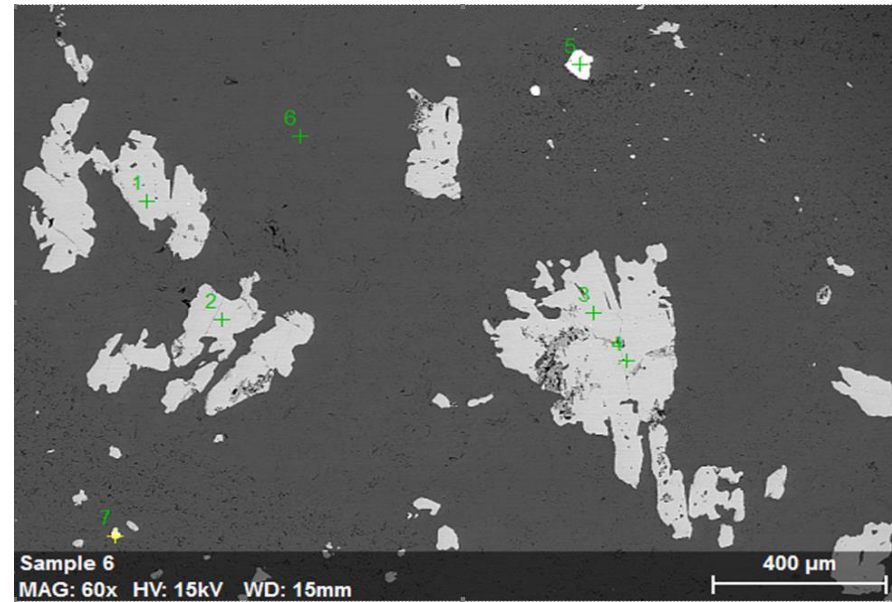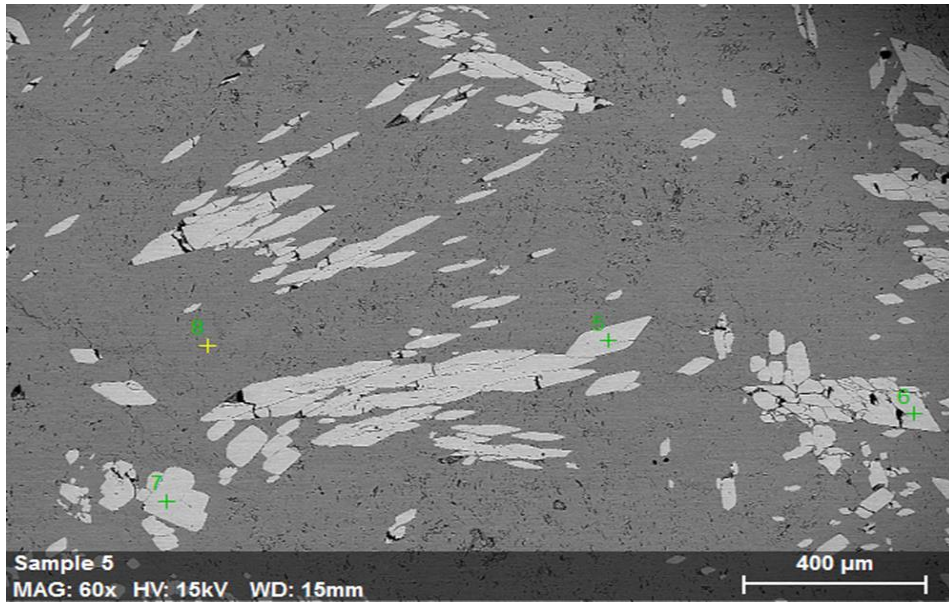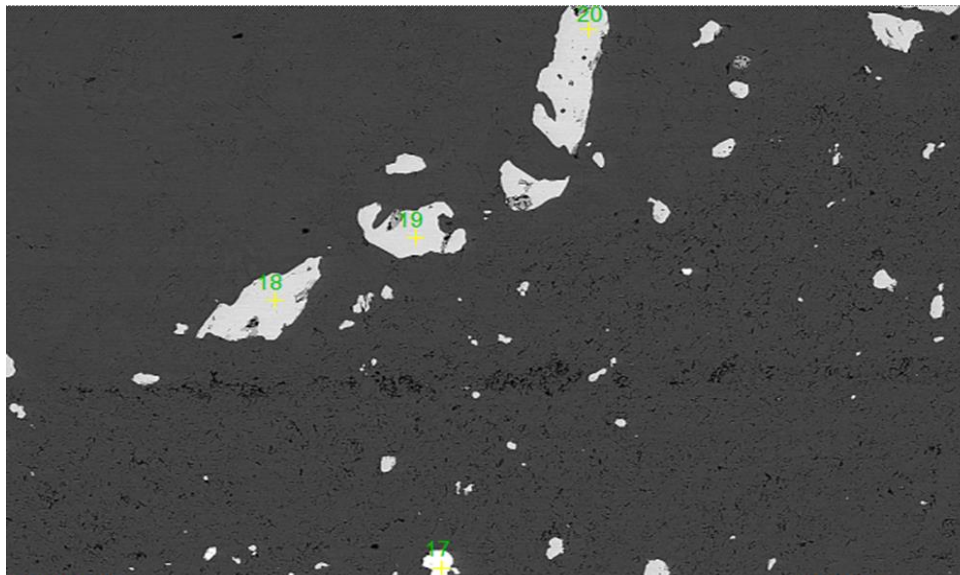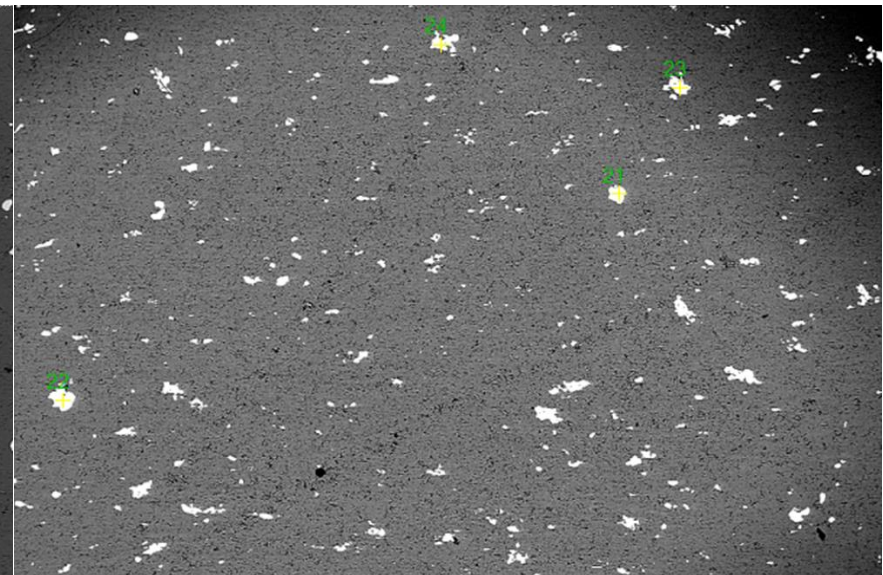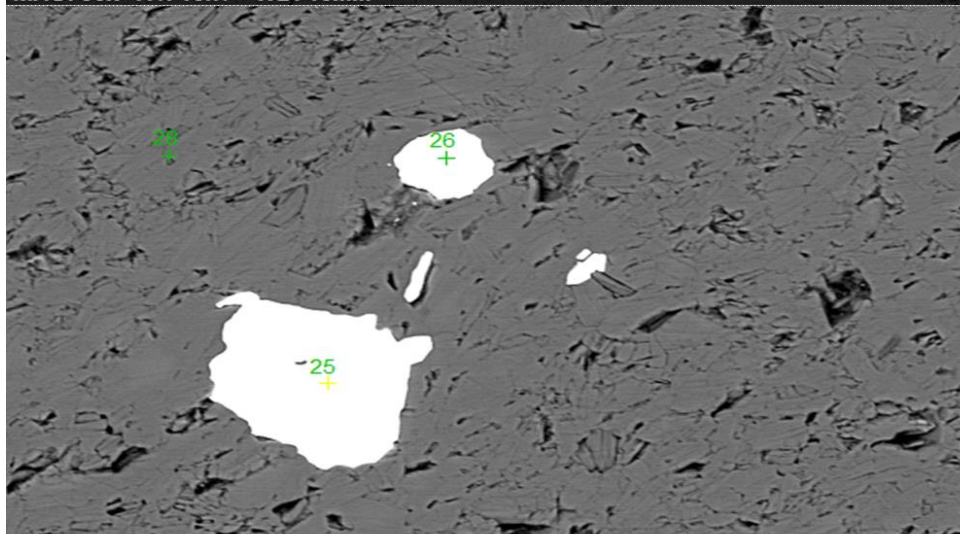
89
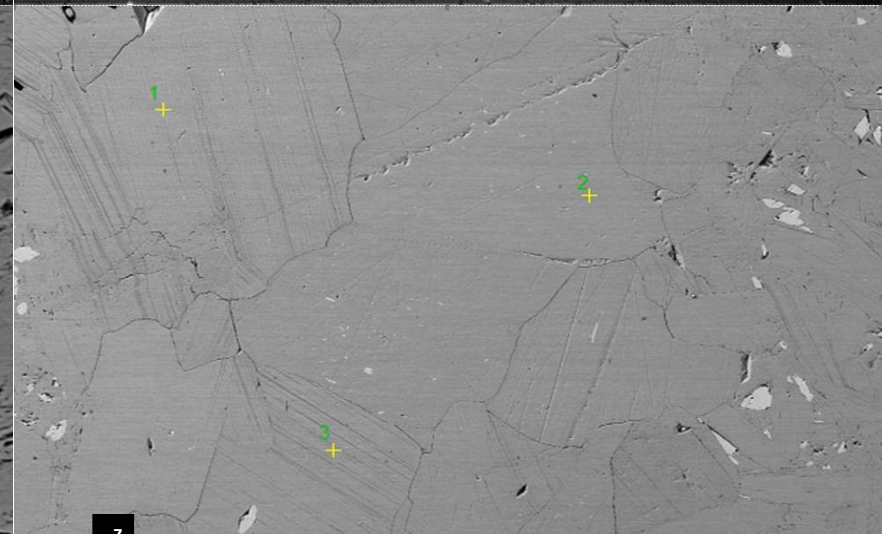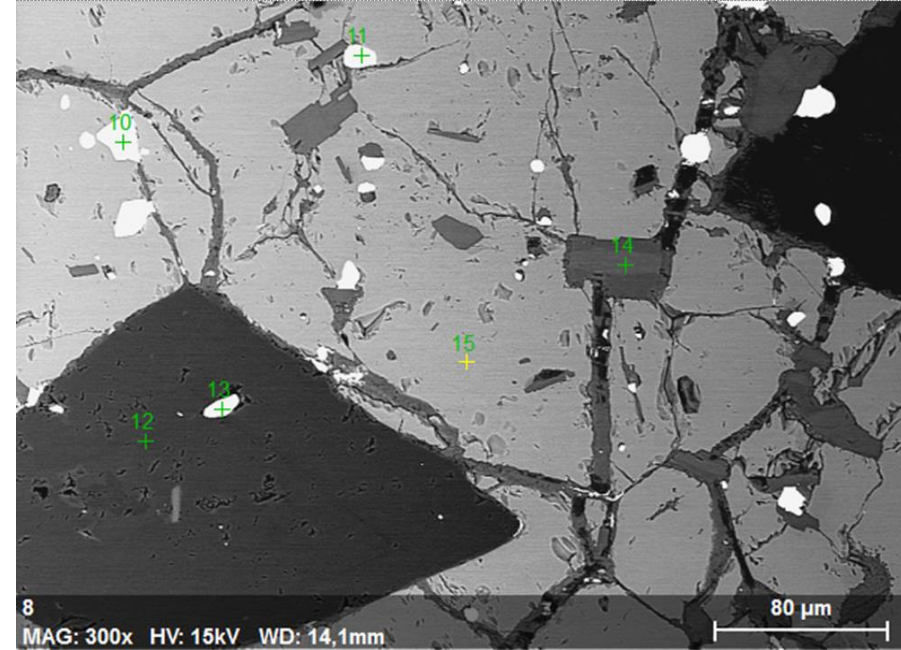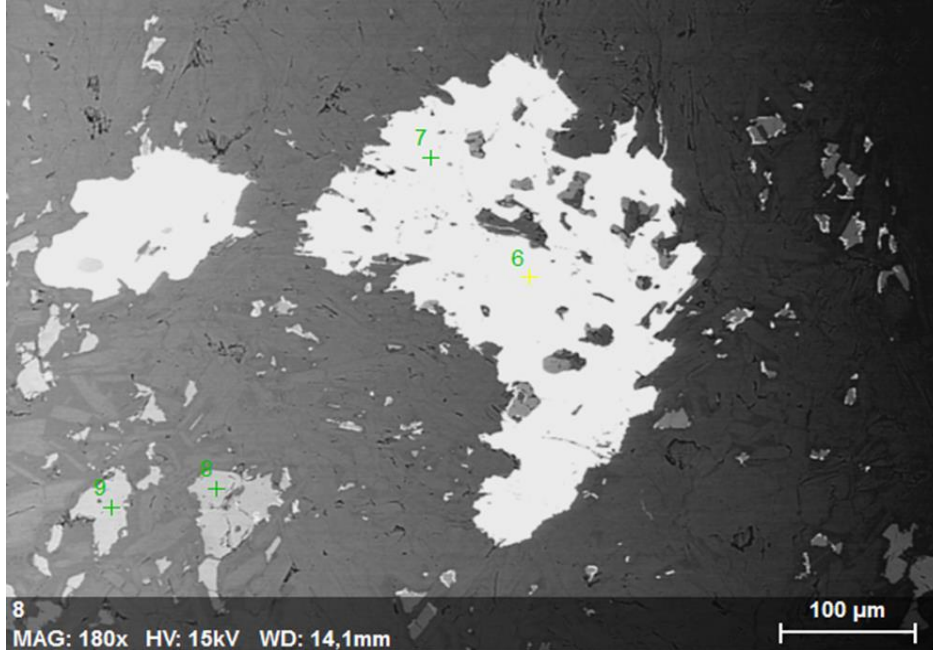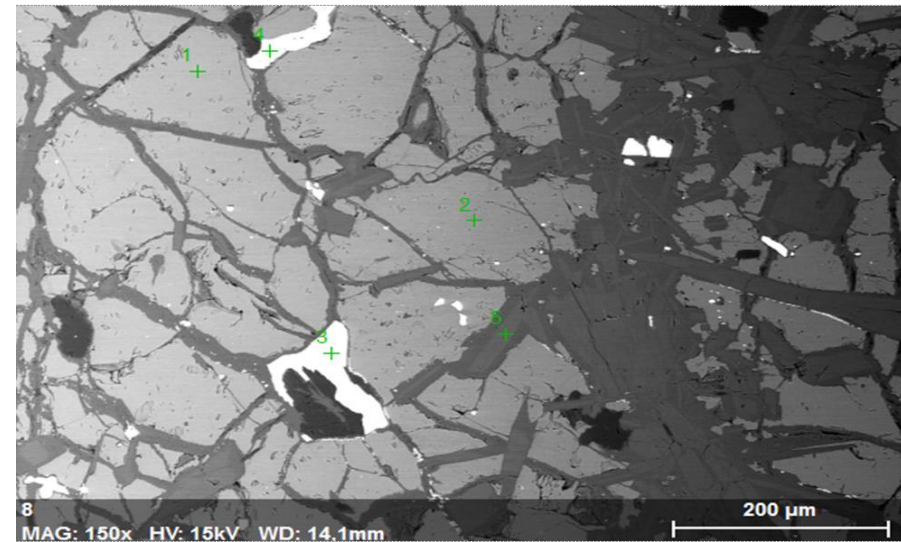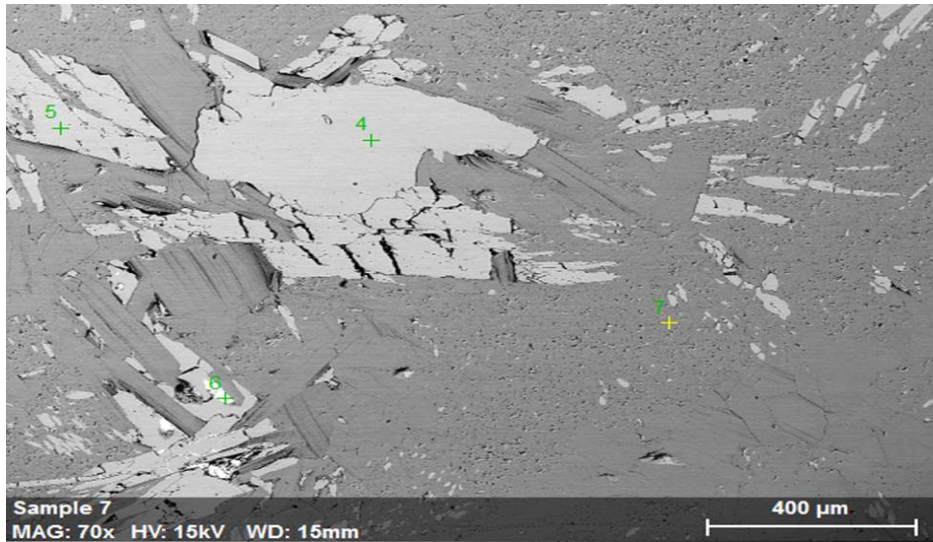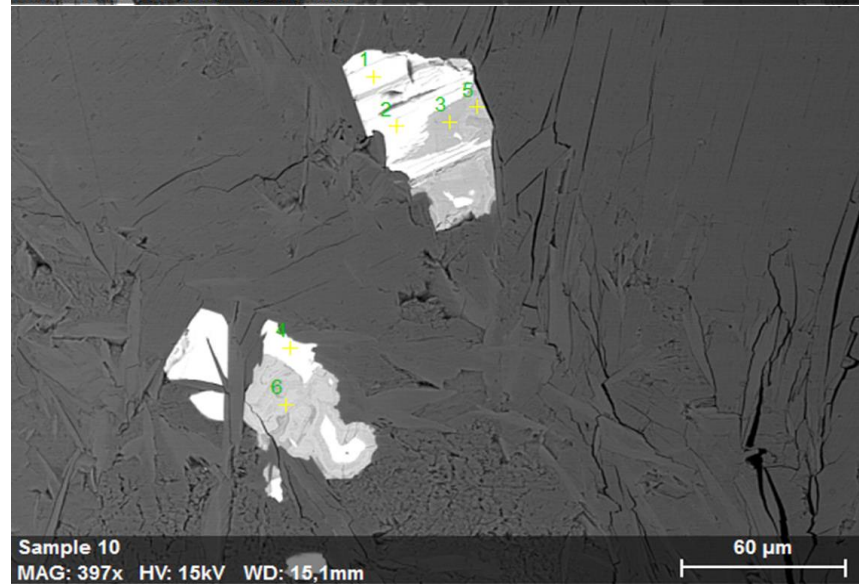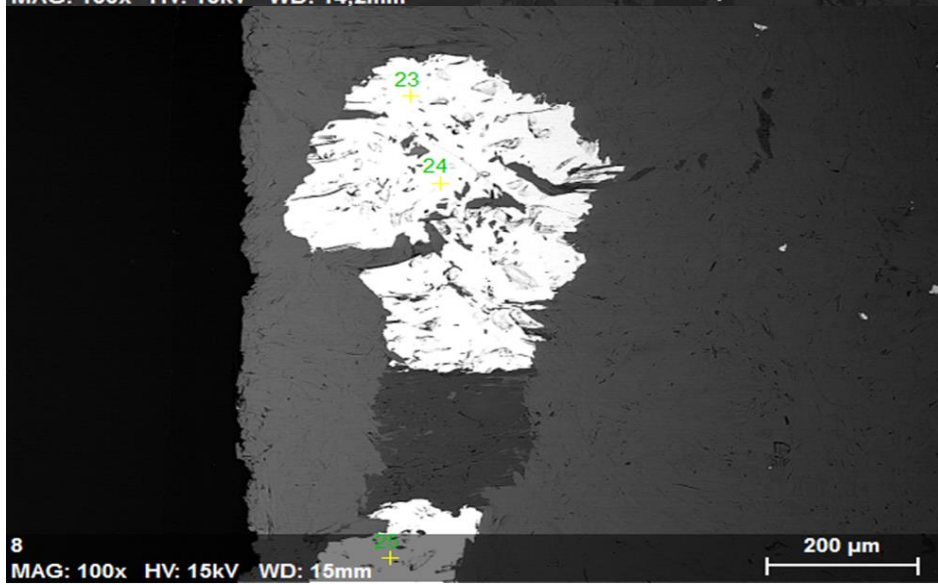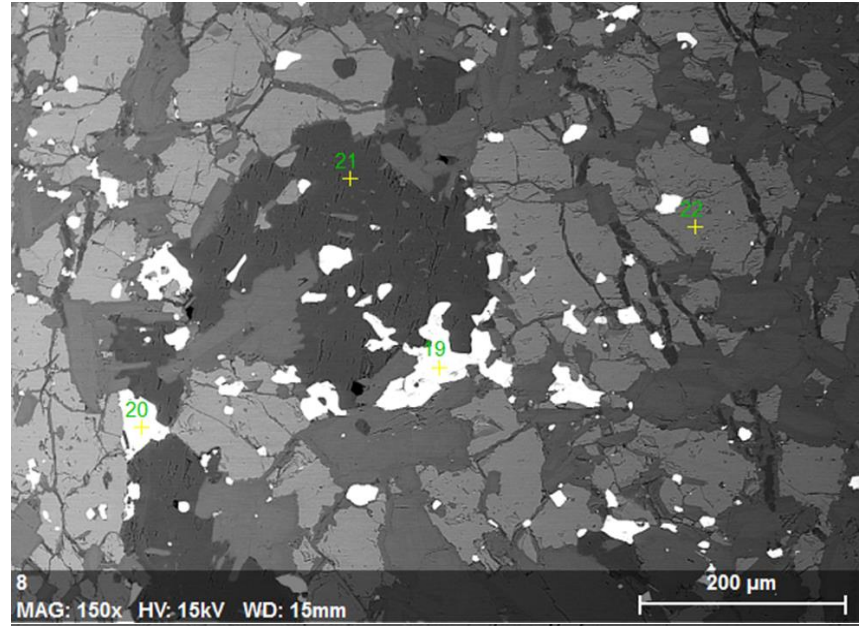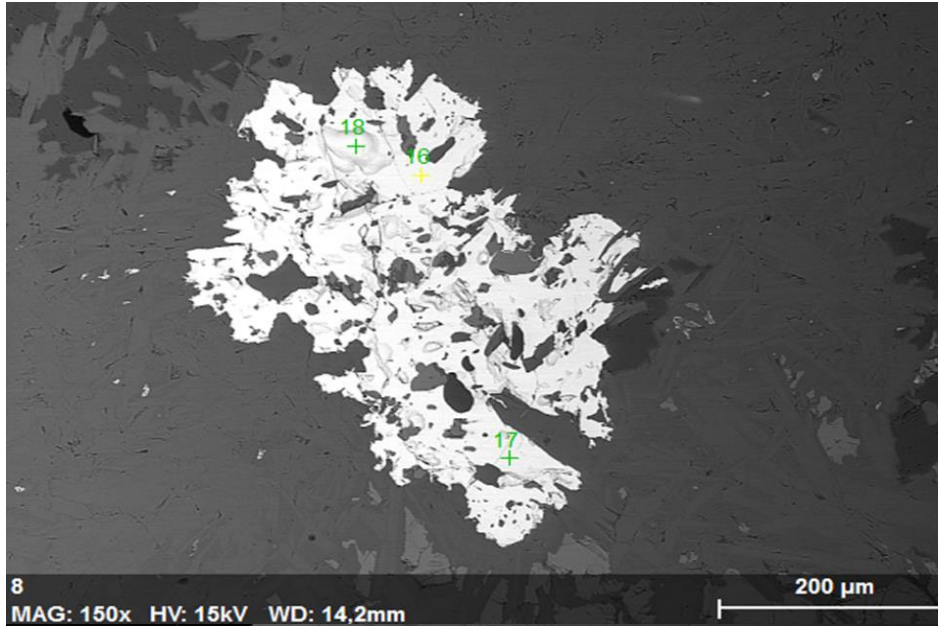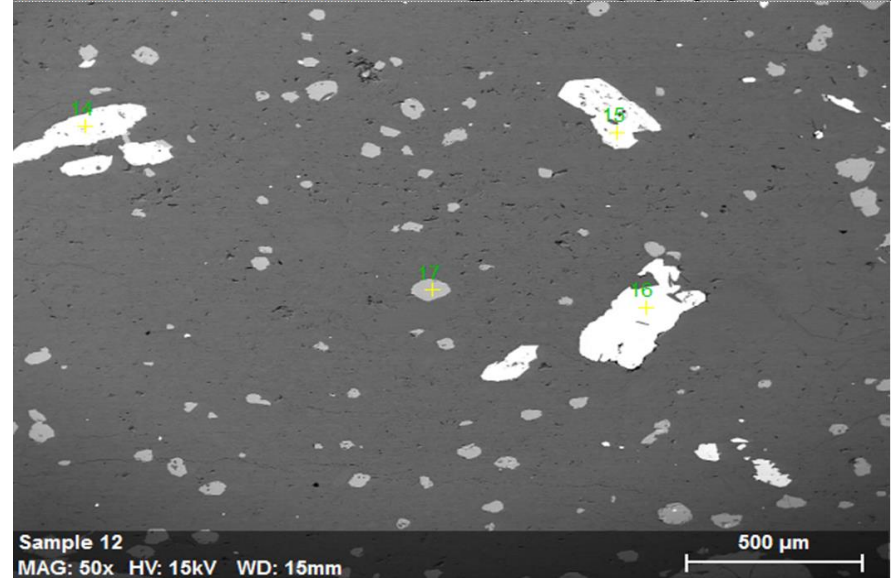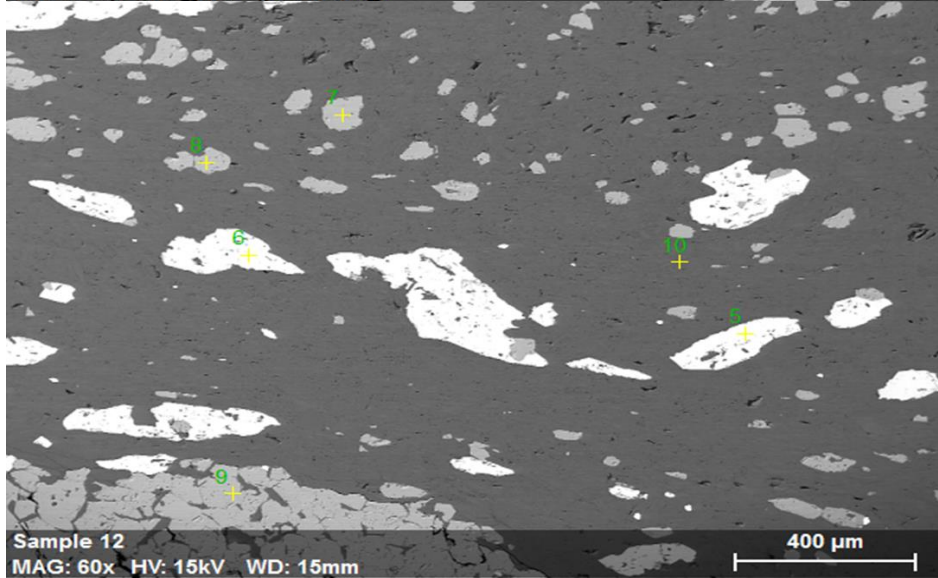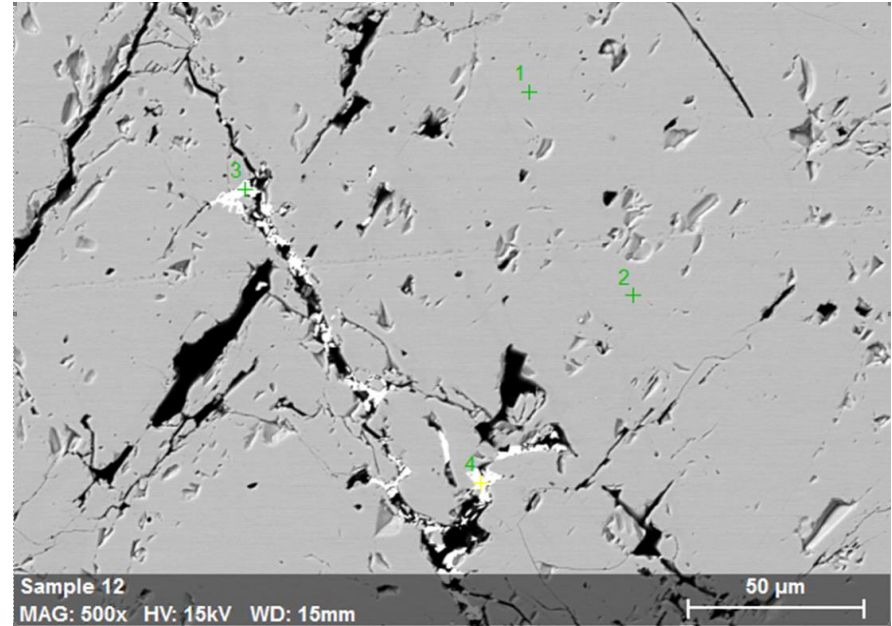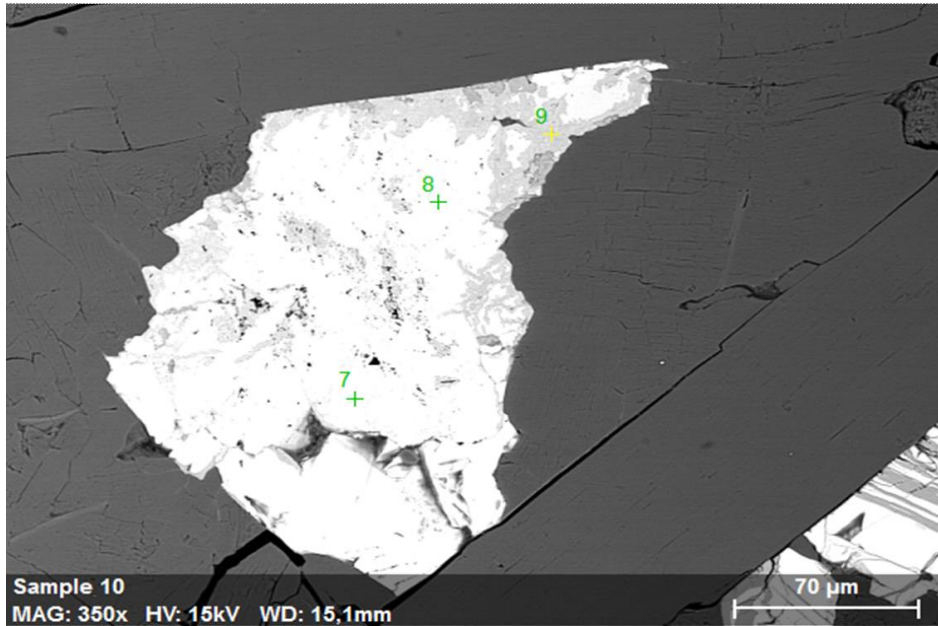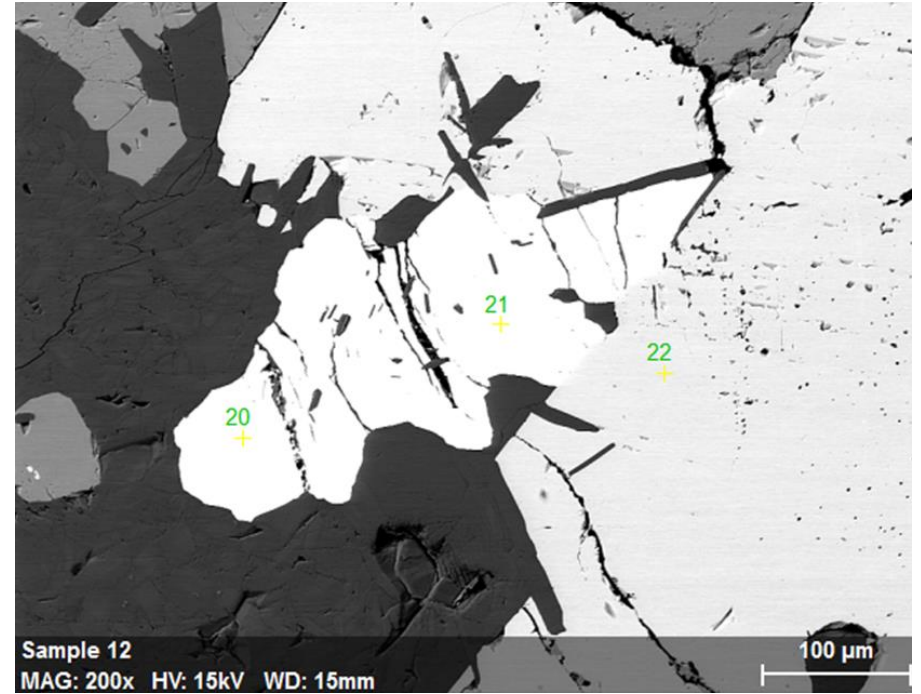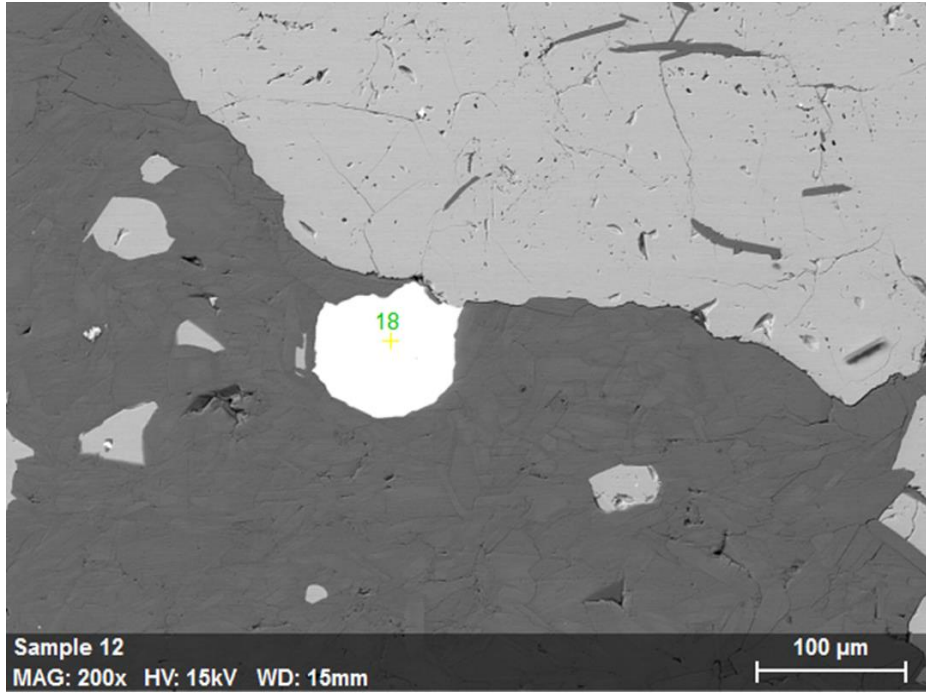
Appendix E – XRD Results

Sample	Quartz	Magnesite	Magnetite	Antigorite	Lizardite	Chrysotile	Chlorite	Feldspar	Talc	Siderite	Amphibole	Dolomite	Olivine	Brucite	Muscovite	Biotite	Garnet	Other
						[Volume %]												
1		0,62	0,9	88,85	4,85	0,28			5,4									
2	0,5	36,48	10,27	50,61	2,05	0,09												
3		8,05	7,37	80,12	4,22	0,25												
4		23,21		73,16	1,97	1,66												
5		1,47					64,08	2,47	7,1	2,24	22,62							
6		0,43	0,52				96,54					2,52						
7							95,19				4,81							
8		8,39	6,23	47,55	2,73									35,1				
9		34,58	2,65	60,61	2,04										0,13			
10		34,61		12,46						29			24					
11	75,91						2,45	6,9							12,09	1,85	0,79	
12							65,5		10									24,5
13			0,6	90,7	3,79				4,9									

Appendix E – Core Logging

Three readings were acquired for each stop, with an interval distance of approximately 5 meters. Reading 1, 2, and 3 are marked by blue, grey, and orange colors in the following graphs.

Siren Ånestad

The Magnetic Petrological Expression of Slipsteinsberget

NTNU

Norwegian University of
Science and Technology